Outer Electron Radiation Belt Dropouts: Geosynchronous and Ionospheric Responses

by

Olakunle Ogunjobi

Submitted in fulfillment of the requirements for the degree of Master of Science in the
School of Physics, University of KwaZulu-Natal.

As the candidate's Supervisor I have/have not approved this thesis for submission

Signed: ....   Name: ....   Date: ....

Durban, December 2011.

Abstract

The study of outer radiation belt dynamics has been ongoing for over 5 decades. Outer radiation belt dropouts involve the rapid lost of electron fluxes at the main phase of a storm and subsequent recovery. The characteristics of the dropouts are many and varied. This study examines the Geosynchronous Earth Orbit (GEO) and the ionospheric responses during Stream Interface (SI) and Magnetic Cloud (MC) events, using a combination of ground based and satellite instruments. SI- and MC-driven dropout events were inspected from summary plots of the Synchronous Orbit Particle Analyser (SOPA) instruments from the year 1996 to 2007. Comprehensive studies were done on six selected events. Analysis of the data from the instruments indicate that SIs and MCs are important lost drivers with significant differences in GEO and ionospheric environment. To validate the data and test for consistent response of the events, the Superposed Epoch Analysis (SEA) technique was used. The ground based measurements also revealed how the absorption peaks in the ionosphere correlated with dropouts and geophysical activity. Ionospheric absorption during SI associated dropouts was enhanced for $5 < L < 6$, while significant peaks in ionospheric absorption extended to lower L during MC driven dropouts. Wave-particle interactions and southward Interplanetary Magnetic Field (IMF-Bz) are apparent causes for the precipitation. This analysis showed that, within the confines of the selected events, SI driven dropouts were more dominant at the declining phase of the solar cycle while the MC driven dropouts were more dominant during solar maximum.

PREFACE

The experimental work presented in this dissertation was carried out in the School of Physics, University of KwaZulu-Natal, Westville Campus from July 2010 to October 2011, under the supervision of Dr. Andrew B. Collier.

These studies represent original work by the author and have not otherwise been submitted in any form for any degree or diploma to any tertiary institution. Where use has been made of the work of others it is duly acknowledged in the text.

DECLARATION 1 - PLAGIARISM

I, ..., declare that

1. The research reported in this thesis, except where otherwise indicated, is my original research.

2. This thesis has not been submitted for any degree or examination at any other university.

3. This thesis does not contain other persons' data, pictures, graphs or other information, unless specifically acknowledged as being sourced from other persons.

4. This thesis does not contain other persons' writing, unless specifically acknowledged as being sourced from other researchers. Where other written sources have been quoted, then:

    (a) Their words have been re-written but the general information attributed to them has been referenced

    (b) Where their exact words have been used, then their writing has been placed in italics and inside quotation marks, and referenced.

5. This thesis does not contain text, graphics or tables copied and pasted from the Internet, unless specifically acknowledged, and the source being detailed in the thesis and in the References sections.

Signed: ....

DECLARATION 2 - PUBLICATIONS

DETAILS OF CONTRIBUTION TO PUBLICATIONS that form part and/or include research presented in this thesis (include publications in preparation, submitted, in press and published and give details of the contributions of each author to the experimental work and writing of each publication)

Signed: ....

Acknowledgement

Contents

List of Figures

List of Tables

Chapter 1

Introduction

This Chapter presents the scientific background theory and overview of this study. It includes the discussion on the Sun's interaction with the Earth, and how this interaction drives different phenomena on Earth, including outer electron dropouts.

1.1 The Sun

The Sun emits electromagnetic radiation and matter consisting mainly of protons and electrons, with a small percentage of alpha particles and some heavier nuclei; into interplanetary space as a consequence of the nuclear fusion process in its interior. The variability of the Sun is reflected by the solar activity. The daily solar activity is estimated by counting the number of individual and groups of spots on the face of the Sun known as Sunspots. Sunspots are dark regions on the surface of the Sun, which represent large concentrations of strong magnetic flux associated with ultraviolet radiation. The existence of sunspots has been known since at least the forth century B.C. They can be as large as 20 Mm in diameter, each consisting of a central dark umbra at a temperature of 4100 K and a field strength up to 1T. The number of sunspots varies, with an 11 year period, but the amplitude of cycle varies and there have been periods of low sunspot number. Sunspot is associated with other solar activities. Some of these activities include solar flares and Corona Mass Ejection (CME). Brief explanation on these activities are provided in the following section.

1.2 Solar Activity

Prominences are ionized gases trapped in the twisted magnetic field of active regions. Eruptive prominences burst out of the confused magnetic fields around sunspots and may shoot upward (about 500000 km) in a few hours. Quiescent prominences develop as graceful arches over sunspot groups and, supported by magnetic fields of strength 0.5–1 mT can last weeks or even months. Densities typically are 10^{16}–10^{17} m^{-3} and temperatures are 5000–8000 K. Prominences probably form because of radiative instability [Leroy, 1989]. The classical model supporting prominence was also provided by Leroy [1989]. Though prominence form due to solar activities but its significance is not within the context of this present study.

A Solar flare is an eruption on the solar surface that rises to maximum in a few minutes and decays in an hour or less. This eruption is a strong transient outburst of radiation, released near the solar surface, that extend up to tens or hundreds of thousands of kilometers into the outer solar atmosphere. Most of the energy released with flare are in form of radiation from the corona. Plasma from solar flares carried in the solar wind can affect the space environment as well as ionospheric processes. At the onset, the field lines that have stretched out start to break and reconnect, which releases energy impulsively and causes the prominence to erupt more rapidly. The rate of solar particles incident on the Earth is strongly related to the level of activity of the Sun. When the Sun is actively producing solar flares, the particle fluxes reaching the Earth can be very high.

Corona Mass Ejection is an explosive ejection of a large amount of solar matter from the solar atmosphere into interplanetary space. Frequent occurrence of CME is not uncommon during solar maximum

activities. However, coronal activities vary in strength and are more active at the sunspot minimum of every 11 years, as corona becomes flattened in shape by the solar magnetic field due to its streamer composition. During solar minimum is the occurrence of higher than average speed of solar wind stream rotating with a 27-day rotation period of the sun known as the high-speed stream. Again, at the declining period of solar activities, the population of relativistic electrons is known to be closely related to the occurrence of high speed solar wind streams.

1.3 Solar Wind

The outermost layer of the Sun's atmosphere, the corona, is so hot, that it continually escapes into space. The resulting stream of charged particles that blows across the entire solar system is called the solar wind. It also carries the Interplanetary Magnetic Field (IMF). The solar wind is responsible for fueling magnetospheric storms, forming the Earth's magnetosphere. It is the major driver of particle precipitation into the Earth's ionosphere. The interaction of the Sun's frozen magnetic field with the Earth's magnetic field plays a dominant role in the transfer of energy from the solar wind into the ionosphere. This role defines the term geomagnetic storms. Earliest in situ observations of solar wind considered average solar wind speeds to be supersonic, around 400 km/s. The existence of solar winds was summarised in the 1950s on the basis of evidence that small variations in the Earth's magnetic field were produced by observable phenomena on the Sun, as well as from theoretical models for the equilibrium state of coronal [Leroy, 1989]. Early in situ observations of the solar wind have been made from spacecraft near the orbit of the Earth with properties characterised in Table 1.1.

Solar wind speed has a bimodal structure, that is, it is divided into two basic populations: High Speed Solar Wind Streams (HSSWs) and Slow Solar Wind Streams (SSWs). HSSWs are seen to be fast streams recurring with the Sun's equatorial rotation period characterized by density enhancements at their leading edge. HSSWs originate from coronal holes with temprature of about 900000 K and speed of more than 500 km/s. SSWs emanates perhaps from the vicinity of the streamer belt having lower temperature and velocity which are generally about 30000 K and 300 km/s respectively.

1.3.1 Stream Interfaces (SIs)

The bimodal structure of solar wind speed provides the mechanism for SI occurrence as shown in Figure 1.1. Because of the IMF, the two streams can not mingle. The slow solar wind from the vicinity of streamer belt is always at the leading edge of the trailing fast solar wind which originates from coronal holes. The region that separates dense, slow-moving plasma from fast, less dense plasma is the SI characterised by a sudden drop in solar wind number density with a proportional increase in observed temperature and a rise in velocity. The deflection of the solar wind azimuthal velocity from westward to eastward is the primary property of SI on arrival at Earth [e.g. Burlaga, 1974]. The peak in plasma pressure at the interface propagates outward into both streams carrying information about the presence of the interface. The association of geomagnetic activity with SIs leads to the possibility of forecasting geomagnetic activity based on predictions of the arrival of the SI. Activity is weak before the SI, very strong at the SI, and then decays slowly after the SI. Since the Sun is rotating the SI is a spiral intermediate to that expected in the two streams. During the period of declining solar cycle, the occurrence of SIs is pertinent as there is an increase in supersonic flows of HSSWs.

1.3.2 Magnetic Clouds (MCs)

A magnetic cloud (MC) is a transient ejection in the solar wind defined by relatively strong magnetic fields, a smooth rotation of the magnetic field direction over approximately 0.25 AU at 1 AU, and a low proton temperature [Burlaga, 1988]. This is further characterised by Lepping *et al.* [1997] as the region between the leading half of the southward IMF B_z (known as geoeffective turning) and the trailing half which contained strong northward (geoineffective) field with an accompanied large density enhancement that strongly compressed the magnetosphere as illustrated in Figure 1.2. It was observed that there was smooth rotation of IMF from the southward to the northward direction. The density was also at a constant level throughout the MC passage while the solar wind speed was at over 400 km/s.

Table 1.1: Observed Properties of the Solar Wind near the Orbit of the Earth. Table from Kivelson and
Russell [1995].

Proton density	0.066 m^{-3}
Electron density	0.071 m^{-3}
He^{2+}	0.25^{-3}
Flow speed (nearly radia)	450 km/s
Proton temperature	1.2 x 10^5 K
Electron temperature	1.4 x 10^5 K
Magnetic field (induction)	7 x 10^{-9} T
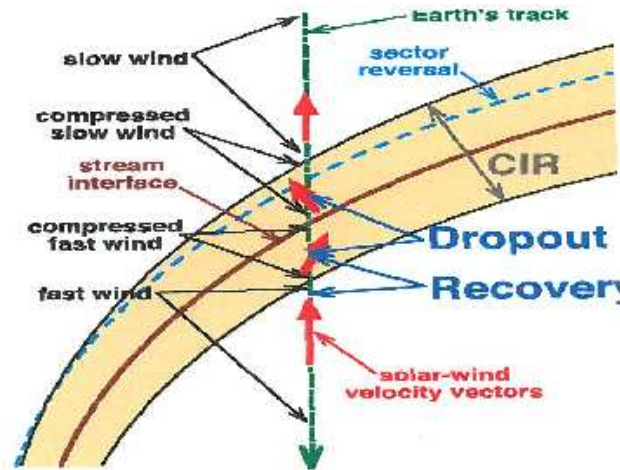
Figure 1.1: Schematic illustration of SI mechanism. From Borovsky and Denton [2010].

The magnetic clouds of the solar wind emerge from the corona [see Figure 1.3] and thus differ from
the turbulence within the ICME. There are different types of MC orientation; mostly southward and
northward types. The southward type involves smooth reversal of IMF B_z from the south to north while
the case is reverse for the later. At the rear part of the cloud, a large southward magnetic field is caused
by a shock compression. The shock intensified a pre-existing southward magnetic field thus increased
the geoeffectiveness of this event.
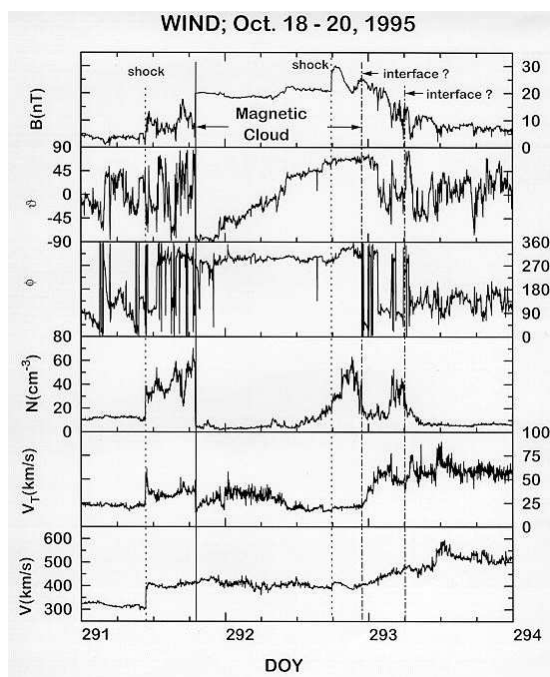
Figure 1.2: Magnetic and Solar wind Parameters showing conditions for MC occurrence. From (top to bottom) the magnetic field strength (B), the elevation (θ) and azimuth (ϕ) of the magnetic field direction, the proton density (N), the proton thermal speed (V_T) and the bulk velocity (V). From Lepping *et al.* [1997].
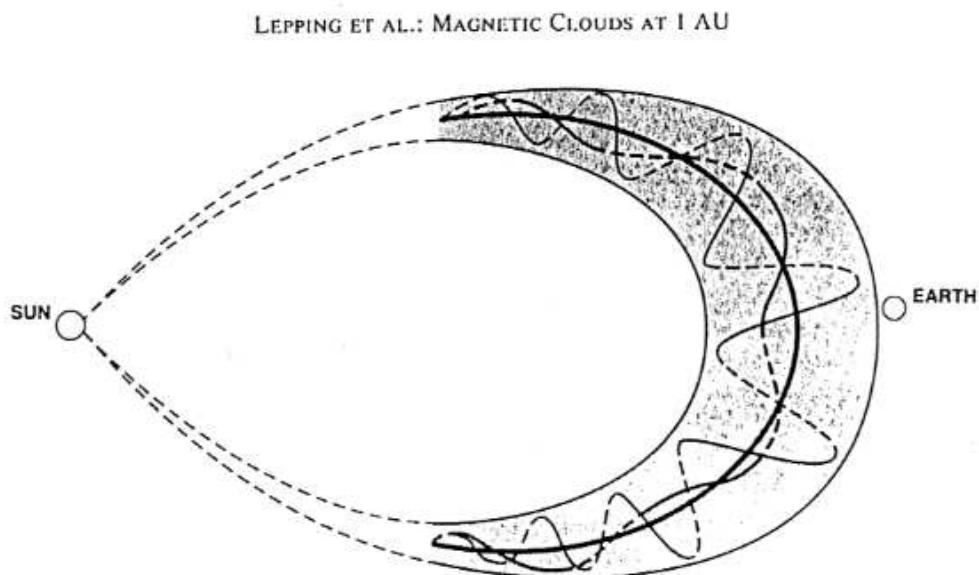
Figure 1.3: Schematic Diagram of Magnetic Cloud. From Lepping *et al.* [1990].

1.4   The Magnetosphere and Ionosphere

The Earth's space environment is divided into ionosphere, plasmasphere and magnetosphere based on the behaviour and number of free electrons and other charged particles as shown in Figure 1.4.
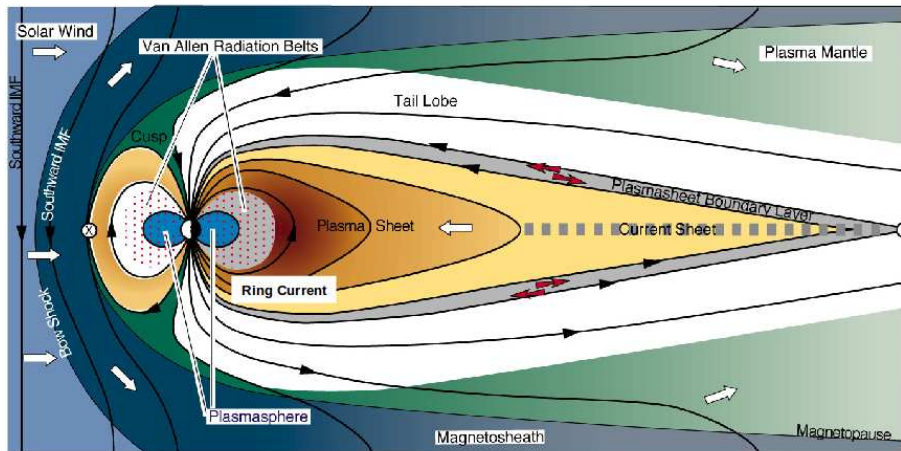
Figure 1.4: A simplified illustration of the main components of Solar wind and magnetosphere interactions. Figure after Hill and Dessler [1991].

1.4.1   Magnetic Field

The Earth has a magnetic field which is dipolar at small distances. It appears to be generated in the Earth's core by a dynamo process associated with the circulation of liquid metal in the core and driven by internal heat sources [Kivelson and Russell, 1995]. This magnetic field is surrounded in space by a region called the magnetosphere, which prevents most of the charged particles from the Sun, carried in the solar wind, from hitting the surface of Earth. The shape of Earth's magnetosphere is primarily determined by the distortion of the Earth's internal magnetic field, the solar wind plasma and the IMF. The Sun's solar wind significantly impacts the Earth's magnetic field. Instead of being a simple dipole, the Earth's magnetic field is compressed by the solar wind on the side facing the Sun and is stretched out on the opposite side called the magnetotail, which extends to tens of Earth radii (R_E).

The Earth's magnetic field lines can be particularly described by the L- value parameter. The Earth's magnetic field lines crossing the equator at a number of R_E is equivalent to the L-value. Apart from using L-value to formally define the Earth's true instantaneous magnetic field, it can also be used to understand magnetic phenomena near the Earth. So, in some cases of near Earth probing, the L-value is approximated using the dipole model of Earth's magnetic field. The dipole model is the first order approximation of the true Earth's magnetic field in a complex state. This complexity of field involves the effects of the IMF and the solar wind resulting into inaccurate values at higher L-shells. An example of such approximation is L^* [Morley *et al.*, 2010b]. In a simple dipole field, L^* is the representation of the drift shell at the magnetic equator [Varotsou *et al.*, 2008].

1.4.2   Ionosphere

The ionosphere can be defined by energetic particle effects on radiowave propagation as a result of the presence and variation in the concentration of free electrons in the atmosphere. The ultraviolet (UV) emanating from the Sun heat the layer of neutral atmosphere and ionizes it. The ionosphere is the ionised upper layer of the Earth's atmosphere lying between about 50 km and 1000 km of Earth's atmosphere. Ionizing particles can also come from the magnetosphere, or from the ionosphere itself if a process for local electron acceleration is operating.

Considering the density variation, the ionosphere can generally be considered as a series of horizontal layers that vary with time and geographical location. The ionosphere however, does not always conform to this simple description, particularly in the equatorial and polar regions. To characterise its behaviour, the ionosphere can be divided into the equatorial, the mid latitude and the polar regions, with the mid latitude region being the 'best behaved' and easier to study, while the polar and equatorial region ionospheres are both subject to a wider range of unexpected behaviour. The different zones of the ionosphere are characterised by different ionospheric conditions, the major cause of this being the Sun. These variations are a result of the fact that the Sun is directly overhead in the equatorial region with the incident rays almost perpendicular to the surface of the Earth. Ionisation is higher in the equatorial region than in the mid-latitude and the polar regions, where the polar ionosphere is less dense.

The structure and variability of the ionosphere are not only controlled by the solar radiation, but also by other solar dynamics [Callis *et al.*, 1991] like the solar wind and its embedded magnetic field, and also by the Earth's magnetic field. There are events (such as SI and MC) of enhanced energy input and ionisation whose major source is the energetic particles from the Sun and the magnetosphere precipitating into the ionosphere. The electrons trapped in the outer radiation belts get lost and interact with the neutral particles in the atmosphere. This is most prevalent near the mirror points in the polar regions where the trapped electrons reach their closest approach to the surface of the Earth. Electrons with energies that range from hundreds of eV to several thousand keV deposit energy into the upper ionosphere and the thermosphere. The electrons lose some of their energy to the molecules producing such effects as excitation, ionisation, dissociation and subsequent emission of radiation and heating. The density of the neutral atmosphere is negligible at great heights but it increases as the altitude decreases.

1.4.3 Plasmasphere

The plasmasphere is made of high densities ($\sim 10 \text{ m}^{-3}$) of cold (~ 1 eV) plasma [Olasen *et al.*, 1987]. The plasmasphere is a magnetic field aligned structure that can be traced all the way from the equatorial plane to the ionosphere. It has a very sharp outer edge called the plasmapause where the dense cold plasma is usually terminated. The innermost part of the plasmasphere does not depend strongly and systematically on geomagnetic activity. The density declines gradually with increasing radial distance. In times of strong magnetospheric activity, strong convection, strips flux tubes away from the outer plasmasphere. After a sustained period of high activity, the outer plasmasphere is observed to refill gradually, over a period of a few days.

1.4.4 Magnetosphere

The magnetosphere may be defined as that region surrounding Earth in which charged particles are affected by the Earth's magnetic field. The magnetic field creates a magnetic bubble that is continually struck by the solar wind. The solar wind is largely deflected around the magnetosphere and thus, distorts its shape, creating a shock wave facing the Sun and a long magnetic tail that stretches away from the planet. The plasma sheet, as indicated by red arrows in Figure 1.4, constitutes the third main reservoir of plasma. It is a region of hot plasma where the energy density remains approximately constant in quiet magnetospheric conditions. With satellite observations, plasma sheet characteristics are well documented with electron energies ranging from 100-500 eV and higher densities of electrons up to 10^6 cm^{-3} [Borovsky and Denton, 2008]. In describing interactions between the solar wind and the Earth's magnetosphere two coordinate systems are employed: geocentric solar-ecliptic (GSE) and geocentric solar magnetospheric (GSM) coordinates. Both coordinate systems have their origin at the center of the Earth with the X-axis toward the center of the Sun. In GSE the Z axis is normal to the ecliptic plane and positive toward the north. The Y that completes the right hand system is positive toward the dusk. In GSM the Z axis is coplanar with the Earth's magnetic axis and the X axis. The Y completes the right hand coordinate system.

The magnetosphere is shaped like an elongated teardrop with a tail pointing away from the Sun. The uppermost boundary called magnetopause is typically located at about 10 Earth Radii R$_E$ above the Earth's surface on the day side. Beyond the magnetopause are the magnetosheath and bow shock.

1.4.5 The Radiation Belts

The radiation belts consist of energetic electrons and protons that are trapped in a doughnut-shaped region centered around the Earth.

Particles in the Earth's magnetosphere can undergo three types of motions from interactions with Earth's magnetic field. These types of motion are illustrated in Figure 1.5. First, due to the Lorentz force (F)

$$\vec{F} = q(\vec{E} + \vec{V} + \vec{B}),$$

a charged particle (q) with a perpendicular component of velocity ($\vec{V}$) will gyrate around the magnetic field ($\vec{B}$) line due to the electric field ($\vec{E}$). This motion makes electrons to spiral around the magnetic field lines since they can not move across them easily.

The second particle motion, bounce motion, is determined by the gradient force

$$\vec{F} = -(\mu\nabla)\vec{B},$$

where μ is the magnetic moment. The magnetic moment is the first adiabatic invariant, which means that the particle's perpendicular energy is proportional to the magnetic field strength. This means that as the particle travels into regions where the magnetic field is stronger (toward the pole), the perpendicular velocity increases. The result is a decrease in the parallel velocity until the gradient force reverses the particle back along the field line to travel towards the opposite pole. This place where the particle is pushed back along the field line is called the mirror point. The bouncing motion brings the particles closer to the surface of the Earth as they move northward or southward away from the equator because of the curvature of the magnetic field lines. A single particle undergoes a third motion called the drift motion, where particles drift around the Earth relatively slowly. This is due to both curvature and gradient of the magnetic field.

Due to the forces from the magnetic field as mentioned above, highly energetic particles can become trapped in the Earth's radiation belt. The Van Allen radiation belt is classified into two as shown in Figure 1.6. Inner radiation belt and outer radiation belts separated by region of low density called slot region (usually between $L = 2.5$ and $L = 3$). Depending on the magnetic field line, the inner radiation belt is commonly between $L = 1.2$ and $L = 2.5$ away from the center of the Earth. It contains mainly proton and ion populations which are relatively stable. The formation of inner radiation belt is due to the influence of losses due to Coulomb scattering and whistler mode pitch angle diffusion on slow inward radial diffusion [see, Ganushkina *et al.*, 2011]. Since it contains mostly somewhat stable proton populations, it is therefore not the area of concentration of this present work.

In the outer radiation belt which commonly fills a space between $L = 3$ and $L = 7$; however, there is a significant variation in its strength and size relative to geomagnetic activity, in particular, storms period [Millan and Thorne, 2007]. The outer radiation belts consist primarily of electrons with energies between 0.5 MeV and 10 MeV. Electrons from the solar wind and few from the ionosphere are sources of the outer radiation belt particles. These particles undergo acceleration by radial diffusion and wave particle interactions to reach relativistic energies. Radial diffusion involves large-scale fluctuating magnetic and electric fields responsible for acceleration of particles across magnetic field shells [Kivelson and Russell, 1995]. The diffusion accelerates the low energy solar wind to relativistic energies as they enter the radiation belt. Researchers have been concerned over the dynamics of outer electron radiation belts since many decades yet the dominant source and lost mechanism responsible for the dynamics is still in contest. The generation and decay of energetic particle populations in the radiation belts are still, after 50 years of research, not fully understood [see review by Friedel *et al.*, 2002].

1.4.6 Ring Current

The ring current is formed primarily through injection (via duskward electric field) and subsequent trapping of particles from the plasma sheet into the magnetosphere [Kamide *et al.*, 1998]. During the so-called substorm expansion, induction electric fields accelerate magnetospheric particles and inject them into the inner magnetosphere where they become trapped and ultimately form the ring current. The ring current system consists of a band, at a distance between $\sim 3R_E$ to $\sim 5R_E$. There is an
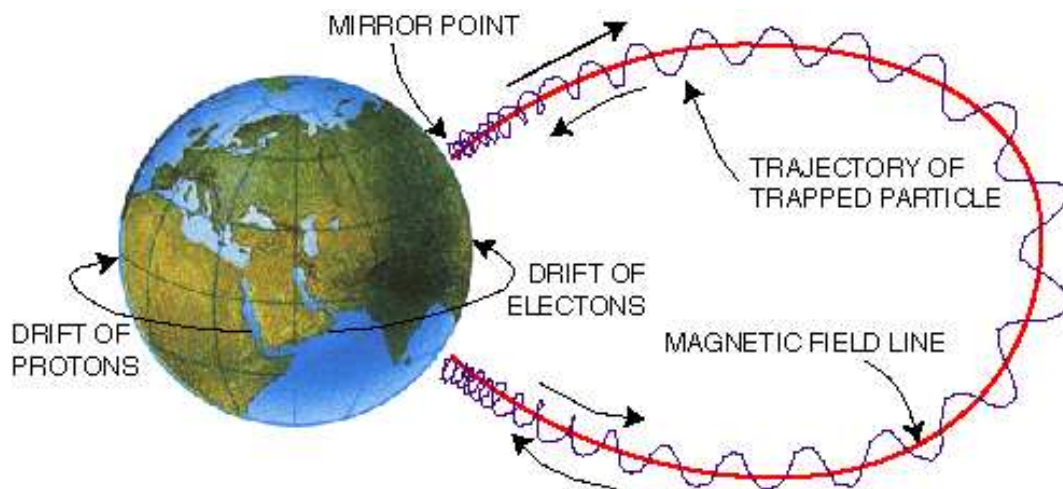
Figure 1.5: A simplified depiction of charged particle motion within the radiation belt, inluding the location of mirror point. Figure from from Baumjohann and Treumann [1996].
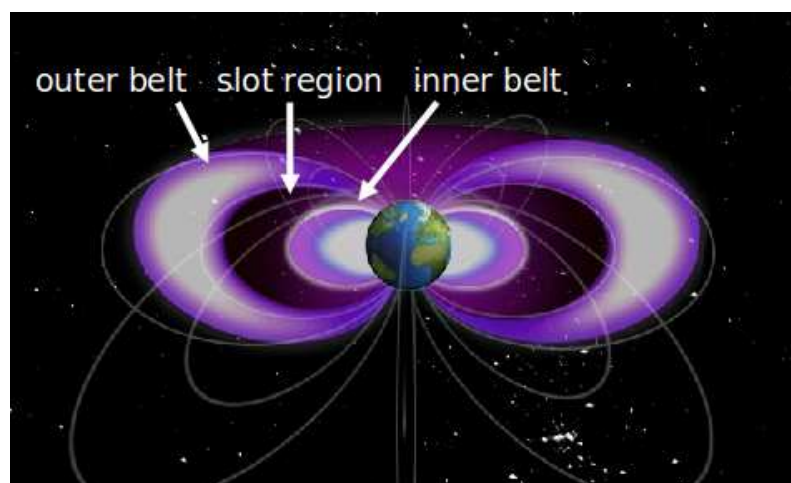
Figure 1.6: A graphical depiction of Van Allen radiation belts. Figure from `http://www.crystalinks.com/vanallenbelt.html`.

overlap between trapped charged-particles and ring currents. Most of the ring current is carried by these trapped particles, and all of the trapped particles contribute to the ring current. However, the term "ring current"emphasizes those components of the particle distribution that contribute importantly to the total current density which, for non-relativistic particles, is proportional to the energy density. The variation of ring current is reflected by the Dst index.

1.5 Magnetosphere – Ionosphere Coupling

In many cases, the boundary between magnetosphere and solar wind is well determined by pressure balance. The equilibrium is however, dynamic rather than static. The key electrodynamics element in the physical coupling between the ionosphere and the magnetosphere is the current flows along the two regions. These currents result from ionospheric convection which is driven by magnetospheric convection [Gold, 1959]. Magnetospheric convection is in turn driven by the solar wind. That is, electrons and other ions of high energy are extracted from the solar wind by the magnetosphere, and through an event of dropout, and other processes, some of the electrons are dissipated into the ionosphere. Early models predict viscous interactions, [Axford and Hines, 1961] and magnetic merging [Dungey, 1961], as the mechanisms responsible for transfer of energy. Later satellite observations suggest that both mechanisms are operative for magnetospheric convection and auroral particle energization but in more complex ways than envisaged by the early proponents [Russell and Elphic, 1979].

However, the space around Earth's atmosphere is alive and dynamic because the Earth's magnetic field reacts to changes in the solar wind. The interaction between the solar wind and the plasma of the magnetosphere acts like an electric generator, creating electric fields deep inside the magnetosphere. These fields in turn give rise to a general circulation of the plasma within the magnetosphere and accelerate some electrons and ions to higher energies. The magnetosphere is coupled to the ionosphere via magnetic field lines during enhanced magnetospheric convection, actions of substorm, inward radial difusion and inward movement of magnetopause among many others. During these processes, magnetospheric electric fields map down to the ionosphere, creating frictional heating and plasma instabilities. The coupling is also important in driving neutral atmospheric waves that affect the state and the dynamics of the ionosphere significantly.

1.6 Earth's Magnetic Field Variation and Storms

1.6.1 Storms

The Earth's magnetic field exhibit both regular daily variation and irregular disturbances. The disturbances are caused by interaction of solar wind with the Earth's magnetic field. Irregular magnetic disturbances do exhibit patterns in their frequency of occurrence. The main pattern is the correlation with the solar cycle and the 27-day rotation cycle and the number of irregular magnetic storm per year characterized by CME-driven storms and the 27-day solar recurrence of some storms which is typical of CIR-driven storms.

The strength and frequency of coronal activity also varies at solar maximum. Among these is the catastrophically ejected billion tons of particles with speeds of millions of km/h in the solar wind termed CMEs causing disruptions of various magnitudes on Earth. ICMEs are preceded in time by a sheath of compressed solar wind, which itself is often preceded by an interplanetary shock. The ICME storm components: shock, ejecta, sheath, and essentially, MC are refer to as CME-driven storms. The effects of ejected particles on interaction with the Earth's magnetic field are referred to as space weather.

1.6.2 Substorms

The basic disturbance in the magnetosphere, involving successive reconfigurations of the geomagnetic field and explosive dissipation of energy at the high-latitude ionosphere (auroral displays), the inner plasma sheet (acceleration of energetic ions) and the distant magnetotail (formation of magnetic neutral lines and plasmoids) is known as substorms [Kamide, 1992]. The energy is provided by the solar wind and is temporarily stored in the form of increased magnetic flux in the magnetotail. The storage of some of this energy in the Earth's magnetotail constitutes the first of the three phases of the substorm, the

growth phase. During the second phase, the expansion phase, the energy stored in the tail is released when the field lines in the inner magnetosphere relax from their stretched, tail-like configuration and quickly move into a more dipolar configuration. The third phase is the recovery phase, during which the magnetosphere returns to its quiet state.

1.7   Geomagnetic Indices

The geomagnetic variation can be measured by standard magnetograms. The magnetograms and the averaged data supplied by the magnetic observatories are too detailed for many purposes, and it has long been found useful to compute some numerical parameters that indicate the level of general magnetic variations or of specific types of disturbance. Storms are measured by the K-index which is the overall geomagnetic condition of the upper atmosphere over the past 3 hours and ranges quasi-logarithmically from 0 to 9. The Kp index (p for "planetary") is a measure of magnetospheric activity which indicates the strength of solar wind driving the magnetosphere. It is based on the data from 12 stations between geomagnetic latitudes of $48°$ and $63°$, selected for good longitude coverage. The most widely used and available index of low-latitude activity is the hourly Dst index. It is the magnitude of the normalized horizontal component of the equatorial magnetic field (axially symmetric disturbance). Dst is routinely obtained by mid-latitude observatories network of ground-based magnetometers which are located around the globe [McCreadie, 2001]. The Dst index was designed as a measure of magnetospheric ring current. Most of the activity indices increase with the square of solar wind velocity. However, almost no magnetic activity is seen unless the IMF embedded in the solar wind has a southward component, antiparallel to the Earth's magnetic field near the subsolar point on the dayside magnetopause. Understanding the state of IMF during high-speed stream interface is owed to its parker-spiral orientation seen in GSM coordinate [Borovsky and Denton, 2009]. This dependency is quantified in the half-wave rectifier model [Kivelson and Russell, 1995]. According to this model, whenever the IMF has a southward component, the activity is proportional to the cosine of the clock angle of the IMF around the Earth-Sun line. Even if the IMF is along the expected Archimedean spiral, a southward component can occur because of the orientation of the Earth's magnetic axis. Solar flares, CME and CIR can also generate substantial north-south components of the IMF.

1.8   Thesis Overview

The purpose of this study is to statistically examine the dependence of outer electron radiation belt dropouts during the interaction of the Earth's magnetosphere and solar wind. This coupling induces significant disturbances in the forms of Corotating Interaction Region (CIR), storms driven by Stream Interface (SI) and Coronal Mass Ejections (CME) storms driven by Magnetic Clouds (MCs). The level of precipitation into the atmosphere during these periods is also studied. This is achieved by, (i) collecting electron responses that are below satellite background and checking the corresponding solar wind structure for SI or MC and (ii) examining the state of the ionosphere from ground-based observations. Events of outer electron dropouts are identified and measured using Synchronous Orbit Particle Analyser (SOPA) while the solar wind conditions and geophysical parameters during the events are determined using the OMNI-2 dataset. The state of precipitation and ionospheric absorption during this time is investigated using Finnish chain of riometers. The specific areas upon which attention is focused are: (i) characteristics of solar wind conditions and geophysical properties. (ii) determination of temporal and energy dependency of the dropouts and (iii) investigation of ionospheric responses.

Dropouts involve lost of electron fluxes from the outer radiation belt at the main phase of a storm and subsequent recovery. The characteristics of the dropouts are many and varied. Geomagnetic storms triggered both by ICMEs and CIRs lead to enhanced losses from the radiation belts [e.g, Clilverd *et al.*, 2010b] into the atmosphere. Outer electron radiation belt dropouts have been primarily associated with high magnetospheric convection and build up of the ring current during storms and the subsequent decrease in the magnetic field strength in the inner magnetosphere. Because of the repeating sequence of solar wind types that pass the Earth [Borovsky and Denton, 2009], both SIs and MCs are particularly amenable to statistical studies such as Superposed Epoch Analysis (SEA).

One of the primary effects of space weather depends on outer electron radiation belt dropouts which can cause significant hazards to Earth-based and space-based assets. The activation of space weather

effects due to dropouts is important in some of the following ways:

- They can penetrate into the ionosphere causing long duration ionospheric disturbances [Basu *et al.*, 1999] that adversely affect the ionospheric density and produce phase fluctuations that may cause significant degradation of GNSS radio signals leading to the lost of signal lock.

- The recovery of dropouts can produce high fluxes of relativistic electrons often referred as "killer electrons"[Horne, 2007] and extra hot plasma sheets that can cause anomalous spacecraft charging and subsequent discharges that can cause logic errors and malfunctions. Dangerous levels of radiation can be hazardous to pilots, passengers and men in space.

- The deposition of outer zone electrons into the atmosphere may induce the generation of NO_x (odd nitrogen) which could cause substantial decrease in stratospheric ozone (O_3) [Rodger *et al.*, 2010b].

1.9   Thesis Structure

This study statistically analyses the dropout characteristics particular to SIs and MCs including the local time dependency by examining some case studies as well as estimating possible precipitation into the atmosphere. Some of the results for the SI are well known from previous analyses [e.g, Borovsky and Denton, 2009; Morley *et al.*, 2010b]. However, this study has extended the previous work by including the behavior of the outer electron dropouts for MC (not previously established), and of several magnetospheric activity indices. The thesis is organised as follows: Chapter 2 presents the context of electron dropouts, plasma waves and interaction with particles. Chapter 3 describes the data and analysis techniques. Chapter 4 applies the techniques in Chapter 3 to the SI-driven dropouts earlier identified by Morley *et al.* [2010b] to statistically determine the equatorial and LEO responses. In chapter 5, some selected case studies of SI-driven dropouts are presented with discussion. Chapter 6 uses the procedures in chapter 5 to some selected cases of MC-driven dropouts. Using the techniques developed in Chapter 4, Chapter 7 presents a qualitative comparison of the overall selected dropouts and the state of ionospheric responses during the two distinct geomagnetic storm drivers. Chapter 8 summarizes the results, compares these results with those of related research and concludes with a discussion of future extensions to this work.

Chapter 2

Electron Dropout and Wave-Particle Interactions

This Chapter reviews past works on electron dropouts and precipitation with the factors that lead to the occurrence of the dropouts and precipitation.

2.1 Wave-Particle Interactions

Wave-particle interaction is a process whereby the wave fields interact with the particles' momenta and energies resulting in scattering of energetic particles from the outer radiation belt [Tsurutani and Lakhina, 1997]. One type of such interaction process between a wave and a charged particle is cyclotron wave-particle interaction. This process can cause the precipitation of energetic charged particles into the ionosphere. This phenomenon is due to the existence of a mechanism that provides pitch angle diffusion of the energetic electrons into the lost cone. In such a mechanism, pitch angle scattering will transport electrons from stably trapped orbits into the drift lost cone, and if the pitch angle becomes less than the local bounce lost cone, the electrons are lost to the atmosphere. Pitch angle scattering by wave particle interaction is an important transport mechanism for energetic electrons in the magnetosphere, as energetic particles are sensitive to pitch angle scattering. When the so called plasma waves interact with electrons, the rate of pitch angle scattering is enhanced relative to the rate of injection associated with radial diffusion or convection. Examples of these plasma waves interacting with the radiation belt electrons were further discussed in the following section.

2.2 Waves in the Magnetosphere

2.2.1 Whistler-mode chorus Waves

Whistler mode wave is quantitatively described in Helliwell [1965]. A right hand circularly polarised electromagnetic wave describes the phenomenon known as a whistler mode. This is the mode at which the Very Low Frequency (VLF) signals travel through a plasma medium. The same study of [Helliwell, 1965] described chorus as natural wave emissions generated by plasma instabilities in the Earth's magnetosphere observed first on the ground at middle and high latitudes. So, whistler-mode chorus waves are perhaps one of the most common and most intense natural plasma waves occurring in the Earth's outer magnetosphere. During magnetic storm recovery phase, any interaction involving whistler-mode chorus waves and radiation belt particles is capable of scattering energetic electrons into the lost cone resulting into ring current decay [Tsurutani and Lakhina, 1997].

Satellite observations have shown that chorus power fluxes increase outside the plasmasphere during enhanced geomagnetic activity [Meredith *et al.*, 2001]. Smith *et al.* [2004] showed that chorus power is initially depressed from the storm onset, reaching a minimum at about the time of the Dst minimum. This decrease in power on the ground may be due to propagation. In the recovery phase of the storm, chorus wave power rises above the prestorm level. Thus, any burst precipitation, and lost of radiation belt electrons observed outside the plasmapause will all amount to chorus effects. It may be worthwhile to note that Millan and Thorne [2007] required possible mechanisms capable to deplete the outer electron

radiation belt. The study noted that one of the possible candidate mechanisms for the scattering of relativistic electrons does not preclude whistler-mode chorus waves.

2.2.2 ULF Waves

ULF waves are one type of electromagnetic waves usually known as geomagnetic pulsations. A standard scenario involving ULF waves begins with the role in transporting magnetospheric energy to the ionosphere; determining the life time of trapped radiation; accelerating particles via resonance; and, perhaps, even in coupling the solar wind energy itself to the Earth's magnetosphere.

Past work shows that as the high-speed solar wind continues to buffet the magnetosphere, it can produce very strong ULF waves that, in turn, accelerate electrons to high energies. Horne *et al.* [2005] focused on the roles of ULF waves in radiation belt electron acceleration versus more localised heating and acceleration by higher-frequency waves resulting in particle energisation and lost. Other work in this area focused on understanding and quantifying ULF wave as a global mechanism. Ukhorskiy *et al.* [2005] for example found that large-scale ULF oscillations and waves can exhibit resonance with the drift-bounce motion of the outer belt electrons, which drives electron radial transport across their drift shells.

More recently, Loto'aniu *et al.* [2010] used both satellite and ground based observations to study lost of outer radiation belt electrons through the magnetopause in response to ULF. A two orders of magnitude decrease in 2 MeV electron flux which is attributed to rapid non-adiabatic lost process. ULF waves were observed in the afternoon to dusk sector from the magnetopause to GEO altitude. The rate of outward radial diffusion was estimated for MeV electrons using the observed ULF wave and diffusion time (about 2.5 hour) was found to be in good agreement with the observed time for non-adiabatic flux decrease at GEO. The magnetopause was compressed inside of its nominal position because of increased solar wind dynamic pressure. The electron lost is interpreted as a combination of magnetopause shadowing due to compressed magnetosphere and enhanced outward radial diffusion from ULF wave-particle drift resonant interactions. The fact that the magnetopause is compressed in response to high speed solar wind interface was also documented by Morley *et al.* [2010b].

2.2.3 EMIC Waves

According to Jacobs *et al.* [1964], one class of discrete electromagnetic emissions which mostly occur with the period of 0.2 to $10s$ (Pc 1–2) frequency range, is an left-hand polarized electromagnetic wave that propagates along field line towards the ionosphere. This wave type is called the Electromagnetic Ion Cyclotron (EMIC) wave. Early observations of these waves were made by magnetometers on the ground and sparked a theoretical paper by Kennel and Petschek [1966] which attempted to explain their generation. It is now generally accepted that generation of EMIC waves requires an anisotropic ($T_\perp > T_\parallel$) and energetic (10 - 100 keV) ion population. Since the phase velocity scales with the Alfvén velocity, the greatest amplification is expected to occur at the geomagnetic equator, where typically the magnetic field strength is lowest while the density is highest (along a particular field line).

From an extensive statistical study using ground-based data, Anderson *et al.* [1992] showed that in the Earth's magnetosphere, EMIC waves are typically observed at $L > 7$ in the post-noon MLT sector. Meredith *et al.* [2003] reported a tendency for the minimum energy for pitch-angle scattering of electrons by EMIC is above 2 MeV, but can be below this only for a small fraction of wave events, at a limited range of local times occurring during intervals of enhanced ring current. EMIC waves are of special importance in outer radiation belt physics and have long been suspected of being one of the major contributors to the lost of energetic particles via a resonant wave-particle interaction. When the resonance condition between the wave frequency and the gyrofrequency of the particle is met, the interaction changes the pitch-angle of these particles, eventually scattering them into the lost cone. The significance of energetic particle lost due to resonant interaction with EMIC waves in the overall balance of source and lost terms acting throughout the Earth's radiation belt is still an area of active research [e.g. Millan and Thorne, 2007].

There are some modeling efforts which try to predict the impact of EMIC waves on high-energy particles. Shprits *et al.* [2009] showed that EMIC waves can, by creating strong gradients in local time in the pitch angle distribution, cause lost even on the dawnside of the magnetosphere, although the EMIC wave occurrence was limited to the duskside in their model calculations. Earlier Li *et al.* [2007] had shown that effective pitch-angle scattering by EMIC waves is somewhat limited to regions of high-density plasma, which implies that plasmaspheric plumes may be during stormtime a prime location for relativistic particle lost. In order to accurately predict the effect of EMIC waves on energetic particle populations, models need to incorporate EMIC wave power values which are similar to those observed in the magnetosphere. Ukhorskiy *et al.* [2010] presented a case study of EMIC waves observed during the main phase of a storm. They were able to show that the wave amplitude and frequency are such that effective pitch angle scattering is predicted for electrons with energies as low as several hundred keV on a timescale of seconds.

From the characteristics of EMIC wave occurrence and the theoretical considerations it generally noted that particles injected onto the closed drift paths during high geomagnetic activity can only encounter EMIC wave at afternoon sector. Yue *et al.* [2011] statistically examined interplanetary shock (IP) with IMF B_z and observed denser and hotter GEO plasmas at pre-midnight with anisotropic temperature peaks at the noon region while it decreases to minimum at midnight. Their statistical observations suggested that, both EMIC and whisler waves can be mainly stimulated at the noon sector. This information are important for an accurate assessment of the role of EMIC waves on outer radiation belt electron lost. EMIC wave particle scattering generally cannot accurately explain outer radiation belt depletions at hundreds of keV. The frequency range of the EMIC waves varies depending on the local gyrofrequency. The range in the magnetosphere is about $0.1 - 5H_z$ known as Ultra Low Frequency (ULF) wave. Though other range such as Extreme Low Frequency (ELF) also exist but not relevant to this study. Due to its significance to the present work, details on ULF wave is provided in the next subsection. For more overview of EMIC wave, reader is referred to [Thorne, 2010].

2.3   Electron Precipitation

Precipitation involves the transfer of energy within the Earth's magnetosphere and into the high latitude ionosphere. The major source of enhanced ionisation in the ionosphere is as a result of the energetic particles depositing their energy in the upper atmosphere. Due to their small mass, electrons can be scattered through very large angles when they collide with the neutral particles in the atmosphere. If such deviations increase the pitch angle, it can lead to further penetration into the atmosphere causing the lost of more energy by collisions. On the other hand, if the deviations decrease the pitch angle, the electron is backscattered and will penetrate more on the other end of its bounce trajectory.

Baker and McPherron [1990] tested the response of the magnetosphere to the interplanetary shocks or pressure pulses which result in sudden injection of energetic particles into the inner magnetosphere. The interplanetary shock leads to changes in the magnetic and electric fields which are accompanied by the acceleration of energetic particles, thus leading to the injection of the particles into the inner magnetosphere. It was also noted that a strong interplanetary shock struck the Earth's magnetosphere and generated high fluxes of very energetic electrons observed in the inner magnetosphere.

As for high-speed solar wind and southward interplanetary magnetic field during magnetic storms, Baker [2001] finds that the intensity, spectrum and localisation of the precipitation into the inner magnetosphere are functions of the solar and geomagnetic activity. Energetic electrons play an important role in the transfer of energy within the Earth's magnetosphere and into the high latitude ionosphere. This transfer was associated with geoeffectiveness of interplanetary magnetic field. Clilverd *et al.* [2010a] noted that energetic electrons deposit their energy in the upper atmosphere and which serve as a major source of enhanced ionization in the ionosphere. Generally speaking, electron precipitation carries most of the particle energy and is the major driver of auroral emissions in the high-latitude ionosphere. Different classes of precipitation exist, and are probably due to different geomagnetic physical mechanisms acting at different locations. Distinguishing different types of precipitation under varying geomagnetic storm drivers will help quantify outer radiation belt dynamics.

2.3.1 Relativistic Electron Microbursts

Relativistic (> 1 MeV) electron microbursts (or short-duration bursts of precipitating relativistic electrons) with a duration of approximately 100 ms were observed to be characterized by sharp rise and slower decay and occasionally with a sawtooth pattern of precipitation. This pattern is an indication of depleted electrons from bounce lost cone. O'Brien *et al.* [2004] gave more evidence to pitch-angle of electron microburst precipitation. Microburst precipitation is associated with scattering by VLF chorus due to the similarity in their local time distributions. It was also noted that, scattering by whistler-mode chorus could be the mechanism responsible for relativistic electron microbursts, since both are often observed between 0300 and 1500 Magnetic Local Time (MLT). Relativistic (> 1 MeV) microbursts were observed to be correlated with chorus riser. Millan and Thorne [2007] gathered that satellites observe microbursts near the nightside trapping boundary and on the dayside at lower L shells. It was found that during high geomagnetic activity, microburst occurence are likely to be between $4 < L < 6$ with losses much stronger during the main phase of the activity, and are capable of emptying the outer radiation belts in a day or less. Morley *et al.* [2010b] in their observational study partially attributed electron microbursts as reponsible mechanism for the observed outer electron dropouts. Although in that work, the peak of absorption was observed from approximately 3 hours after the arrival of the onset of the storm driver, and thus coincides with the end of the interval of rapid lost.

2.4 Electron Dropouts

Dropouts as earlier stated is the lost of electrons from the outer radiation belt at the main phase of a storm event and subsequent recovery. Many observational and theoretical studies have examined the variations of outer radiation belt electron fluxes. In this section, only the most pertinent works are mentioned. The majority of the previous studies have looked at the enhancement while only few concentrated on the losses. Electron precipitation is the most acceptable type of radiation belt lost, but the source mechanisms are not fully understood. Quantifying satellite measurements of outer electron radiation belt dropouts can be used to help identify dominant radiation belt lost mechanisms when correlated with the behaviour of magnetospheric phenomena. For example, the initial onset and amplitude of dropout should correspond with the onset and amplitude in the proposed mechanism. Also, the observed energies should resemble the energies that the proposed mechanism can act on. Thus, satellite observations play a key role in discerning the dynamics of the outer radiation belt.

McIlwain [1972] was the first to observe decreases in the trapped flux and suggested adiabatic effect as the cause, or actual losses through either precipitation into atmosphere or lost through magnetopause (known as magnetopause shadowing). While this work generated much interest initially, later measurements have shown that some of the conditions for the mechanism are not generally present. A rare class of dropout phenomena has been associated with the entry of geosynchronous spacecraft into magnetospheric lobes as well as magnetopause crossings. Thomsen *et al.* [1994] studied the frequency of occurrence and the local time dependence of the magnetospheric lobe regions at GEO with satellite observation using energetic particle and field measurements. They proposed that a strong field alligned current system together with the storm-enhanced ring current caused the compression of the local plasma sheet.

Onsager *et al.* [2002] investigated the dependence of radiation belt electron dropouts on local time, radial distance, and particle-energy. They noted, that the initial dropouts were controlled by the adiabatic response called Dst effect and that non-adiabatic which involve interactions with various magnetospheric waves will eventually cause the lost of electrons from the magnetosphere. However, in the case of outer electron radiation belt dropout due to recurrent storms such as SI, the Dst effect is found to play an insignificant role [Borovsky and Denton, 2009]. Subsequent observational efforts have followed one of the main methods: classification based on adiabatic effects, and non-adiabatic effects.

More recently, a superposed epoch analysis (SEA) was performed to discern the dominant dropout mechanism during CIR. Borovsky and Denton [2009] found that the onset of dropout occurs after the passage of the IMF sector reversal prior to the passage of SI. The tendency for the dropouts begins during compressed slow solar wind while the recovery from dropouts commences during the passage of the compressed fast wind. Borovsky and Denton [2009] also documented typical chronology of a recurring HSSW cycle and the resulting geomagnetic activity, behaviour of the Earth's plasma sheet, drainage plumes, and phase of the relativistic-electron dropouts with the conclusion that EMIC waves

play key role in dropout occurrence. However, the study did not test the consistent response of dropouts to SI and MC events.

Despite extensive work describing the dropout signature [e.g Millan *et al.*, 2002; O'Brien *et al.*, 2004; Thorne *et al.*, 2005; Millan and Thorne, 2007] in response to geomagnetic storms, the most relevant is that of Morley *et al.* [2010b], in which SEA was employed in analysing satellite-based and ground-based observation of electron dropout responses to SIs. The study addressed whether there is a consistent radiation belt response to arrival of SI, how the response varies with drift shell and the statistical status of magnetopause during the arrival of SI. Their GPS observation is presented in Figure 2.1. The GPS measurements as presented were ordered by L^*. In the 230–410 keV of electron band as shown in Figure 2.1 (first panel) there is a strong tendency for electron counts to drop out at the arrival of the SI with a minimum in counts about 2 h after the SI. The effect is less pronounced deeper in the magnetosphere; the median dropout order at this energy ranges from 0.4 orders at $L^* = 4.5$ to 1.4 orders at $L^* = 6.5$. The electron counts tend to recover to pre-event levels in about a day. The median response at $L^* = 4.5$ shows a tendency to increased counts within several hours. Figure 2.1 (second panel) is superposed epoch data for the 0.77–1.25 Mev energy channel. The time of minimum electron counts is approximately 4–5 h after the epoch. This is delayed with respect to the lower energy channel by 2–3 h. The dropout also appears to move to lower L^* over several hours (on average), in contrast to the 230–410 keV channel where the dropout is nearly simultaneous across all L^*. The median dropout order at this energy ranges from 0.4 orders at $L^* = 4.5$ to 1.4 orders at $L^* = 6.5$. The lower L^* also shows a net increase in the electron counts, maximizing at $L^* = 4.8 - -5$. At $L^* = 6.5$ the electron counts only recover, on average, to their pre-event level. For this energy range the recovery takes an average of 2 days, but increases slightly with L^*. The response in the 1.7–2.2 Mev energy channel is as in Figure 2.1 (third panel). There is also an observed tendency to dropout, which remains pronounced to $L^* = 4$. The counts are near the noise floor from $L^* > 5.5$, but the time of minimum electron counts at $L^* = 4.5$ is about 7 h after epoch. The median dropout at this energy ranges from about 0.8 orders at $L^* = 4.5$ to 1.8 orders at $L^* = 5.5$. The recovery of these populations is also different. The time scale for recovery is extended beyond 3 days. The results of the observed dropouts were found to be energy and L^* dependent with an indication of outward diffusion and magnetopause shadowing.

The statistical average of > 30 keV ionospheric absorption for intervals centered on the set of SI to indicate regions of precipitation was also performed by Morley *et al.* [2010b] as shown in Figure 2.2. Absorption appears to increase (indicating the precipitation of > 30 keV electrons) around the time of epoch, and the precipitation becomes more strongly organized approximately 3 h after the SI and peaks at higher latitudes in the morning sector. The morning sector absorption remains elevated for at least 12 h after the arrival of the SI. Based on the riometer data, they suggest that the radiation belt losses can, at least in part, be explained for $5 < L < 6$ by a rapid and busty precipitation mechanism that is active in the late morning sector. A likely candidate responsible for such is relativistic electron microbursts since these normally occur outside the plasmapause. However, the work does not test the response on solar wind conditions and thus could cannot directly attribute the role of relativistic electron microburst as the mechanism responsible for rapid dropouts. However, they showed that the busty nature of the absorption and the spatial location are suggestive of electron microbursts driven by high-latitude chorus waves, which are generated off the magnetic equator in the late morning and on the day side. Thorne *et al.* [2005] had earlier confirmed the agreement of the lost rate of electrons due to microbursts with theoretical calculations of the lifetime based on quasi-linear scattering by field-aligned whistler waves during the October 1998 storm. This present study will further investigate electron dropouts in response to SI and MC during maximum and declining phases of solar cycle.
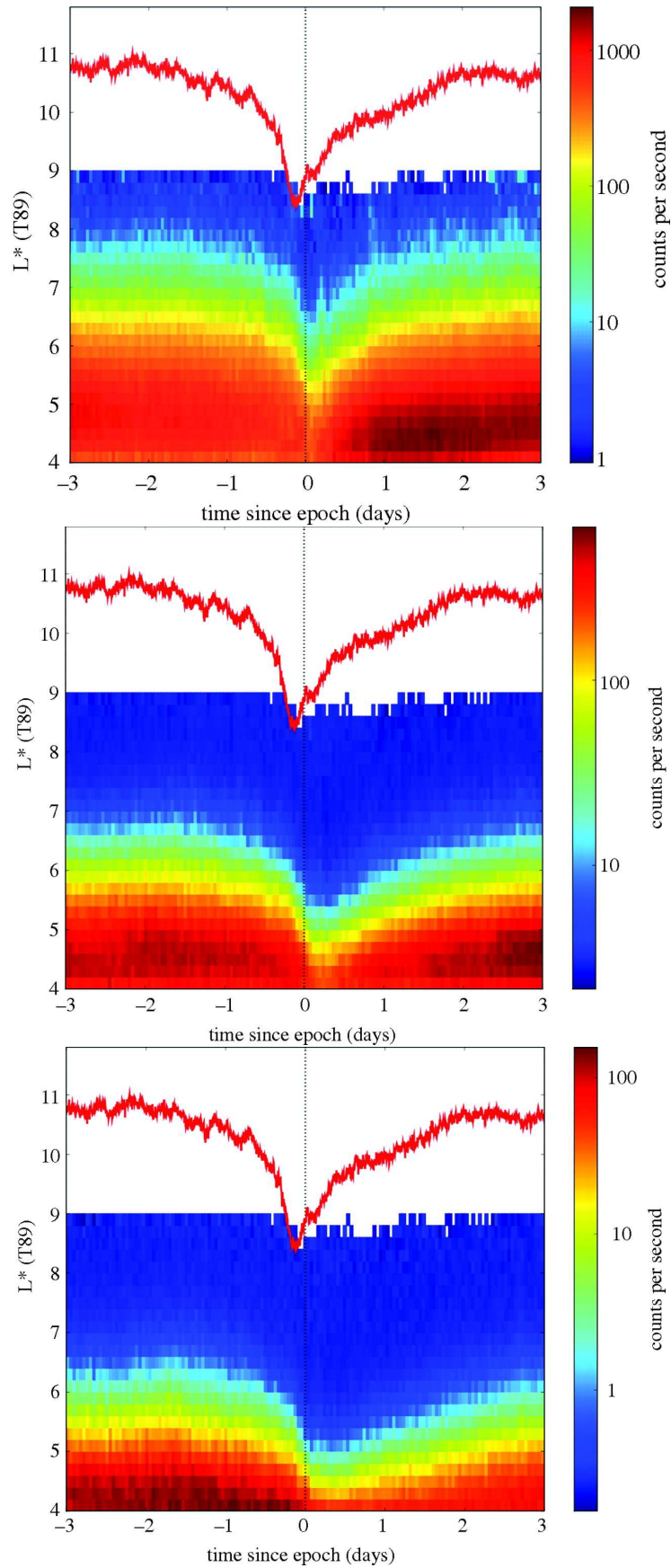
Figure 2.1: Two-dimensional SEA of electron counts as functions of L^* from combined X-ray dosimeters (CXD) onboard GPS . The abscissa is the time relative to epoch and the ordinate is L^*, calculated using the T89 magnetic field model and the ONERA library. (top to bottom) Electron counts from the 230–410 keV, 0.77–1.25 Mev, and 1.7–2.2 Mev energy channels. The overplotted red line shows the median standoff location of magnetopause. Figure from Morley *et al.* [2010b].
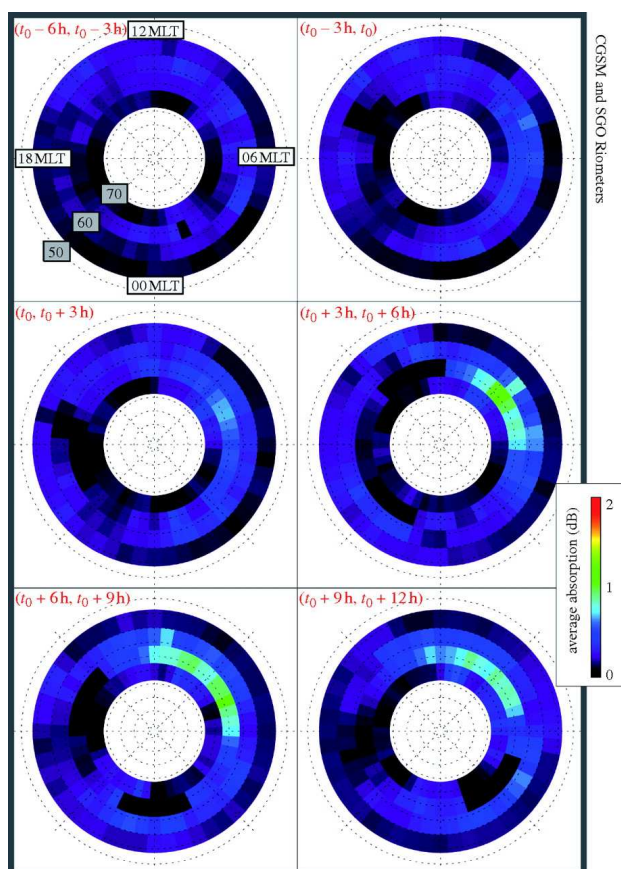
Figure 2.2: Maps of riometer absorption averaged over all 67 epochs, in 3 h time bins. Figure from Morley *et al.* [2010b].

Chapter 3

Data Description and Analysis Techniques

This chapter presents a description of the data used in this study. It also describes the procedure of event selection and techniques implemented to investigate the dropouts. Both satellite and ground based data sets were employed in this study.

3.1   Data Sets

3.1.1   LANL/SOPA Data

The first data set used for this study is provided by the Synchronous Orbit Particle Analyzer (SOPA) instruments on Los Almos National Laboratory (LANL) satellites in Geosynchronous Earth Orbit (GEO) meaning that they hover continuously over one position on the surface above the Earth. The interest in the LANL/SOPA data in the context of this study lies in the location of the satellites. GEO, at altitude of 6.6 R_E, lies near the outer edge of the radiation belts but still within the region of stable trapping for electrons and ions making it suitable for space weather applications. Also, an ideal location from which to study plasma sheet access to the inner magnetosphere as observed by Denton *et al.* [2006]. Apart from knowing the morphology of the region, understanding the cause and effects of depletion of electrons from outer radiation belts requires knowledge of the electron energy above keV and its temporal evolution. At every 10.24 seconds, SOPA instruments provide high spatial, high resolution measurements of differential electron fluxes from 50 keV to greater than 1.5 Mev in 12 channels using the three telescopes mounted at 0°, 30°, and 60°. The SOPA telescopes are actively controlled such that the spin axis of the satellite points continuously toward the center of the Earth. The SOPA flux measurements used for study were from four electron channels 225–315 KeV, 315–500 keV, 0.75-1.1 Mev and 1.1–1.5 Mev.

Seven SOPA equipped satellites have been in operation, beginning in 1989. Data are mostly received from three or four satellites simultaneously [Belian *et al.*, 1992]. The satellites with SOPA instruments are 1989–046, 1990–080, 1991-095, 1994-084, LANL 97A, LANL 01A, and LANL 02A. For every operational satellite, flux data were normalised to obtain the same yearly averaged logarithm [Belian *et al.*, 1992]. It is possible to obtain logarithmic average by summation of log-fluxes divided by the number of satellites per time [Borovsky and Denton, 2009].

SOPA summary plots were used to determine which satellites were providing data at a particular time and where they were located with respect to local time. SOPA data was acquired from `http://leadbelly.lanl.gov`.

3.1.2   GOES Data

Geostationary Operational Environmental Satellites (GOES) circle the Earth. The combined GOES satellite proton and electron data serve as an overview of the current satellite environment, particularly at geosynchronous altitude. Although the LANL satellites are also in GEO but the quick look plot from the SOPA instruments onboard does not easily identify Solar Proton Event (SPE). Since this study is

on the electron dropouts, GOES environment plots were checked for proton level that was above the satellite threshold and then filtered.

3.1.3   NOAA/POES Data
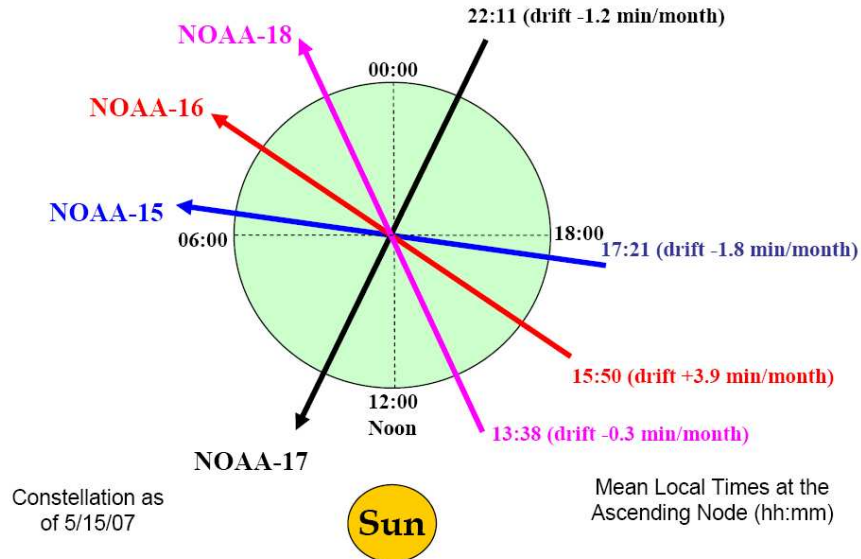
Figure 3.1: Schematic illustration of NOAA satellites passing the equator (from `http://noaa///nesdis/oso.html`).

NOAA/POES are the National Oceanic and Atmospheric Administration Polar Orbiting Environmental Satellites (POES). The POES, a polar-orbiting, Sun-synchronous, low-altitude (850 km) with a period of about 100 minutes satellite, has on-board the Medium Energy Proton and Electron Detector (MEPED) that monitors the intensities of charged particle radiation at higher energies. There are four POES, currently in orbit (see Figure 3.1). The satellites are named chronologically, based on launch date. POES 15 was launched in 1998, POES 16 was launched in 2000, POES 17 was launched in 2002 and POES 18 was launched in 2005. POES (15-18) orbit the Earth in such a way that they pass over the poles, thus, observe a wider range of L values and MLT. The MEPED on each satellite provides directional (0° telescopes for precipitating and 90° for trapped) measurements of energetic electrons but with proton contamination. This study applies correction to remove protons from the precipitating electron data. For this correction purpose, data from 0° telescope was selected only when it is measuring electrons inside the loss cone.

The fidelity of reducing proton contamination, thus, ensuring accurate measure of precipitating electrons is obtained from Lam *et al.* [2010]. The suggested first order correction,

$$\propto +15° < \propto_{LC} \tag{3.1}$$

was employed where $\propto$ is the local particle pitch angle at the satellite, $\propto_{Lc}$ is the edge of the loss cone, while the telescope opening angle is 15°. Assuming conservation of the first adiabatic invariant, the local pitch angle at the satellite, equivalent to the edge of the loss cone was determined by

$$\propto_{Lc} = \sqrt{\frac{B_{sat}}{B_{120}}} \tag{3.2}$$

Both the ambient magnetic field at the spacecraft B_{sat} and the ambient magnetic field at the foot of the field line which intersects ~ 120 km above the Earth are obtained from International Geomagnetic Reference Field (IGRF) model. To further ensure subtraction of protons from electron channel, the counts from 0° telescope were inspected to ensure that counts in the $E > 100$ keV channel are less

or equal to the counts in the $E > 30$ keV channels. This is reasonable since the precipitating electron counts rapidly decreases with increasing energy. With POES satellites, the superposed epoch is organised across all MLT such that at any given MLT, one of the POES satellite provides coverage. This study also examined the degree of relationship between trapped and precipitating electron flux. For more information on POES satellite data sets, the reader is referred to Rodger *et al.* [2010a].

3.1.4 OMNI Data

Other data sets consist of measurements of near-Earth solar wind, magnetic field and plasma parameters found in the OMNI database. These provide the geophysical data to build a picture of the response of Earth's magnetosphere to dropouts and particle precipitation. The OMNI database is an hourly resolution, multi-source data set from different instruments with coverage from November 1963. Higher temporal resolution versions of the OMNI database exist, but with coverage from 1995 [King and Papitashvili, 2005]. The data set was created at NSSDC by interspersing, after cross-normalizing, field and plasma data from each of several spacecrafts. OMNIWeb is a distributed network of synchronous databases designed to allow solar-terrestrial physics reseachers and customers to access all parameters necessary for solar wind-magnetospheric observations and modelling. The OMNI data sets used in this study were downloaded from the NSSDC OMNIWeb at `http://mniweb.gsfc.nasa.gov`.

Also included in OMNI data set since its creation are activity indices, providing state of ring current and magnetospheric convection among several others. From about 51 different parameters available at OMNI, only those that are relevant to this study were extracted. Of relevance are the IMF B_z, proton density, solar wind azimuthal velocity (GSE-V_y), solarwind radial velocity (GSE-V_x), solar wind pressure (nPa) and Alfvén Mach number (M_A). Hydrodynamic waves propagate with the speed called called the Alfvén speed. An Alfvén wave in a plasma is characterised by low frequency traveling oscillations of the ions and magnetic filed. Typical Alfvén speed is at ~ 40 km/s. Thus, in a case of average solar wind moving at speed of 400 km/s, the value Alfvén speed in it will be 10. This resulting value is refereed to as the M_A.

3.1.5 Riometer Data

Another data set used in the present study is measurements made with ground-based Riometers (Relative Ionospheric Opacity METERs) from the Finnish Riometer chain. With these observations, the state of the ionosphere during SIs- and MC-driven storms is investigated.

Remote sensing of electromagnetic waves of cosmic origin is a technique widely used to study the state and structure of the ionosphere. Riometers provide means of detecting particle precipitation into the atmosphere. Riometers respond to the integrated absorption of cosmic ray noise through the ionosphere [see, Clilverd *et al.*, 2010a] but electron density at heights where the electron motion is collision dominated. Riometers are mostly widebeam, typically 30 MHz and sensitive to any incident particle population capable of reaching the ionosphere in the range of 70–100 km (that is, D–region), empirically determined to be greater than 30 keV electrons or Mev protons [Clilverd *et al.*, 2010a]. Generally, riometers cannot resolve the individual particle populations detected, but the use of presence (or absence) of riometer absorption during an event is employed as a robust indicator of precipitation of high energy electrons [Morley *et al.*, 2010b].

The amount of the background cosmic radio noise disrupting the ionosphere is known to be a constant for a particular location and given (sidereal) time of the day. In order to identify extraordinary absorption, a reference Quiet Day Curve (QDC) is of importance. Any deviations from this expected value must then be due to absorption in the ionosphere. The riometer techniques is such that it achieves high gain stability by switching rapidly between the antenna and a local noise source. The power output of the noise source corresponds to that received by the antenna. The current through the noise source is recorded and this is monotonically related to the power output. So, by using the received power from an inactive period the general background absorption can be removed and only the variation above this level will be considered. Figure 3.2 illustrate a typical QDC fitting to only the data that are deemed to be quiet. Little activity is observed as seen in the received power versus time plot. However, overlapping of both the QDC and received power noise discontinued around 22:15 UT as shown in Figure 3.2. Therefore,

the noisy signal at around 22:15 UT indicates ionospheric absorption. This study make use of absorption data from the chain of Finnish riometers.
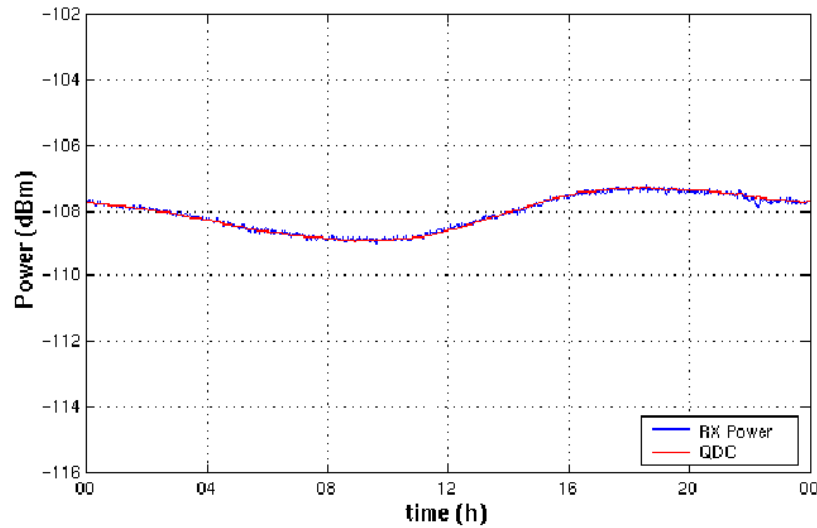
Figure 3.2: A quite day curve. The noise level of the received power (blue line) and QDC for days that are quite (red). Figure from `http://spears.lancs.ac.uk/data/summary/interpret/quiet.`

Beginning in 1970, the Finnish Riometer Chain maintained across a wide latitudinal range which includes sites in Ivalo, Sodankylä, Rovanlemi, Oulu, Jyväskylä and Nurmijärvi with additional riometers operating in Vidsel and Abisko in Norway, in Svalbard, and that of Iris in Kilpisjärvi. Figure 3.3 shows map of the location of Finish Riometer chain used in this study. The Finnish Riometer Chain is maintained by the Sodankylä Geophysical Observatory (SGO). Data is accessed as well as some vital information, from SGO website: `http://www.sgo.fi/Data/Riometer/riometer.php.`

Particle precipitation increases in frequency and magnitude during high activities leading to ionospheric irregularities. These irregularities can be observed in riometer measurements given in absorption intensity form. Example of QDC absorption intensity is seen in Figure 3.4. Absorption peaks at all Finnish riometers between 7–10 UT on 10 January 1997. Any significant correlations between these ionospheric absorption peaks and the outer electron dropouts will indicate the effects that the dropouts have during the storm drivers of interest.
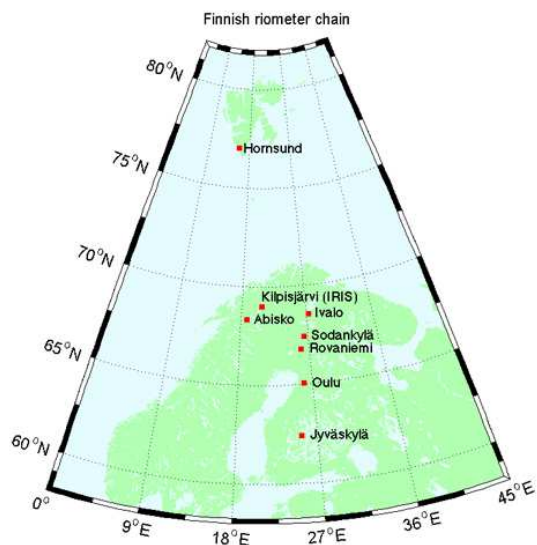
Figure 3.3: Finish riometers, a graphical map showing locations of active riometers. Figure from `http://www.sgo.fi/Data/Riometer/riometer.php`.
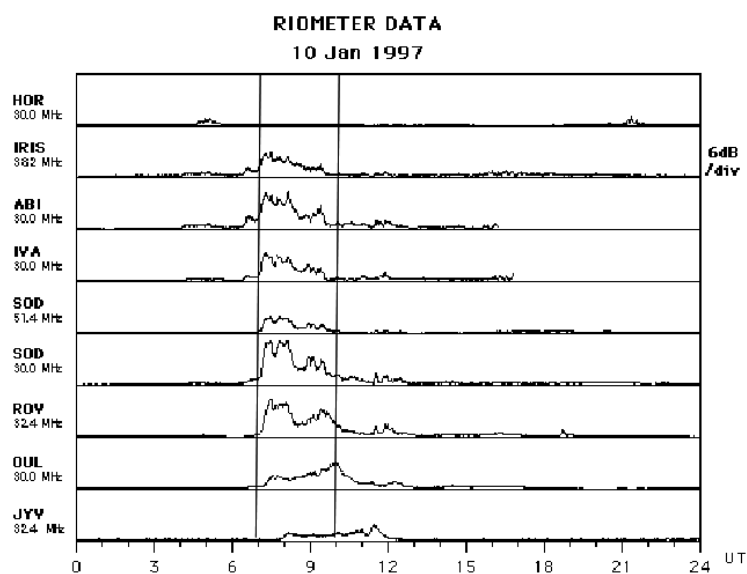
Figure 3.4: A typical sample of riometer absorption from Finish chain of riometers.

3.2   Event Selection Procedure and Techniques

3.2.1   Event Selection and Cleaning
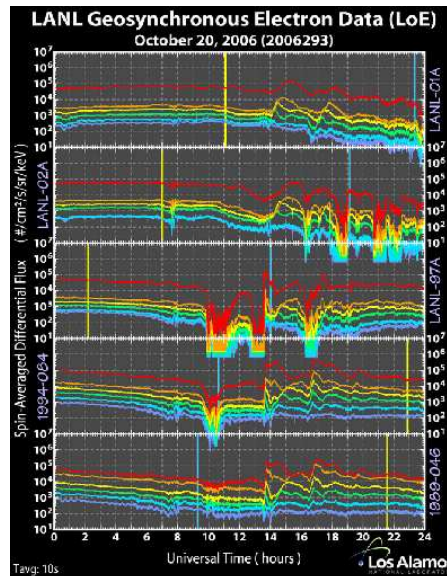
Figure 3.5: An example of a dropout. The panels reflect (from top to bottom) the fluxes on LANL 01A, 02A, 97A, 1994–084 and LANL 1980-046. The plot below the threshold line at each satellite indicates dropout. Local noon and midnight are respectively indicated by the yellow and blue vertical lines at each of the plots. Figure from `http://summary_plot_chose.html`.

The first step undertaken was to select particle dropouts by visual inspection of hourly quick look plots of SOPA satellite fluxes at all energies. Events were classified as particle dropouts only when fluxes drop to background levels across a wide energy range [Fennell *et al.*, 1996; Belian *et al.*, 1992]. The inclusion of plots from three or four SOPA satellites helped to identify dropouts across GEO. In order to study the local time difference of SOPA satellites, the start and end time can not be directly recorded as one satellite could observe the dropout at local noon while other could be at midnight and still observed the same dropout. However, this study used various SOPA satellite data to measure the flux levels at all local times using the onset of events as presented in the following chapters. Figure 3.5 presents an example of the flux dropouts for 20 October 2006.

Since the SIs and MCs are solar cycle dependent, dropouts events were collected from 1996 to 2007 in order to have clear understanding of the variability of occurrence in maximum and declining phase of the solar activity. The following criteria were then further imposed:

- There is no dropout a day before or a day after because it is sufficiently close to be considered a duplicate event or could be due to other processes.

- There is no proton contamination. This is achieved by checking NOAA space environment for any known solar proton events. Figure 3.6 shows a graph of typical solar proton event from NOAA space environment available at `http://www.swpc.noaa.gov/ftpmenu/index.html`.

- There is a clear signature of either SI or MC during the dropout. This is achieved by examining solar wind conditions and geomagnetic data at the day of dropout. It should also be noted that MC referred to in this study are of southward type.

204 dropouts were initially identified from 1996 to 2007. The selection criteria above were then applied. 17 were discarded as duplicates or due to other factors while 25 were eliminated as proton contaminated events and another 17 were avoided as unclear signature of SI or MC leaving total of 145 cleaned dropouts from which 80 were classified as SI-driven dropouts and the other 65 dropouts as MC-driven. The cleaned events and associated solar wind structures are listed in Table 3.1.

The second step involves the measurements of electron fluxes at (1) time of SI driven dropouts and (2) time of MC driven dropouts. Flux measurements on each of the instruments in operation were normalised for each year so as to have the same yearly averaged logarithm of flux in the dawn sector. In addition, 3 hourly averages of the measurements on each satellite were used to construct a multispacecraft logarithmic average. A SEA was then performed.

The riometer data were examined for any indication of particle precipitation during the events. Particle precipitation is indicated by a peak in absorption.
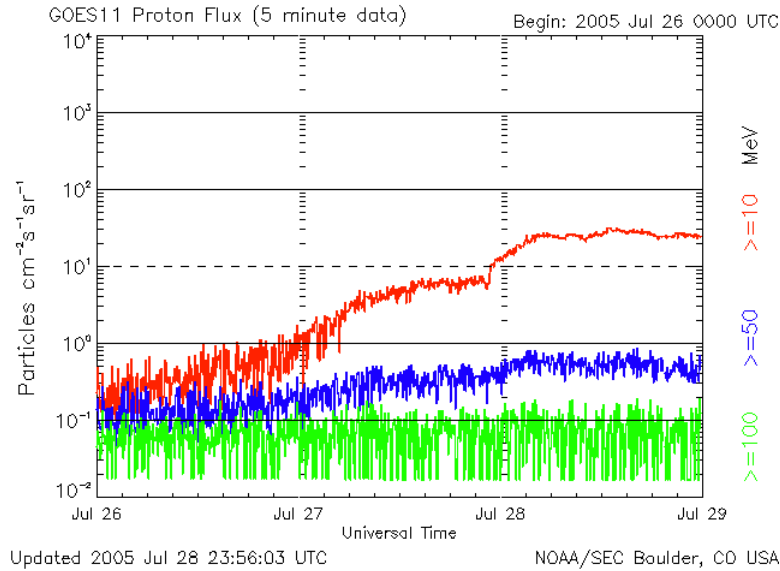
Figure 3.6: Graph illustrating solar proton event. The red line plot beyond the threshold indicates proton flux, blue is electron and green is ions.

3.2.2   SEA Technique

One method for composition of time series data is called Superposed Epoch Analysis (SEA) technique. This technique is used to reveal consistent responses, relative to some repeatable phenomenon, in noisy data [Chree, 1908]. It consists of sorting data into categories (key events) and comparing means for different categories. The technique is such that data are averaged in relation to the event, the consistent event signal will remain and random influences will tend to average out. SEA makes no assumption of linearity, and its use in this study is justified as a good technique at separating signals from noise from a large data set. The reference time as zero time of SEA allows one to investigate onset of interplanetary sources and the initial part of the events.

Because of the repeatable nature of SIs and MCs as storm drivers they are amenable to SEA. The choice of reference (zero) time for SEA is important and substantially influences the results [Borovsky and Denton, 2009]. In this study, time series of the variables under investigation are extracted from a window around the epoch (the SI amd MC) and all data at a given time relative to epoch form the sample of events at that lag. The data at each time lag are then averaged so that fluctuations not consistent about the epoch cancel. The reference time is based on:

- Onset of SI driven dropouts as determined by the deflection of solar wind azimuthal velocity (that is, reversal of GSE-Vy),

- Onset of MC driven dropouts as determined by the reversal of IMF Bz (smooth rotation of IMF B_z rotation from south to north).

It is highly desirable to have some believable hypotheses for why the event should affect the SEA variables, otherwise there will be a risk of finding a statistical coincidence with no physical meaning. Thus, a

statistical significant test is carried out by estimating the probability that the signal obtained from the SEA arose by chance using the first and third quartiles.

Table 3.1: Selected dropouts and associated solar wind structure from 1996-2007 used for study. DOY is day of the year and SWS is Solar Wind Structure

SN	Year	DOY	SWS	SN	Year	DOY	SWS	SN	Year	DOY	SWS
1	1996	13	MC	53	2000	22	MC	105	2004	287	SI
2	1996	56	SI	54	2000	43	MC	106	2004	304	SI
3	1996	63	MC	55	2000	52	MC	107	2005	2	SI
4	1996	100	MC	56	2000	145	MC	108	2005	29	SI
5	1996	185	MC	57	2000	154	SI	109	2005	49	MC
6	1996	242	SI	58	2000	178	MC	110	2005	64	SI
7	1996	319	SI	59	2000	193	MC	111	2005	95	SI
8	1996	360	MC	60	2000	279	SI	112	2005	110	SI
9	1997	10	MC	61	2000	288	MC	113	2005	119	MC
10	1997	36	SI	62	2000	303	MC	114	2005	128	SI
11	1997	42	MC	63	2000	319	SI	115	2005	140	SI
12	1997	66	SI	64	2000	360	SI	116	2005	174	SI
13	1997	87	SI	65	2001	21	SI	117	2005	269	SI
14	1997	111	MC	66	2001	24	MC	118	2005	281	SI
15	1997	121	SI	67	2001	87	MC	119	2005	306	MC
16	1997	135	MC	68	2001	212	SI	120	2005	317	MC
17	1997	159	MC	69	2001	217	SI	121	2005	361	SI
18	1997	188	SI	70	2001	254	SI	122	2006	16	MC
19	1997	240	MC	71	2001	281	SI	123	2006	26	SI
20	1997	246	MC	72	2001	305	SI	124	2006	37	MC
21	1997	274	MC	73	2002	59	MC	125	2006	65	MC
22	1997	318	SI	74	2002	89	SI	126	2006	95	SI
23	1997	326	MC	75	2002	103	MC	127	2006	124	SI
24	1997	364	MC	76	2002	131	SI	128	2006	219	SI
25	1998	8	MC	77	2002	159	SI	129	2006	231	MC
26	1998	16	SI	78	2002	247	SI	130	2006	239	MC
27	1998	48	MC	79	2002	277	MC	131	2006	260	SI
28	1998	59	SI	80	2002	300	SI	132	2006	267	SI
29	1998	63	MC	81	2002	322	MC	133	2006	293	MC
30	1998	80	SI	82	2002	325	SI	134	2006	301	SI
31	1998	101	MC	83	2002	341	SI	135	2006	314	SI
32	1998	122	MC	84	2002	360	SI	136	2007	15	MC
33	1998	157	SI	85	2003	3	SI	137	2007	29	SI
34	1998	186	MC	86	2003	8	MC	138	2007	59	SI
35	1998	218	MC	87	2003	29	SI	139	2007	82	SI
36	1998	239	MC	88	2003	58	MC	140	2007	91	SI
37	1998	268	MC	89	2003	88	MC	141	2007	127	SI
38	1998	280	SI	90	2003	92	SI	142	2007	237	SI
39	1998	292	MC	91	2003	192	SI	143	2007	263	SI
40	1998	317	MC	92	2003	207	SI	144	2007	292	SI
41	1998	357	SI	93	2003	230	MC	145	2007	324	SI
42	1998	363	MC	94	2003	233	SI				
43	1999	4	SI	95	2003	260	SI				
44	1999	13	MC	96	2003	287	SI				
45	1999	49	MC	97	2003	324	MC				
46	1999	55	SI	98	2004	22	SI				
47	1999	107	MC	99	2004	42	SI				
48	1999	211	MC	100	2004	69	MC				
49	1999	265	MC	101	2004	96	SI				
50	1999	298	MC	102	2004	199	SI				
51	1999	311	SI	103	2004	220	MC				
52	1999	337	SI	104	2004	243	SI				

3.3 Summary

LANL satellites are located at GEO. Outer electron radiation belt dropouts are spotted and measured using the multisatellite LANL summary plots and data sets. The selected dropouts are cleaned of solar proton contamination by checking the NOAA space environment for each event. Further restrictions were imposed that discard double events, and those with unclear signature of SIs and MCs by correlating the solar wind conditions provided in OMNI data base at the time of each event. Also, the OMNI data provide synchronised measurements of solar wind and geophysical parameters. Riometers detect ionospheric disturbance in form of absorption intensity. This absorption is directly proportional to particle being precipitated into the ionosphere. The chain of Finish riometers is used to investigate any significant correlation of dropouts and state of ionosphere. In order to reveal clear and consistent responses of these observations over a decade, SEA techniques were considered suitable to average out all the noisy signals in the data.

Chapter 4

Validation of Techniques

In order to validate the technique and methodology discussed in Section 3.2.2, this study first examined the 67 SI events identified by Morley *et al.* [2010b]. Two of the events not associated with dropouts were rejected while one is found to be contaminated by SPE. Thus, the 64 events used to study and validate the proposed methodology were a subset of Morley's events. For all acquired data, the reference time of the SEA is set to SI onset. The data extracted at this reference time were averaged and for robustness, the lower and upper quartiles were used to show dispersion of data. It should be noted however that, Morley *et al.* [2010b] used Global Positioning System (GPS) ordered by L^* in their statistical study of outer electron dropouts. This study focused on analysis of geosynchronous plasma environment at 6.6 R_E thus, did not use GPS observation. Also, accessibility to GPS data is not available at the time of this study. It should also be noted that Morley *et al.* [2010b] used hourly resolution OMNI data and three hourly average riometer data in each of the spatial bin. Their argument is that the Earth rotates by $15°$ every hour thus, the use of three hourly average riometer data is justifiable. In this study, three hourly data is used for the SEA. This resolution of time helps to correlate with the three hourly sourced quasi-logarithmic index, Kp. Another substantial reason which could account for the disparity to Morley *et al.* [2010b] observation is that their events were inclusive of some SI events not associated with dropouts. Also, Moreley's events were not completely devoid of Solar Proton Events (SEP) which had been filtered in the course of these study.

4.1   SIs: Geophysical Observations

The SEA of the various geophysical parameters is performed for the 64 subset of SI events initially identified by Morley *et al.* [2010b] as presented in Figure 4.1.

In Figure 4.1 (first panel), superposed average of Kp as a measure of magnetospheric convection is seen to be ramping up 3 hours prior the arrival and reaches peak of 3+ at approximately 3 hours after the arrival of SIs and then returns to the pre-event level in 0.5 day.

Figure 4.1 (second panel) displays Dst index. It shows positive value of about 15 nT prior to the arrival of SI indicating weakly magnetospheric pressure and reverses to an average of -30 nT at SI arrival. Dst perturbation continues through a day although at relatively low level as can be seen. Small Dst perturbation is clearly organized by the solar wind stream interfaces in the manner expected based on the variations of solar wind variables during high speed stream interface for example, [Borovsky and Denton, 2006, 2009; Morley *et al.*, 2010b].

In Figure 4.1 (third panel), is the B_z component which prior to the arrival of SI, was distinctly in northward peak of 10 nT and gradual southward reversal prior to the arrival of SI. The threshold value of GSM-B_z of less than -10 nT persists for about 3 hours at SI arrival. An important characteristic of B_z in GSM coordinates from this analysis is a persistent negative bias in the average value that lasts for at least three days. It is known that when this component is negative the IMF merges with the Earth's magnetic field and drives magnetic activity. Although not demonstrated here this bias is a consequence of the Russell-McPherron effect [see Russell and McPherron, 1973] which drives magnetospheric activities. High-speed-stream-driven storms are owed to a Russell-McPherron effect of a Parker-spiral-orientation

of the magnetic field seen in GSM coordinates: southward B_z after the sector reversal creates the storm and northward Bz prior to the sector reversal creates a "calm before the storm" [Borovsky and Denton, 2009]. It is apparent that some days before the SI the selected events were geo-ineffective, that is, $B_z > 0$. However, the Earth passed through the heliospheric current sheet hours before the SI reversing the polarity of the IMF so that the IMF was geo-effective persisting during the high-speed stream interface.

Figure 4.1 (fourth panel), shows the solar wind number density with the sharp peak at the arrival of SI reaching approximately 19 cm^{-3} indicating difference of dynamic-pressure as fast wind overtakes slow wind.

The solar wind radial velocity (GSE -V_x) is presented in Figure 4.1 (fifth panel) showing greater than 300 km/s before SI arrival. Just at SI onset, -Vx is elevated to range of greater than 500 km/s for 3 days after SI implying that high-speed- stream driven storms last for over 3 days. Prior to the SI arrival is compressed slow wind stream and after the SI is compressed fast wind stream while at the interface is shear velocity.

In Figure 4.1 (sixth panel) the GSE y-component (solar wind azimuthal velocity) is shown. Close to the day 0, V_y is at the level of around -9 km/sec on average but reverses to approximately +10 km/s on average scale indicating arrival of SI at Earth. Compared with Figure 1 in Morley work (not shown), the general overview of these parameters did not show any significant difference.
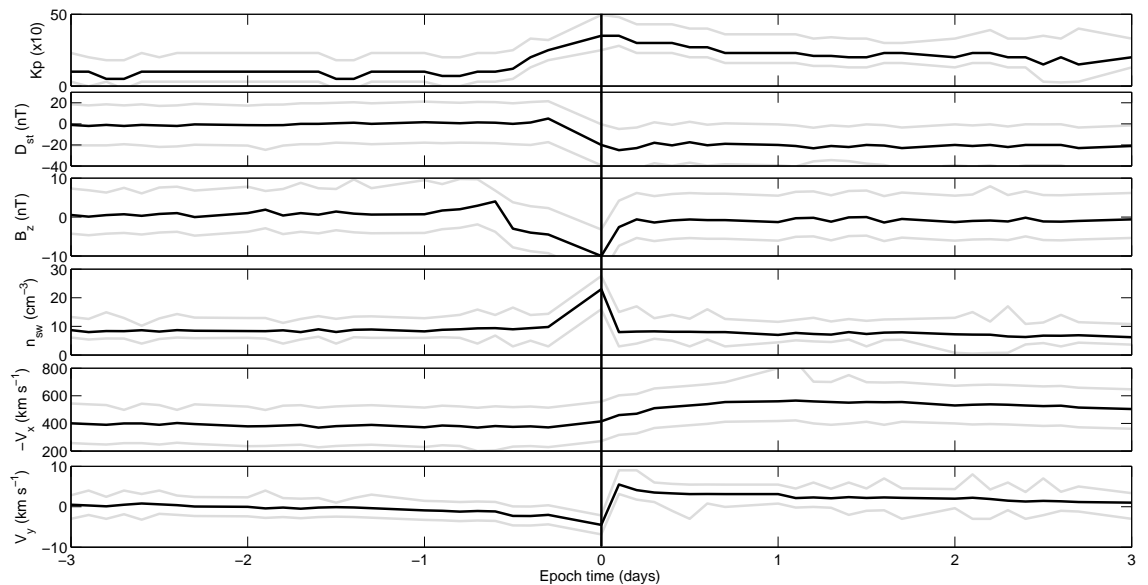
Figure 4.1: Plots of superposed properties of 64 SIs used: in each panel the grey lines are the third and first quartiles while black line indicates the average, with the zero epoch taken as the time of V_y reversal indicated by vertical line. From top is Kp index, Dst index, IMF B_z, solar wind number density, solar wind V_x and solar wind V_y.

4.2 Equatorial Observation of Electron Flux Dropout

For every operational LANL satellite, flux data were normalised to obtained the same yearly averaged logarithm [Belian et al., 1992]. Observations at GEO can also be compared with global positioning system (GPS) taken at $L^* = 6$ when considering adiabatic effects since particles would move outward to conserve their third adiabatic invariant during disturbed time. It will be reasonable to say there is less mixing of adiabatic effects in this analysis since the sets of SIs used here do not follow strong enhancement in ring current.

Figure 4.2 presents an overview of superposed average of the logarithm of 225–315 keV, 315–500 keV and 0.75–1.1 Mev electron flux as measured by LANL satellites. In Figure 4.2 (top), electrons of 225–315 keV is plotted showing gradual dropout of electron flux from -1 (day) and reaching minimum at approximately 3 hours after the arrival of SI and recovers quickly to pre-event level in less than a day. In Figure 4.2 (middle) is the 315–500 keV electron flux and as can be seen there is also a gradual dropout prior to the arrival of SI but electron flux dropout is about 0.78 order deeper than in 225–315 keV channel at arrival of SI. The recovery is seen to be slightly higher than the pre-event level for more than three days. Figure 4.2 (bottom) shows 0.75–1.1 Mev electrons, there is also observed gradual dropout from -0.5 day till 0.8 day after the arrival of SI. The dropout is seen to be about 1.55 and 0.11 order differ from 225–315 keV and 315–500 keV channel respectively while the recovery level is higher than pre-event level more than 3 days. Bearing in mind the time resolution employed in this SEA, the recovery period is roughly the same with the dropouts presented by [Morley *et al.*, 2010b]. However, the minor disparity could perhaps be due to GPS orbital peculiarities. It should also be noted that some of the Morley's events were discarded as earlier mentioned in this chapter.
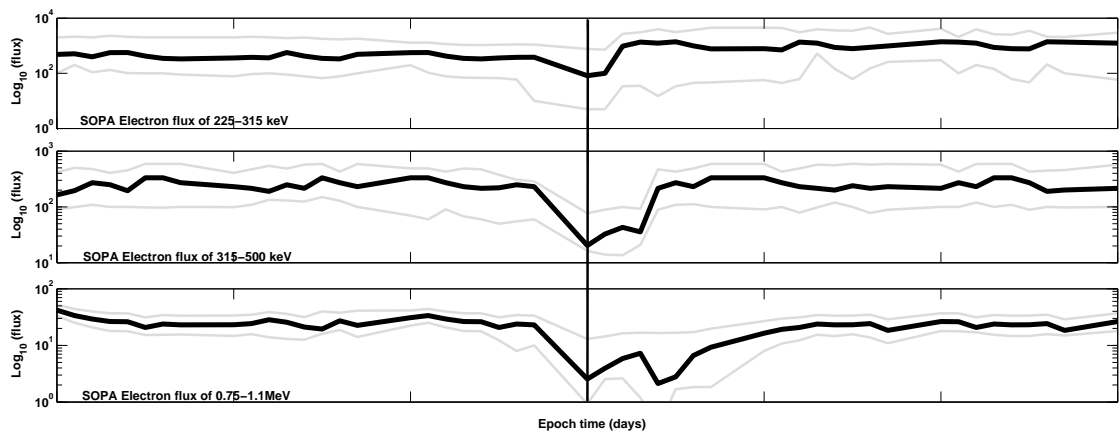
Figure 4.2: Superposed epoch plots of electron flux as measured by combined LANL satellites: (top) is 225–315 keV, (middle) is 315–500 keV, (bottom) is 0.75–1.1 MeV. The vertical line indicates arrival of SI. Format is as in Figure 4.1.

4.3 Estimate of > 30 keV Electron from LEO

Figure 4.3 presents the superposed counts per second of the precipitating > 30 keV electrons. Prior to the arrival of SI, the level of count is very low. At the SI onset the count increases significantly only around $5.05 < L < 6.05$. region. After about a day, the count recovers to pre event level. With different SEA reference, Meredith *et al.* [2011] also investigated related High Speed Solar wind (HSS) driven events. However, the scenario in count rate as presented in Figure 4.3 is roughly similar to that of Meredith *et al.* [2011] as presented in their Figure 1 (b) (not shown). According to Meredith *et al.* [2011], the electron count rate stays constant in the days before the storm onset, increases dramatically at storm onset and decreases at about 0.5 days after. There is also dramatic peak in precipitating flux at the onset of the event reported by Meredith *et al.* [2011] Figure 2 (h) (not shown). The characteristics of the counts in the Figure 4.3 is clearly seen in the line plot shown in Figure 4.4.

For clarity purposes, superposed averages of > 30 keV electrons at 0° (90°) that is, precipitating (trapped) channels across three spatial cuts (L= 4.02, 5.02 and 6.02) using POES15 and 17 (2030-0630 MLT) and POES 16 and 18 (0730-1930 MLT) were presented as line plots in Figure 4.4 (top-bottom). In Figure 4.4 (top), electrons at $L = 4.02$ is plotted, as can be seen there is a gap of more than factor of 5 difference between trapped and precipitating electrons preceding and few hours following the arrival
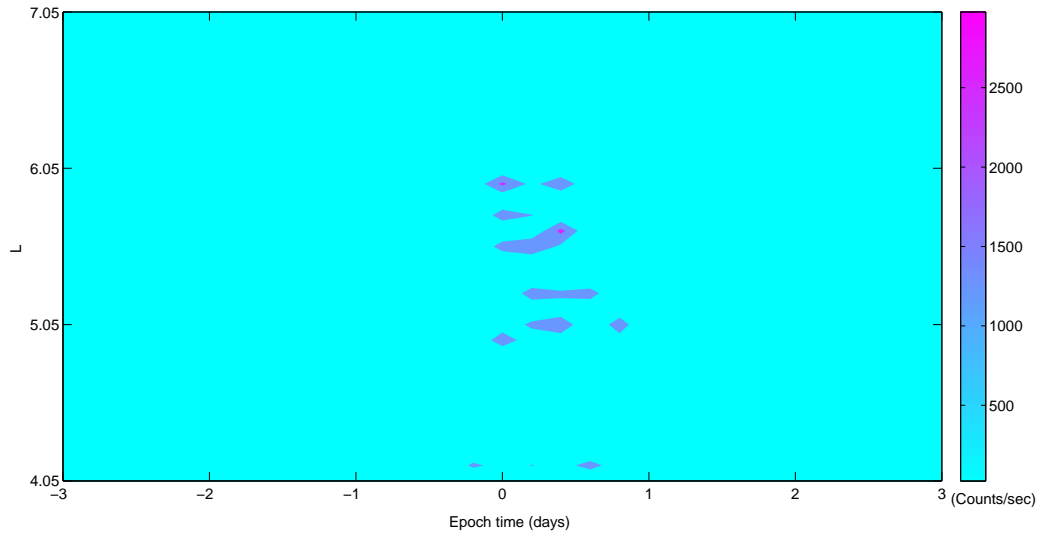
Figure 4.3: Superposed L–t diagram of precipitating > 30 keV electron counts as observed by NOAA/POES satellite for 64 SI events. The color code reflects average values of the electron counts.

of SI which indicates no substantial precipitation at the absence of the event. The narrow peak is seen on arrival of SI. Figure 4.4 (middle) is the plot of > 30 KeV electrons at $L = 5.02$ with more than a factor of 5 gap between trapped and precipitating electrons preceding and a day following the SI. This implies busty precipitation at this region. The peak with slower decaying character is observed in both trapped and precipitating electrons at the SI arrival. Figure 4.4 (bottom) shows > 30 keV electron at $L = 6.02$ both trapped and precipitating electron showing systematic variation. Precipitating electron as can also be seen peaks on SI arrival. Similar to $L = 5.02$, the simultaneous slower decaying peak of both trapped and precipitating electrons are seen in the morning sector which began approximately 0800 MLT to around 1400 MLT. The slower decaying peak lasted for about 6 hours after the impact of SI.
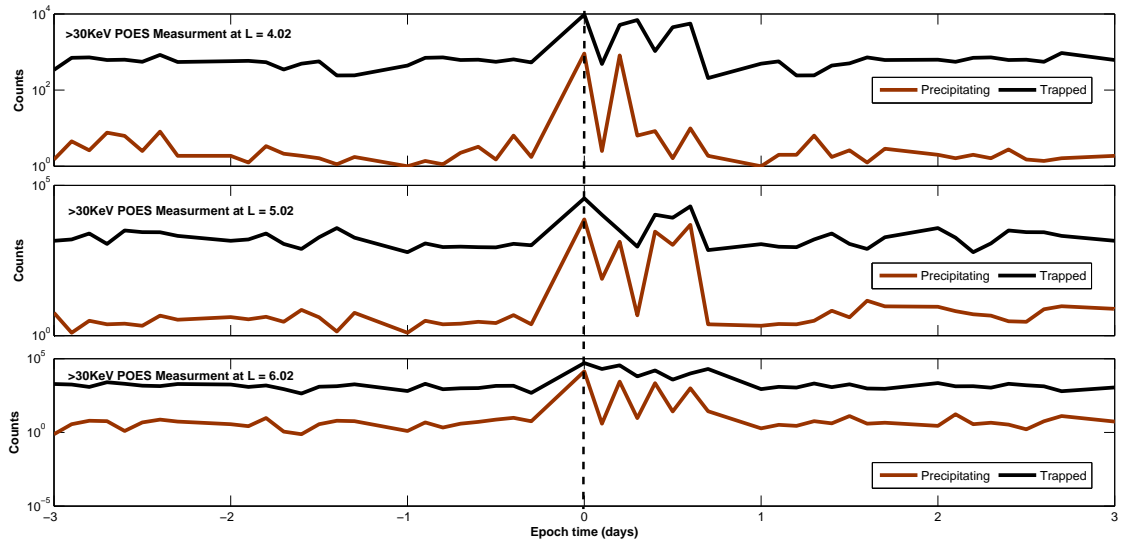
Figure 4.4: Superposed epoch plot of trapped and precipitating > 30 keV electron from NOAA/POES satellite. The black line in each plot indicates measurements from $90°$ telescope (trapped electrons) while the red line indicates measurements from $0°$ telescope (precipitating electrons). The dash vertical line indicates arrival of SI (top) is the >30 KeV at $L = 4.02$, (middle) is $L = 5.02$ while (bottom) is counts at $L = 6.02$.

4.4 Discussion

SEA shows that these sets of events occurred during southward B_z. This confirms the immersion of the magnetosphere in slow solar wind [Morley *et al.*, 2010b] during the events. Moderate magnetospheric activity is seen but SI does not follow strong ring current measurement on arrival. It is also noticeable that difference in dynamic-pressure causes sharp peak in solar wind number density during which magnetopause would have moved inward on arrival of SI while compressed fast wind lasts for 3 days after SI.

Across GEO, there is tendency for outer electron radiation belt dropouts prior to the arrival of SI which reaches deepest minimum mostly at 3 hours after the arrival of SI. The recovery is also seen to be rapid at lower energies. It is very important to note that prior to the arrival of the SI magnetic activity is very low and electrons accelerated previously are gradually lost from the radiation belts. About half a day before the arrival of SI the IMF B_z begins to reverse southward while at the synchronous orbit relativistic electron fluxes begin to decrease more rapidly. This analysis corresponds to the Global Positioning System (GPS) observation reported by Morley *et al.* [2010b], who found dropout to be energy and L* dependent with combined radial diffusion and lost through magnetopause as the likely cause. Although in this study, the GEO observation is similar to that of $L^* = 4$–4.5. This of course is reasonable as particle usually move outward to conserve their third adiabatic invariant in response to changes in B_z. For example, satellites during storm periods can be at $L = 4$ but measuring particles from $L = 3$ due to enhanced ring current at that period [Varotsou *et al.*, 2008]. At such time, the L^* of the satellite is equal to 3.

POES 15-18 orbiting LEO shows that > 30 keV precipitating electron flux level is about a factor of 5 lower than trapped flux preceding and about a day following the time of the event. Consistent with some previous observations, [e.g Clilverd *et al.*, 2010a; Lam *et al.*, 2010], there is tendency in precipitation following the trend of trapped flux. Here, statistical analysis revealed an unstructured abrupt peak (with slower decaying character) in precipitating electron flux on arrival of SI which coincided with time of deepest minimum of observed dropouts. The local asymmetry of magnetic field could probably lead to openings of the closed drift path through which energetic particles can get lost and precipitate into the ionosphere but cannot be directly attributed to the cause of the observed outer electron dropout. Analysis also reveals high geomagnetic latitude to be of higher precipitation of electron flux consistent

with Morley *et al.* [2010b]. This is a good indication of chorus driven microburst as one of the important loss mechanism operating during this period and it is therefore arguable that if the peak of ULF wave power is examined it will not confirm this possibility. Although combined riometer data were used in Morleys' work which indicate continuous ionospheric absorption for about 12 hours after the impact. The singular difference in Morley *et al.* [2010b] and this observation could be attributed to riometer indiscriminate sensitivity to mixed particle population and combining riometers of different L values could be somewhat tricky. POES electron telescope's sensitivity to protons cannot also be left unemphasised although some cleaning procedures were taken as earlier mentioned yet the dominant loss mechanism is still not completely understood.

Chapter 5

Case Studies: SI-Driven Dropouts

Since the storm driver is such a critical part of the radiation belt research, a more complete understanding of outer electron radiation belt dynamics requires event based studies that utilize the actual response to storm driver. Although SEA represent the majority of signal responses but for in-depth analysis, some individual events were selected. The SI- driven dropouts of 23 June 2005, 7 May 2007 and 11 November 2007 are used for detailed studies. It should also be noted that these three events are subset of the present selected events shown in Table 3.1.

5.1 Case Study 1: SI-Driven Dropout of 20 November 2007

A case of SI- driven dropout on 20 November 2007 is presented. Various geophysical properties, electron flux measurements and the state of ionospheric absorption were studied.

5.1.1 Geophysical Parameters and Solar Wind Conditions

Figures 5.1 (a-h) present the geophysical parameters during the SI driven dropout of 20 November 2007. Figure 5.1 (a) is the plot of Kp index. Kp is seen ramping up prior to the event reaching approximately 5+ on arrival of SI. Kp remain higher than the pre-event level after the arrival for over a day. The higher magnetospheric activity observed on arrival of SI is not unexpected in some cases of high speed stream driver [e.g Borovsky and Denton, 2009]. The other storm measure is by Dst indices as presented in Figure 5.1 (b). Prior to the arrival, there is positive value of around 1.1 nT indicating calm before the storm. On arrival a small storm of about -50 nT is measured by Dst which lasted for a day.

Around the time of these storm measurements, the IMF B_z is studied, as shown in Figure 5.1 (c). Prior to the storm B_z was at +8 nT and reverses southward on arrival to about -10 nT and remains southward for over a day after the arrival. This observation indicate geoeffectiveness of IMF during the stream interface.

Centered around the geoineffective and effective, the level of solar wind proton density is checked as shown in Figure 5.1 (d). Solar wind proton density is at the peak of about 10 cm^{-3} on arrival of SI. After the high density is compressed fast wind while prior is the compressed slow wind and at the onset of the SI is shear velocity in between the compressed slow and fast solar wind.

During the compressed slow and fast wind and at shear velocity, the solar wind radial velocity (-V_x GSE) is examined as presented in Figure 5.1 (e). Prior to the SI occurence, -V_x is steady at approximately 400 km/s while it ramped up on arrival of SI.

Another solar wind condition around this storm activity is shown in Figure 5.1 (f) which presents the Alfvén Mach number (M_A). The Alfvén Mach number is at approximately 6.0 on arrival of SI with slight increase after the arrival of SI. Such high M_A is perhaps due to the increased in pressure as fast solar wind overtakes the slow solar wind.

An idea of the state of magnetopause is needed during these activites. Therefore, the solar wind pressure is examined at the time of this event as presented in Figure 5.1 (g). Relative to prior the arrival, a peak of about 5 nPa is observed on arrival of SI. This peak is an indication that magnetopause would have moved inward on arrival of the SI. The increase in pressure due to shear velocity at interface is also observed. However, this event cannot account for the peak observed during the geoineffective period that occurred a day prior to the event.

Since the magnetopause is inward as partly explained by the peak seen in dynamic pressure on arrival, the change in orientation of azimuthal velocity (V_y) is apparent presented in Figure 5.1 (h). V_y deflects from -6.0 km/s to about +7.0 km/s on arrival of SI. The deflection of V_y from west to east implies arrival of SI at Earth. Throughout this study, the onset of SI is taken as the time of V_y deflection.
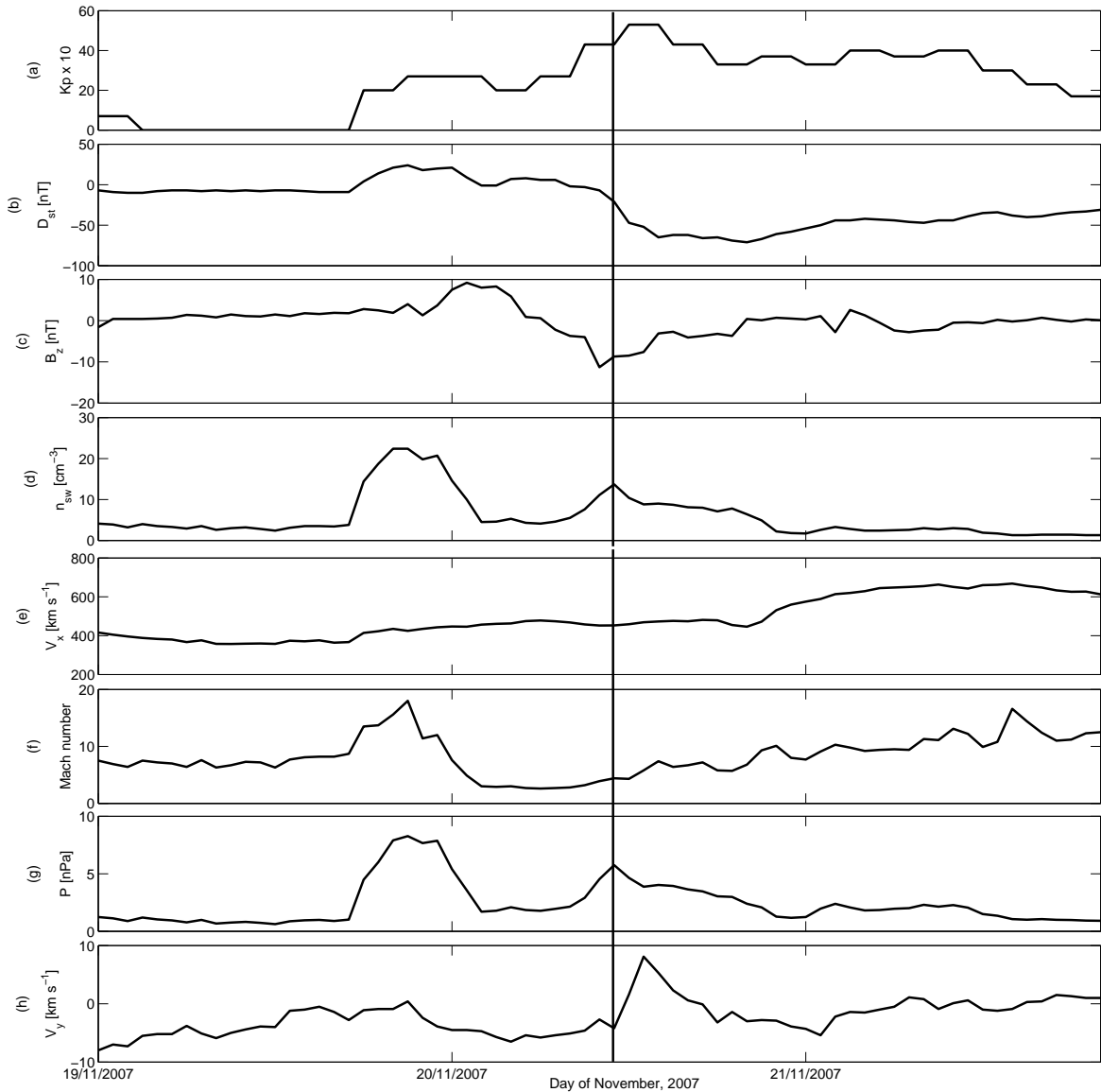

Figure 5.1: Geophysical parameters and solar wind conditions on 20 November 2007 SI-driven dropouts. From (a) - (h) are Kp index, Dst index, Z-component (GSM) of the solar wind magnetic field, Solar wind number density , solar wind radial velocity, Alfvén Mach Number, solar wind pressure and the solar wind azimuthal (west-east) flow velocity. The vertical line indicates the onset of SI.

5.1.2   LANL/SOPA Measurements of Electron Dropout

In Figure 5.2 (top) is the plot from the LANL-01A satellite on 20 November 2007. The dropout also occurs across the considered energy bands. Substorm-like activity was initially observed in the night side prior to the arrival of the SI. There is also substantial drop of electron flux observed in dusk at around 1700 LT on SI arrival with order of 10^{-2} flux deeper. The onset of the recovery is higher than the pre-event level and energy dependent. Similarly, in Figure 5.2 (middle), measurements from LANL 97A satellite on 20 November 2007 are shown. Tendency for dropouts is also first observed close to the arrival of SI in dusk sector and also seen when it was at night side on arrival of SI around 1900 LT. The order of electron dropout observed is about 10^{-2} flux deeper after the arrival of SI. At the recovery phase, electron fluxes with lower energy recovers quickly and were above the pre-event level. Another LANL satellite, 1994-084, is examined as presented in Figure 5.2 (bottom). It first observed dropout at midnight. Electron flux is observed to reach minimum of 10^{-1} deeper during the dropout. The onset of recovery is higher than the pre-event level. There is quick recovery at lower energy while there is a delay in quick recovery at higher electron flux energy. Throughout the observation presented in Figure 5.2, the time delays in minimum flux at higher energy with respect to lower energy band is apparent.

This observation can most probably arise through inward diffusion from the plasmasheet, or may represent the increased population of ring current electrons via increased magnetospheric convection, or through another phenomenon known to be the action of magnetospheric substorms. It is also clear that at the peak in dynamic pressure at time of event can be correlated with the magnetopause inward movement. That is, the magnetopause would have moved closer to the Earth implying possible lost through magnetopause shadowing.

5.1.3   Riometer Absorption

Figure 5.3 (a-h) presents the ionospheric observation from the chain of Finish riometers on 20 November 2007. During this period, data was unavailable at Hornsund ($L = 13.2$), Iris (L= 6.0), Rovanlemi ($L = 4.9$) and Jyväskylä ($L = 3.7$). But in Figure 5.3 (c) is the plot of absorption from Abisko riometer ($L = 5.7$) which is at the peak of about 1.2 dB on arrival of SI.

A Narrow peak in absorption is also seen in Figure 5.3 (d) from Ivalo riometer ($L = 5.6$) reaching 4.2 dB on arrival of SI and return to pre-event level afterwards.

At Sodankylä riometer ($L = 5.2$), there is no noticeable absorption on arrival and after SI as shown in Figure 5.3 (e).

Oulu riometer ($L = 4.4$) in Figure 5.3 (g) shows no significant absorption on arrival of SI. The peaks later seen at around 4 hours after the arrival cannot be directly attributed to SI. It could probably be due to effect of other interplanetary shock.

Riometers, in general, respond to changes in ionospheric free electron density at heights where the electron motion is collision dominated. During this event, collision is apparently seen to be outside plasmapause at the region close to the equator. However, the significant peak at the polar latitudes ($L = 5.7$ and $L = 5.6$) is not seen exceed an hour and there is a quick return to pre-event levels. The peaks observed at these latitudes a day after the event could be due to varying processes acting at the same time which cannot be fully explained by the arrival of SI.
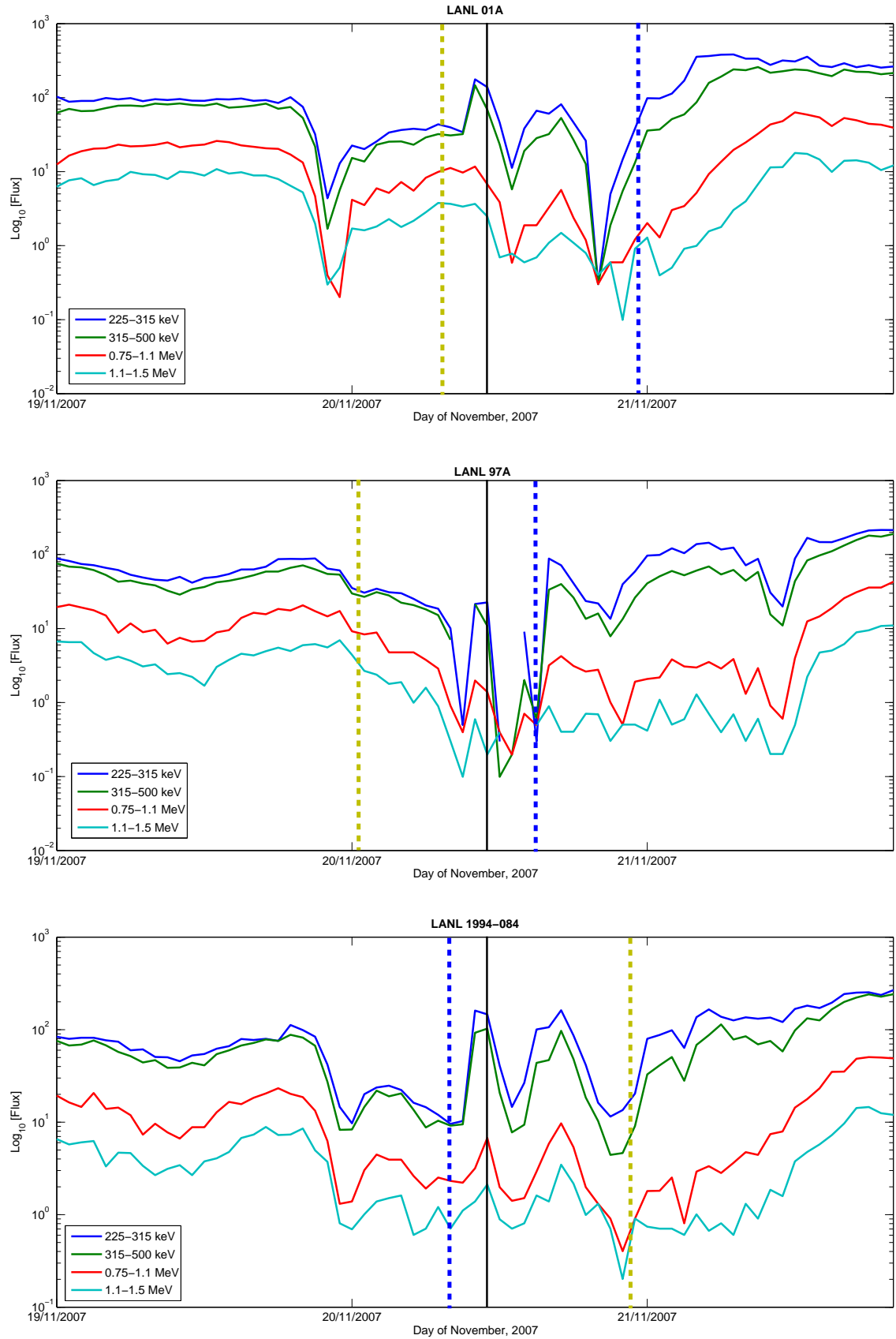
Figure 5.2: Electron flux as measured by the LANL 01A, 97A and 1994–084 satellites during SI-driven dropout of 20 November 2007. From top to bottom, each of the three panels contains 225–315 keV (deep blue), 315-500 keV (green), 0.75–1.1 MeV (red) and 1.1–1.5 MeV (light blue). The black vertical line indicates the arrival of SI while the yellow dash-line indicates local noon and blue dash-line indicates local midnight.
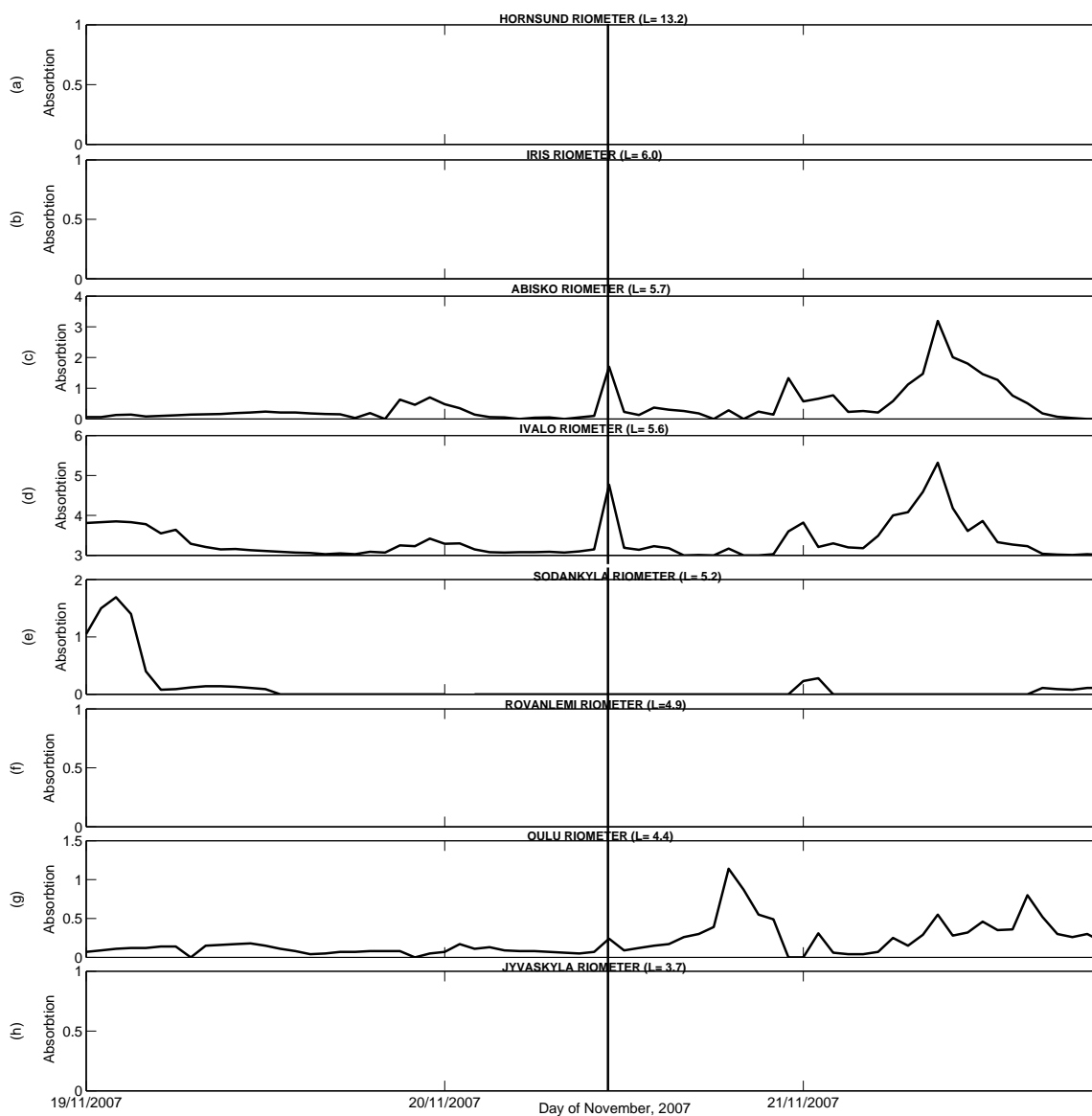
Figure 5.3: Riometers absorption during SI- driven dropout of 20 November 2007. The vertical line indicates the onset of SI arrival.

5.2 Case Study 2: SI-Driven Dropout of 7 May 2007

The geophysical properties, flux level and absorption during SI-driven dropout of 7 May 2007 were also studied. This event was earlier reported by Morley *et al.* [2010a] as rapid and global ever observed using global positioning system (GPS) satellites. The interest of this study in this event is to examine the GEO electron flux variation and the ionospheric absorption.

5.2.1 Geophysical Parameters and Solar wind Conditions

In Figure 5.4 (a-h) the geophysical parameters during SI-driven dropout of May 7 2007 are presented. Similar to Figure 5.1, storm activities were relatively prior to the arrival of SI. Similarly, there is a peak in solar wind dynamic pressure on the arrival which again indicate magnetopause closer to the Earth. However, the snap back of IMF Bz from southward to northward and then back to southward which occurred 2 hours after the arrival has an effect on the overall dynamics after the SI.

Figure 5.4: Geophysical parameters and solar wind conditions on 7 May 2007 SI-driven dropouts. Format is as in Figure 5.1.

5.2.2 LANL/SOPA Measurements of Electron Dropout

Similar to the event earlier presented in Figure 5.2 there is also tendency for energy dependent dropouts at all energy bands across various LT as presented in Figure 5.5 (top-bottom). However, there is less substorm activity except prior to the SI as noted from LANL 1994-084. Therefore, the possibility for the cause of dropout as earlier noted partly holds. It can be said that there is minimum action of the magnetospheric substorms compared to the previous event shown in Figure 5.2.

5.2.3 Riometer Absorption

Figure 5.6 further presents the ionospheric absorption on 7 May 2007 from the chain of Finish Riometers as earlier shown in Figure 5.3. Similarly, significant peaks are also observed within the polar regions (L= 5.7, 5.6 and 5.2). In contrast to previous case (Figure 5.3), Figure 5.6 continues to show peak on the arrival of SI at Sodankylä riometer ($L = 5.2$). This observation still confirmed the equatorial region to be collision dominated during SI arrival.
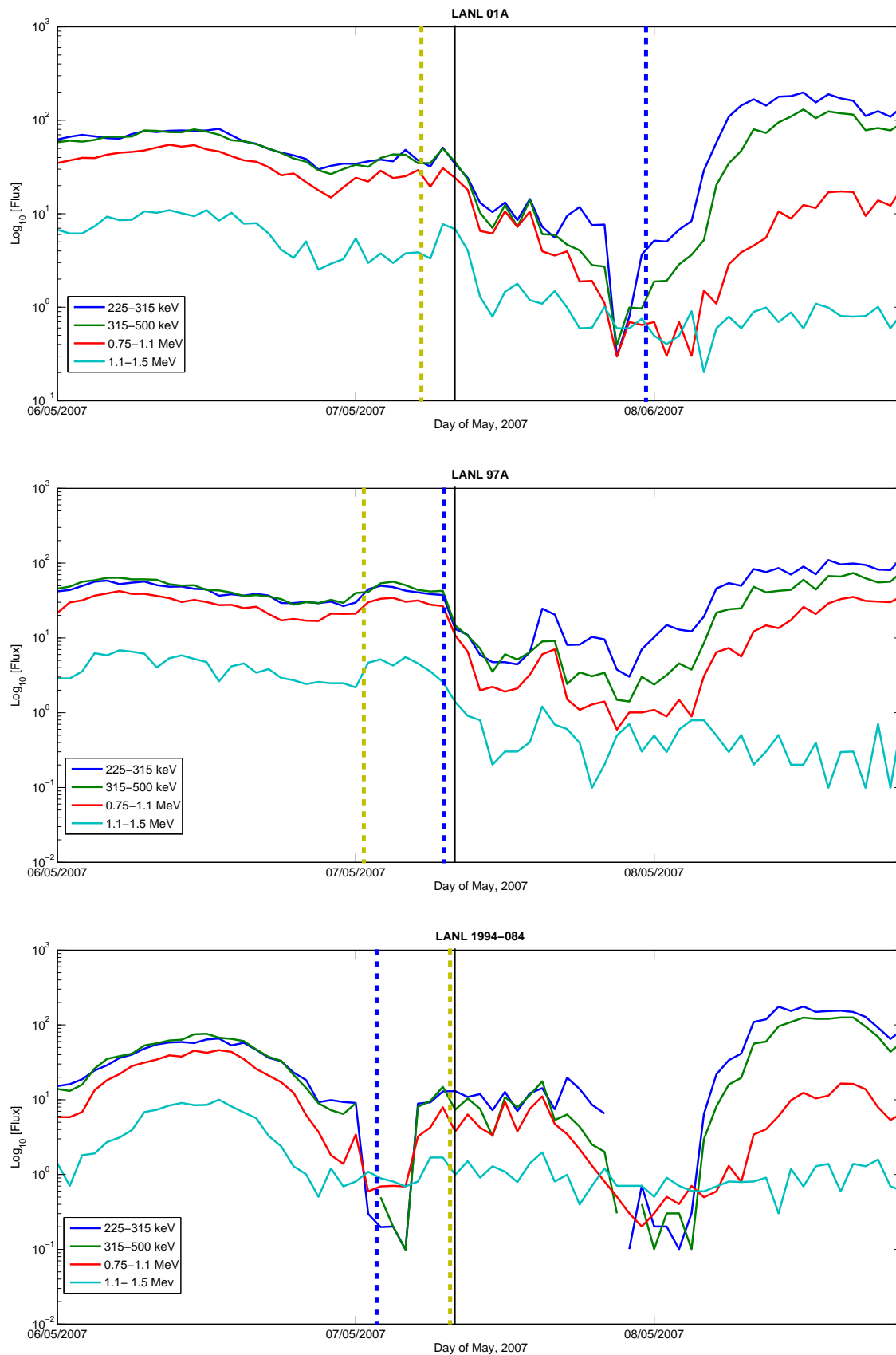
Figure 5.5: Electron Flux from LANL SOPA 01A, 97A, 1994-084 satellites During SI-Driven Dropout of 7 May 2007. Format is as in Figure 5.2.
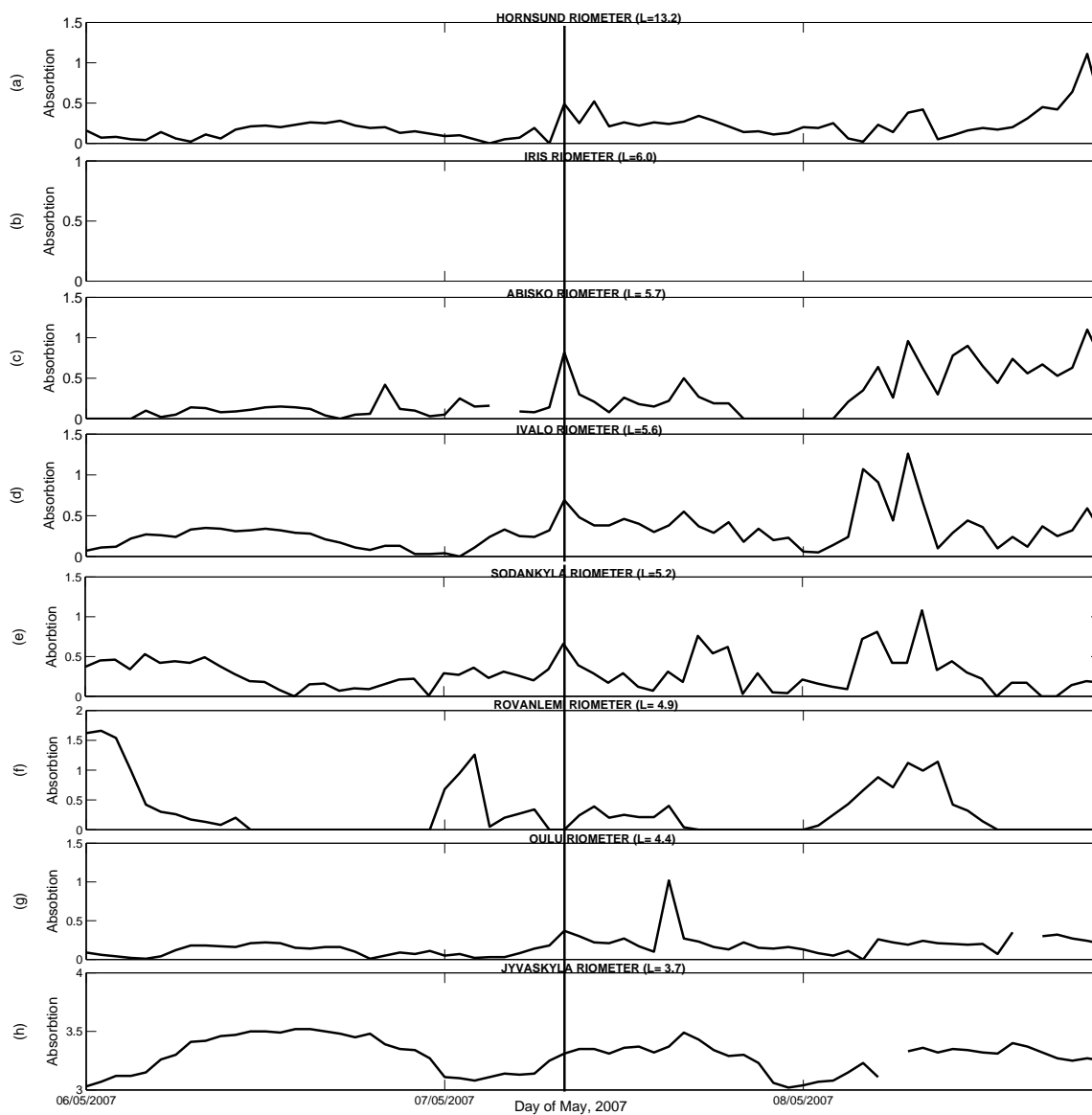
Figure 5.6: Riometers absorption during SI-driven dropout of 7 May 2007. Format is as in Figure 5.3.

5.3   Case Study 3: SI-Driven Dropout of 23 June 2005

On 23 June 2005, there were dropouts of electron across a wide range of energy bands and globally observed by SOPA satellites with slight differences in local time. Various geophysical parameters and solar wind conditions, GEO electron flux level and ionospheric absorption during this event were studied.

5.3.1   Geophysical Parameters and Solar Wind Conditions

Figure 5.7 (a-h) shows the geophysical parameters during the dropouts of 23 June 2005. Similar to Figure 5.1 and Figure 5.4, activities remain quiet prior to the arrival of the SI arrival. However, it is observed that a snap back of IMF B_z also occurred similar to 5.4 but without any significant changes on overall dynamics after the SI. Perhaps this implies that the local asymmetry of IMF B_z might be insufficient to explain the cause of the observed outer electron radiation belt dropouts during SI.
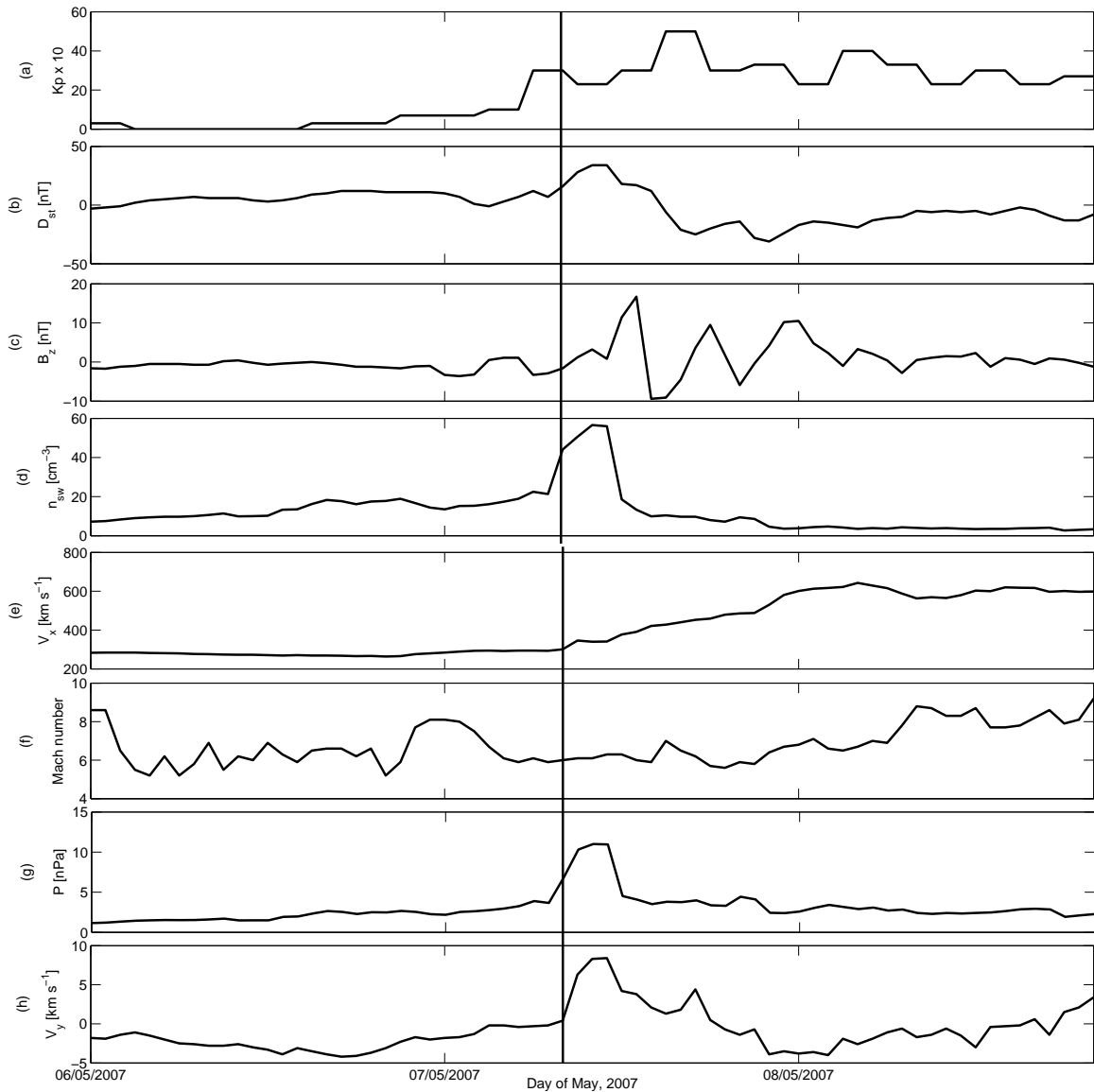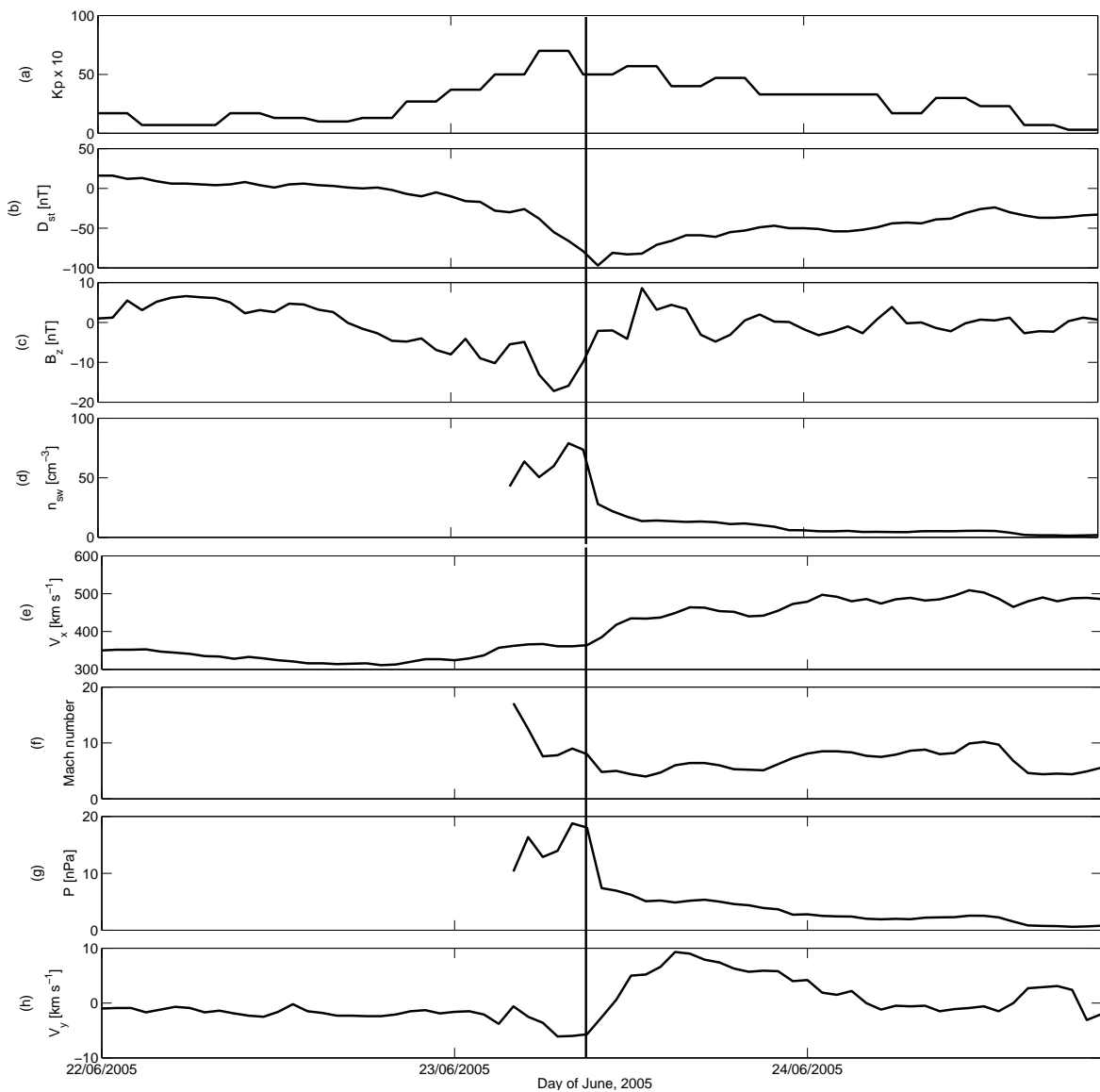

Figure 5.7: Geophysical parameters and solar wind conditions on 23 June 2005 SI-driven dropouts. Format is as in Figure 5.1.

5.3.2 LANL/SOPA Measurements of Electron Dropout

Figure 5.8 presents observation similar to that of Figure 5.2 and Figure 5.5. However, the substorm activity prior to the arrival of SI is more pronounced in this case in contrast to Figure 5.5 where substorm activity is less. Considering the geophysical parameters during this event, the plausible cause for this GEO electron observation can perhaps in whole be explained by the phenomena noted for Figure 5.2.

5.3.3 Riometer Absorption

Again, Figure 5.9 presents the ionospheric absorption of particle precipitation into the ionosphere using the chain of Finnish riometers. Contrary to Figure 5.3 and Figure 5.6 the peaks in absorption is seen at about 2 hours prior to the event. At this duration, there is also significant peak at Oulu riometer ($L = 4.4$). Notably, the peaks correspond to the time of substorms as depicted by LANL satellites. Although there is tendency for drop outs and subsequent recovery on arrival of SI yet the absorption peaks can not be directly associated with the dropout onset. The complicated solution towards identifying the major mechanism during this event is owed to varying processes acting simultaneously. Statistical approach will later be employed to study the general responses of SI dropouts. Perhaps by this approach, the dominant mechanism can be more visible.
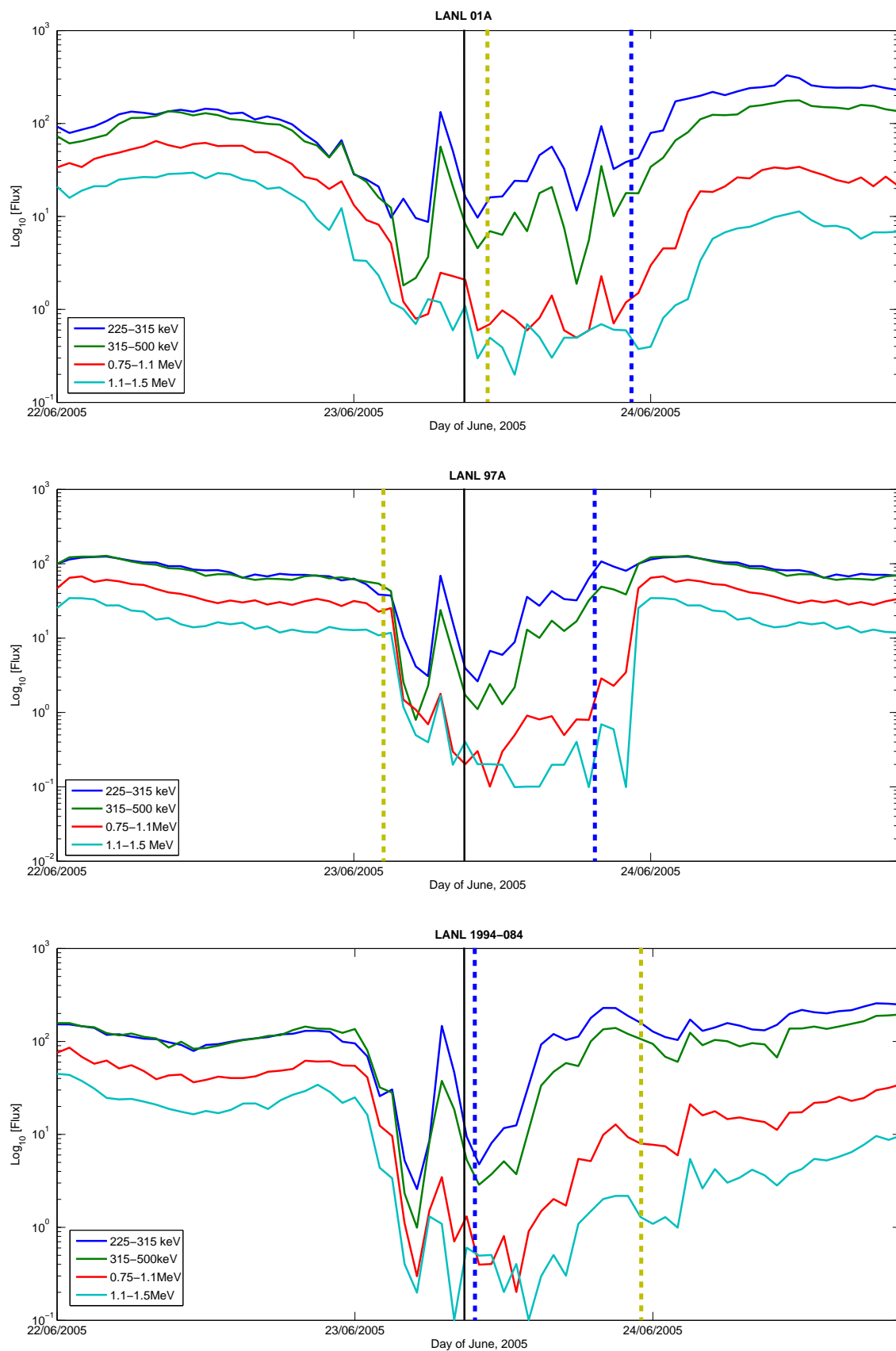
Figure 5.8: Electron Flux as measured by the LANL SOPA 01A, 97A, 1994-084 satellites during SI-driven dropouts of 23 June 2005. Format is as in Figure 5.2.
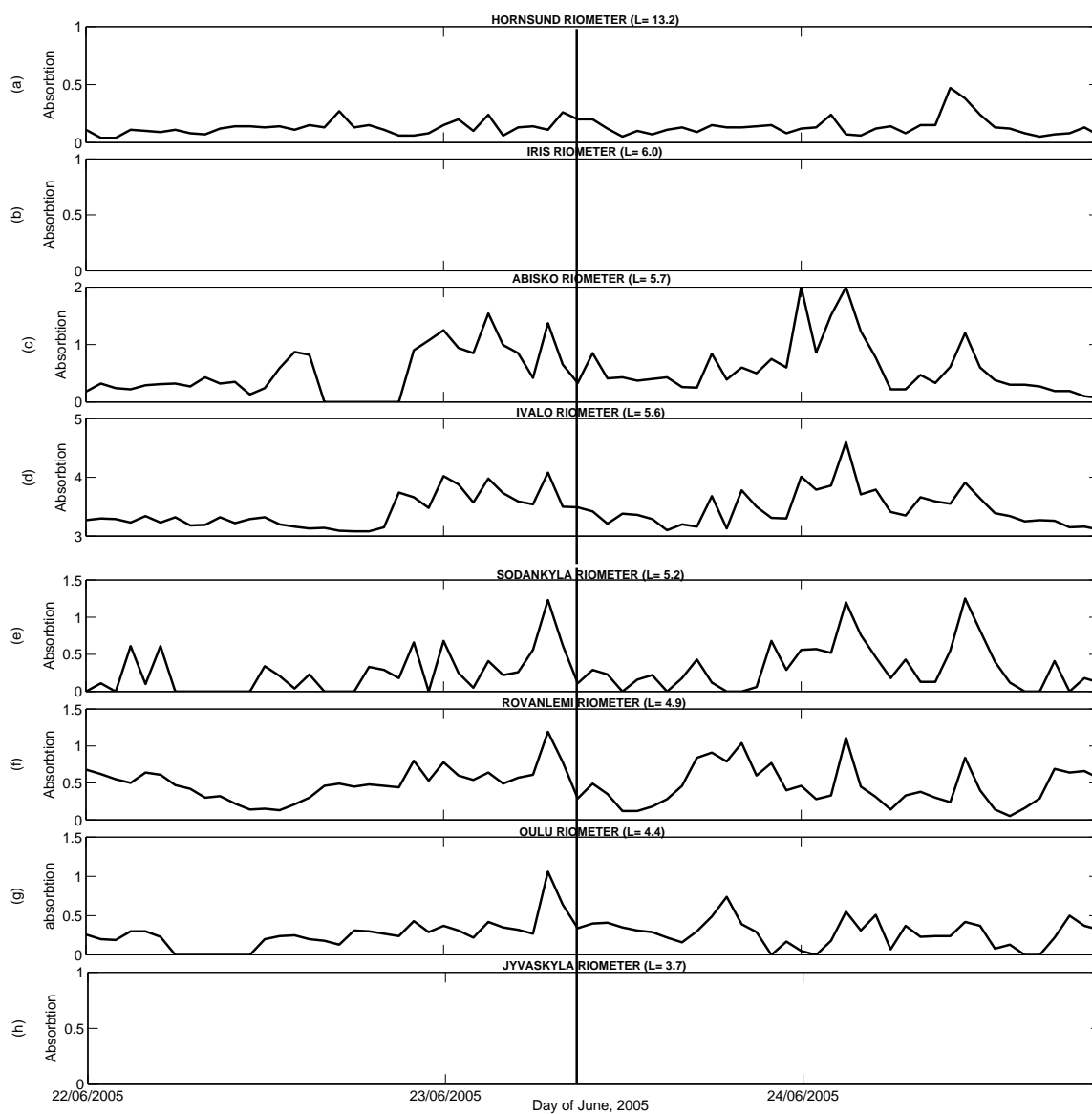
Figure 5.9: Finish chain of riometers absorption during SI-driven dropout of 23 June 2005. Format is as in Figure 5.3.

5.4   Summary

Case studies were presented for 20 November 2007, 7 May 2007 and 23 June 2005, SI-driven dropouts. For each of the parameters, the dropout and the onset of the recovery were analysed.

The tendency for dropout during these events began within the same active period of magnetospheric convection as measured by the Kp index. This differs from 23 June 2005 when the peak in Kp is higher prior the event. Electron flux dropouts were observed during southward turning of IMF B_z. During this time, the Dst indicates a small storm. However, on the recovery side of the dropout, there was not any significant changes in Kp and Dst. The onset of SI-driven dropout of outer electrons was seen to be simultaneous with the peak of solar wind number density as solar wind radial velocity ramped up while the recovery of the dropout was seen to be during drop in solar wind number density, and compressed fast wind. During these periods, Alfvén Mach number is typically high as well as the solar wind pressure with the onset of electron dropout without any noticeable change during the dropout recovery. The tendency for dropouts was seen during the reversal of azimuthal solar wind velocity from west to east and recovered after the arrival of SI.

At GEO, the electron flux of 225–315 keV, 315–500 keV, 0.75–1.1 MeV and 1.1–1.5 MeV were examined. The tendency for electron dropout was seen to be gradual and energy dependent and the recovery from dropout was faster at lower energy. The electron flux level immediately after recovery was mostly higher than the pre-event level. The dropout reached deepest minimum mostly at the arrival of SI. For all the cases, the dropout occurred at all local times; dawn, midnight, dusk and at noon which also holds for recovery. Inward radial diffusion, strengthening of the ring current electrons via enhanced magnetospheric convection, action of magnetospheric substorms as well as magnetopause shadowing were the plausible phenomena noted as the cause of this equatorial dropouts during SI.

The ionospheric absorption during these periods was investigated in order to know how electron dropout compared with precipitation. Two of these events, 7 May 2007 and 20 November 2007, showed significant mid-latitude absorption on arrival of SI which coincided with the minimum electron flux dropout. This indicate changes in ionospheric free electron density at this height on SI arrival. Morley *et al.* [2010b] also found link between dropout due to high speed stream interface and busty riometer absorption at mid-Latitude around the late morning sector. These were contrary to the absorption seen at some hours prior to the arrival of SI on 23 June 2005. It was actually noted that event of 23 June 2005 depicts peaks in magnetospheric activity prior to the arrival. These suggest that not all the electron dropouts on arrival of SI entered the ionosphere. From the riometer data, the radiation belt losses can, at least in part, be explained for mid-Latitudes where the electron motion is collision dominated. The overall response of SI-driven dropout was later investigated using SEA technique (See Chapter 7).

Chapter 6

Case Studies: MC-Driven Dropouts

Some individual events of MC-driven dropouts on 10 January 1997, 22 January 2000 and 29 October 2000 were examined to better understand the dynamics of the outer radiation belt.

6.1 Case Study 4: MC-Driven Dropout of 10 January 1997

The first MC in the year 1997 occured on 10 January at around 0440 UT, during which there was a dropout. This event was studied by Reeves [1998] but the work did not discuss the ionospheric absorption. In this study, geophysical properties and absorption during this time were considered to better understand their impacts.

6.1.1 Geophysical Parameters and Solar wind Conditions

Figure 6.1 (a-h) presents the geophysical parameters during the MC-driven dropout of 10 January 1997. Figure 6.1 (a) shows plot of Kp at the peak of 6+ on arrival of MC. Kp continued to indicate high magnetospheric activity for about 3 hours after the impact of MC and subsequently returning to pre-event level.

During the time of higher Kp, Dst as presented in Figure 6.1 (b) depicts -80 nT on arrival of MC. Dst continues to measure a storm of about -70 nT for over 7 hours after the event. Such decrease in Dst is indicating an intensification of the ring current.

Figure 6.1 (c) is the plot of GSM B_z. There is smooth rotation starting at 0440 UT from -19 nT to +19 nT at around 1600 UT. This interval indicates the time of MC arrival. During the period of strong, steady southward IMF, the magnetospheric response is characterise of active storms. Within this period, the ring current is also intensified.

Figure 6.1 (d) is the plot of solar wind number density. There is a about a day delay for the peak seen. Delay in solar wind density peak is typical of passage of MC at Earth e.g [Reeves, 1998]. The peak coincides with the time at which the B_z reaches north from the smooth rotation. This trend is highly followed by the Dst.

The solar wind radial velocity (V_x GSE) is shown in Figure 6.1 (e). The effect is not significant as it maintains the same level of around 400 km/s prior to and after the event.

Around the time of high magnetospheric activity and intensified ring current, Figure 6.1 (f) presents the Alfvén Mach number which drops to a lower level of 0.1. Prior to the passage of MC, Alfvén Mach number is higher reaching about 17.

Figure 6.1 (g) is the plot of solar wind pressure. There is also delay in peak of solar wind pressure at about a day after the onset of MC passage corresponding to the time of peak in solar wind number density. This implies magnetopause compression at this time. It is also noted that the Dst also shows the effects of the solar wind pressure enhancement as it turns positive during this interval.

As presented in Figure 6.1 (h), V_y GSE at the time of MC is insignificant as the same level variation is maintained prior to and after the onset of MC.
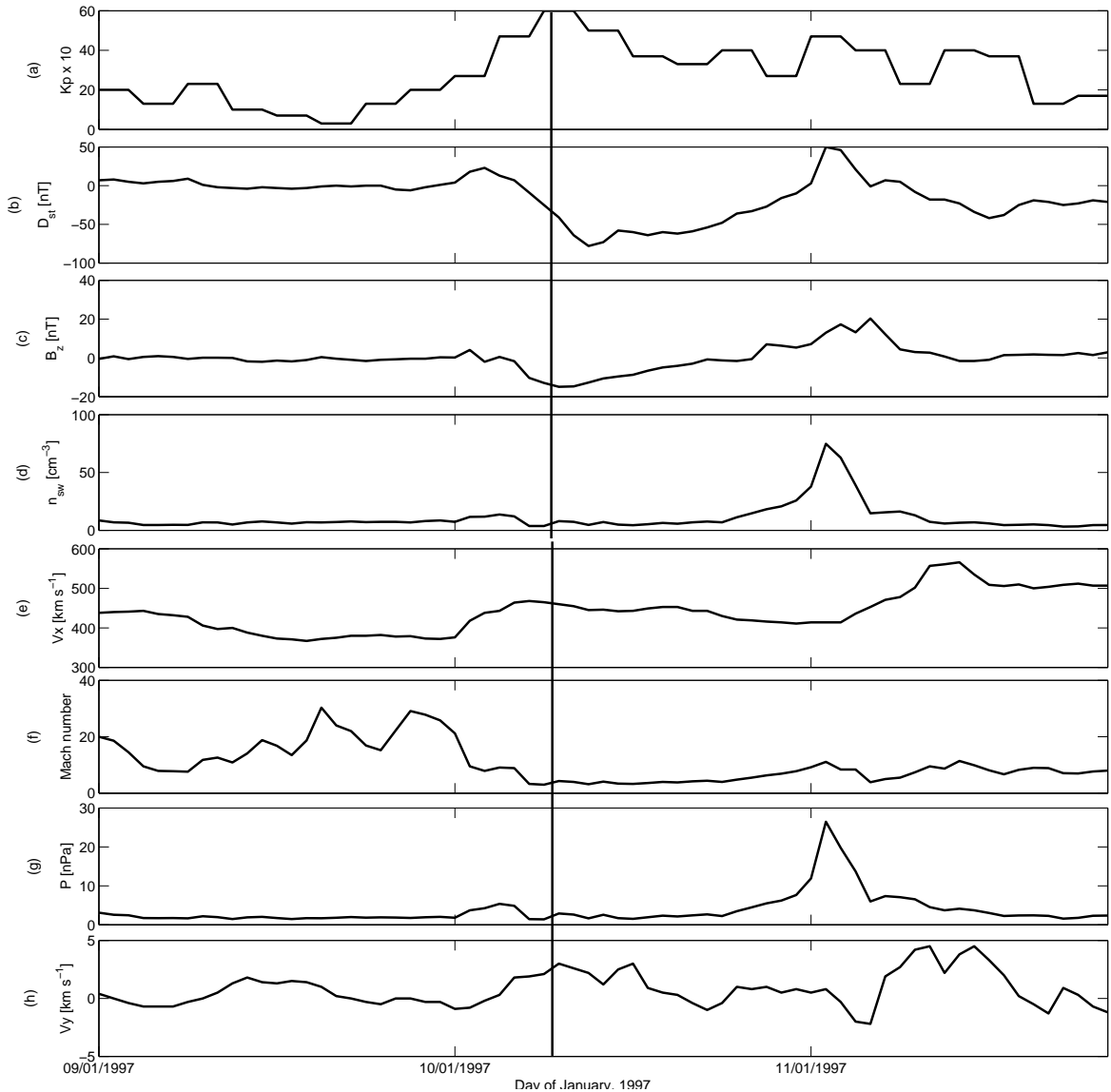
Figure 6.1: Geophysical parameters and solar wind conditions on 10 January 1997 MC-driven dropouts. From a-h are Kp index, Dst index, B_z, Solar wind number density , solar wind radial velocity, Alfvén Mach Number, solar wind pressure and the solar wind azimuthal (west-east) flow velocity. The vertical line indicates the onset of MC.

6.1.2 LANL/SOPA Measurements of Electron Dropout

The electron fluxes from the LANL satellites were examined for the 10 January 1997 event. During this time data was received from 1990-095, 1991-080, and 1994-084 satellites.

In Figure 6.2 (top) measurements from LANL 1991-080 satellite are shown. Dropout is also seen at passage of MC in local noon at about 0700 LT. The order of dropout is about 10^{-1} deeper after the arrival of MC with fast recovery phase. Dropout and recovery are independent of energy similar to that of LANL 1998–084 in Figure 6.2 (middle). However, at the arrival of MC, satellite 1994–084 observed a strong growth phase dropout followed by a small substorm injection at midnight.

On Figure 6.2 (bottom) is the plot of LANL 1990-095 satellite. The effects of adding or removing a satellite can be seen where data gaps exist prior to and after the event. This of course does not help to obtain the clear picture of the scenario observed by LANL 1990-095 but the dropout tendency is true for passage of MC around the night side.

GEO observations of electron flux across the 225 keV to 1.5 MeV band during 10 January 1997 as observed by LANL satellites at different longitudes are independent of energy in dropout and recovery. The smooth rotation of the IMF from south to north is seen to have initiated moderate substorm activity in the magnetosphere. The effect of the substorm is apparent by the rapid fluctuations of GEO energetic electrons. This could probably arise due to the the fluctuating magnetic and electric field at the time of MC arrival.

6.1.3   Riometer Absorption

On 10 January 1997, absorption rates were examined and presented in Figure 6.3 (a-h) from the chain of Finnish riometers. Generally, absorption from the chain of Finish riometers show a narrow peak directly at the passage of MC which cuts across various L values of the riometer stations. With this observation it can be noted that strong substorm-like activity associated with the passage of strong southward IMF B_z in the magnetic cloud causes electrons to be lost into the ionosphere at arrival. This is apparent as simultaneous peak continues to be significant from outside to inside the plasmapause.
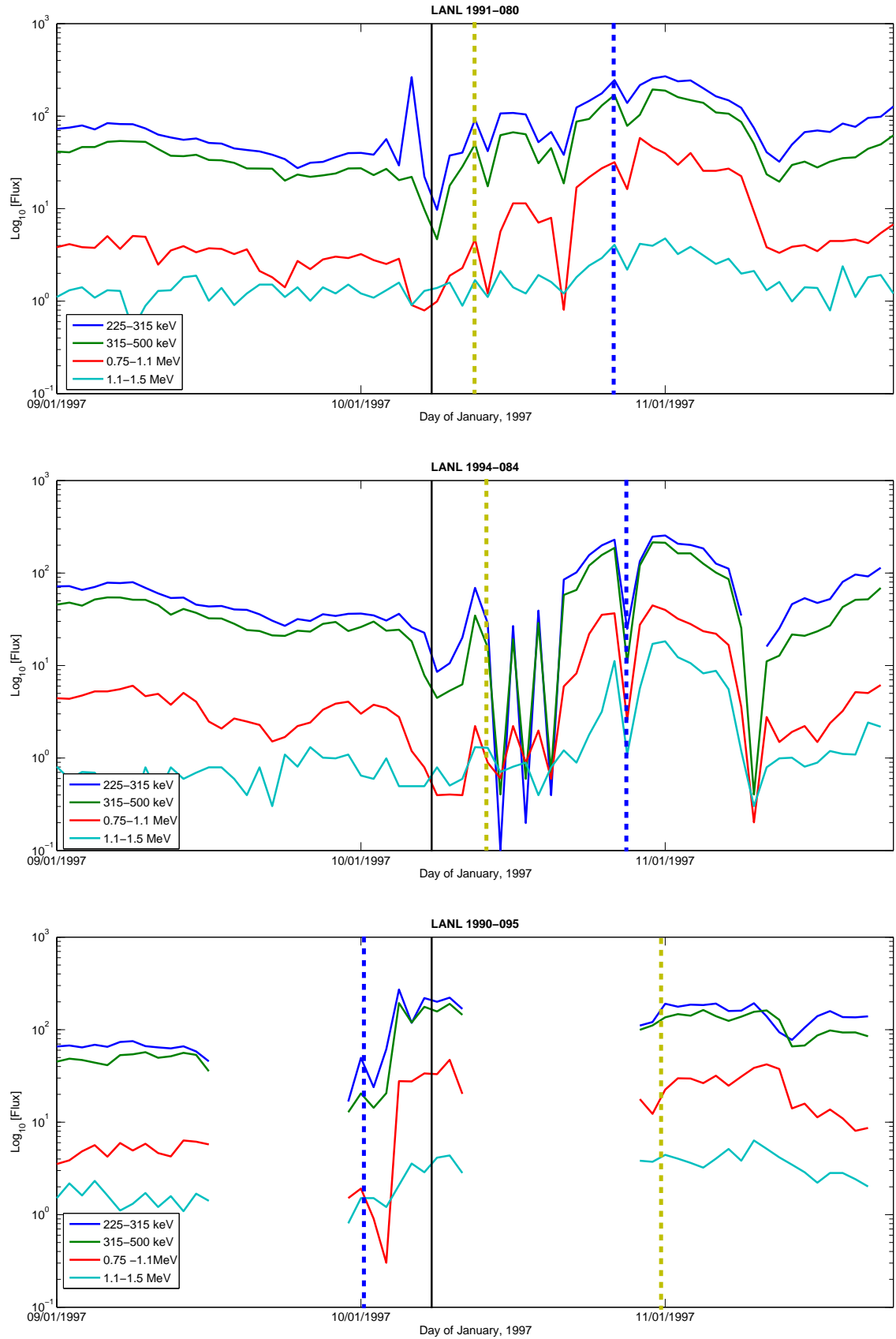
Figure 6.2: Electron flux as measured by the LANL SOPA 1991–080, 1994–084 and 1990–095 satellites during MC-driven dropout of 10 January 1997. From top to bottom, each of the panels contains 225–315 keV (deep blue), 315-500 keV (green), 0.75–1.1 MeV (red) and 1.1–1.5 MeV (light blue). The black vertical line indicates the arrival of MC while the yellow dash-line indicates local noon and blue dash-line indicates local midnight.
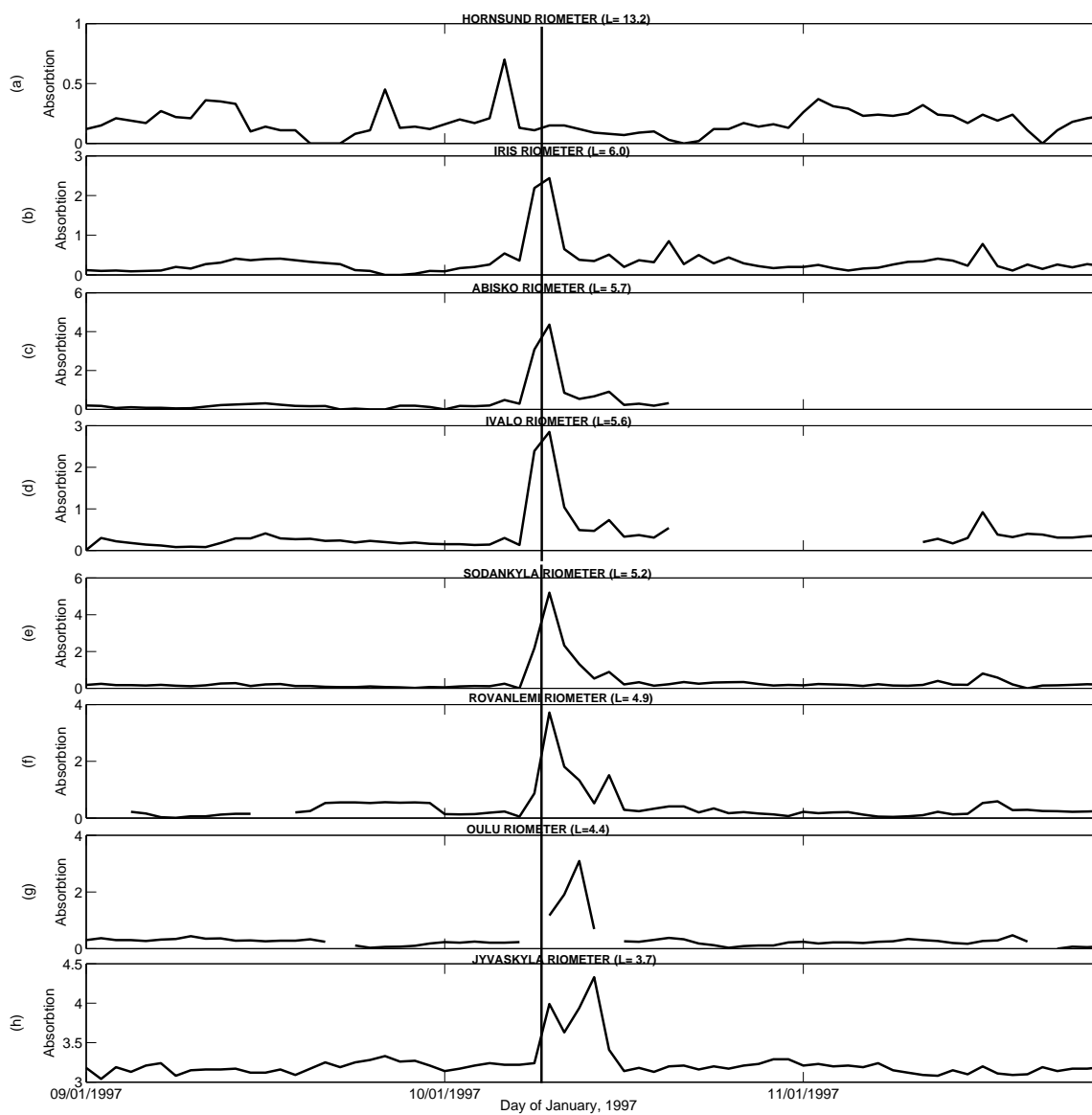
Figure 6.3: Finnish chain of riometers' absorption during dropout of 10 January 1997. The vertical line indicates the onset of MC arrival.

6.2 Case Study 5: MC-Driven Dropout of 29 October 2000

The year 2000 was the last solar maximum and 29 October 2000 is the last MC-driven dropout in the collection of this study. This event is examined for various conditions in the magnetosphere and ionospheric state of absorption.

6.2.1 Geophysical Parameters and Solar wind Conditions

Similar to Figure 6.1, Kp and Dst shows high activities as IMF B_z rotates smoothly from south to north as depicted in Figure 6.4. Other solar wind conditions on 29 October 2000 are also similar to that of 10 January 2007 on arrival of MC. However, contrary to Figure 6.1, a day delay peaks which was earlier noted for n_{sw} and nPa after the arrival were absent in the later observation as illustrated in Figure 6.4.

6.2.2 LANL/SOPA Measurements of Electron Dropout

The response of GEO electron to the event of 29 October 2000 is depicted in Figure 6.5. Similar to Figure 6.2, dropouts due to the strong substorm related activity associated with the passage of strong southward IMF BZ in the magnetic cloud is apparent. However, two LANL satellites provide full coverage for this day. 1998-084 observed the dropout near the night side while 1994-084 observed the dropouts in the dusk side.
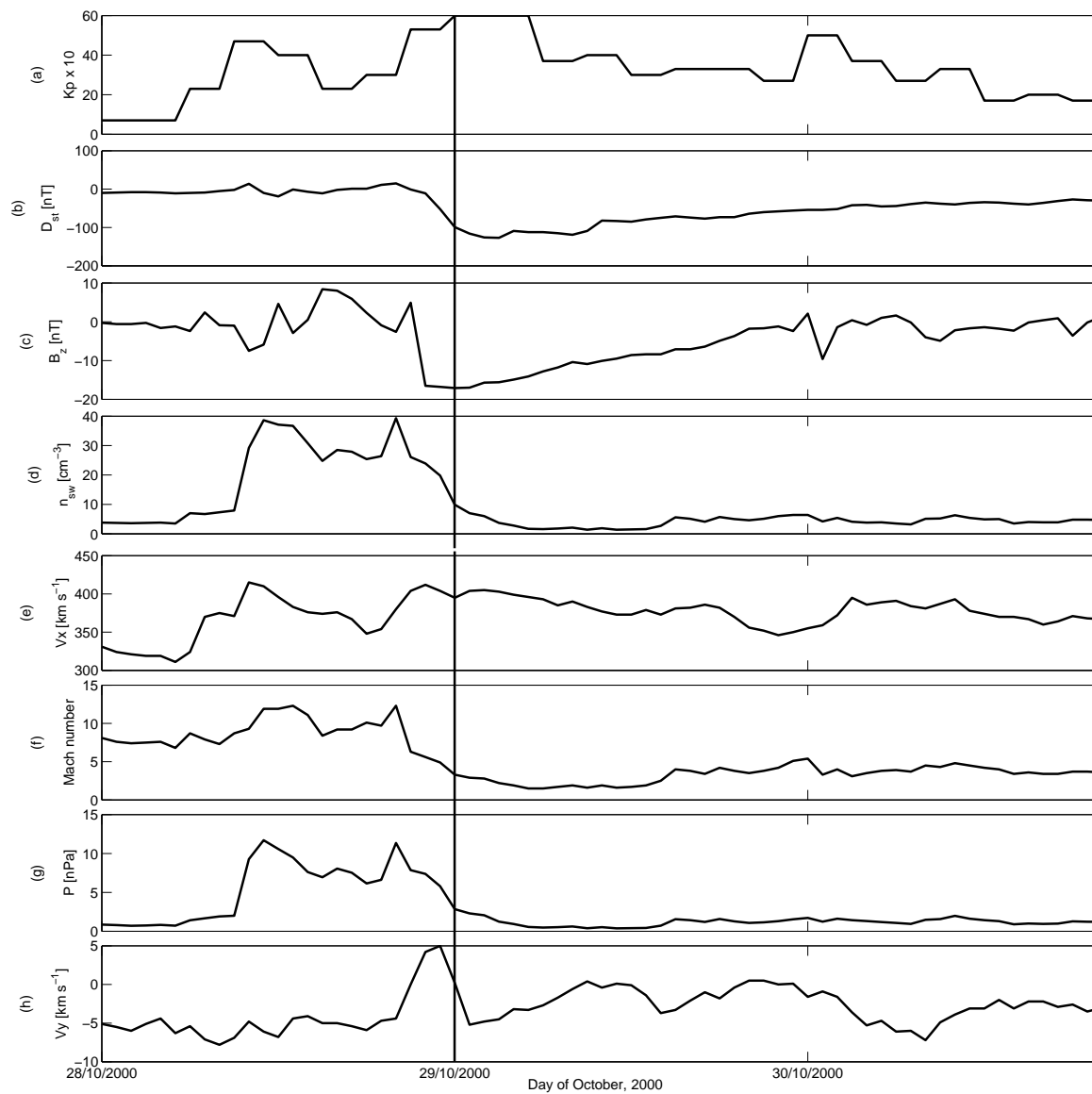
Figure 6.4: Geophysical parameters and solar wind conditions on 29 October 2000 MC driven dropouts. Format is as in figure 6.1
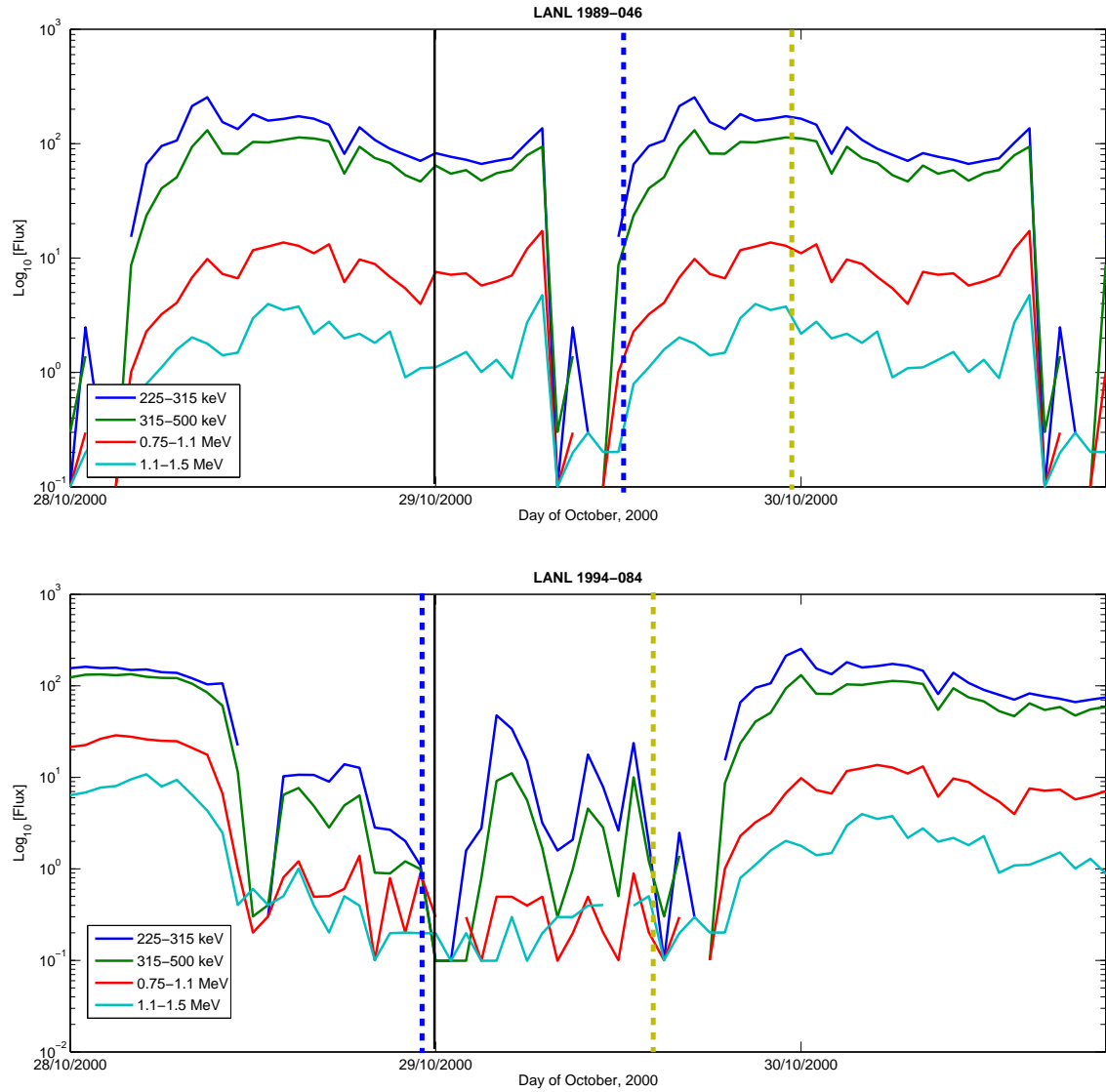
Figure 6.5: Electron flux as measured by LANL SOPA 1989-046, 1994-084 satellites during MC driven dropout of 29 October 2000. Format is as in Figure 6.2

6.2.3   Riometer Absorption

This study further investigates ionsopheric absorption during the MC-driven dropouts of 29 October 2000 as presented in Figure 6.6 (a-h). There are simultaneous peaks in absorption of approximately 2.0 dB at the onset of MC passage. The absorption is much similar to the event presented in Figure 6.3. But the absorption continues for about 3 hours after the event. However, data was not available at Hornsund riometer ($L = 13.2$) at this time.
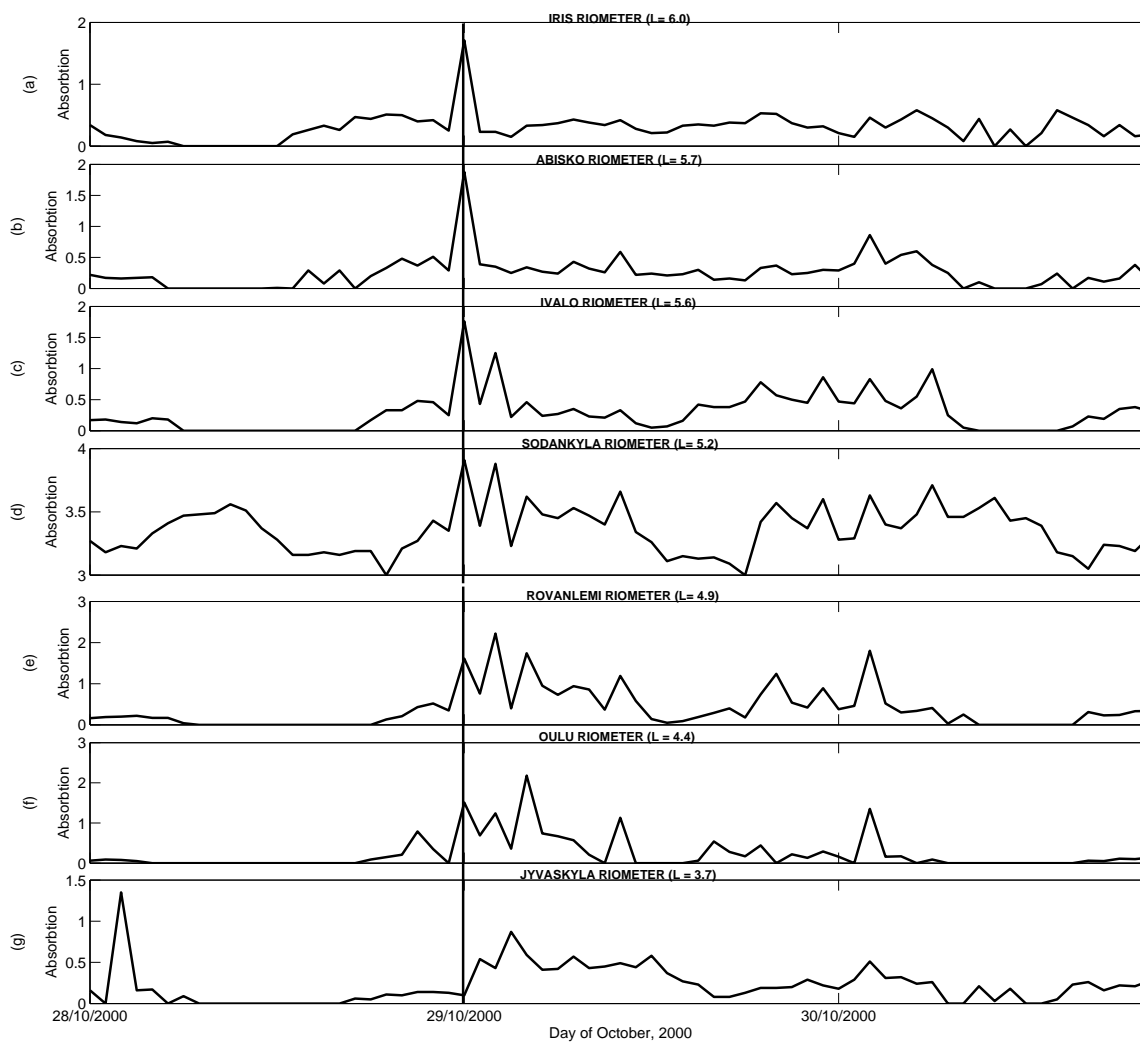
Figure 6.6: Finnish chain of riometers' absorption during dropout of 29 October 2000. Format is as in Figure 6.3.

6.3 Case Study 6: MC-Driven Dropout of 22 January 2000

Another MC-driven dropout case of 22 January 2000 is presented. Various parameters, electron flux levels and rate of absorption during this period were closely examined.

6.3.1 Geophysical Parameters and Solar wind Conditions

Again, Figure 6.7 presents the geophysical parameters for 22 January 2000. Similarities were observed to Figure 6.1 and Figure 6.4. However, the difference in these parameters to immediate event is the delays in peaks seen at solar wind density and pressure. Thus, this observation is overall similar or can be fully explained for that presented in Figure 6.1.
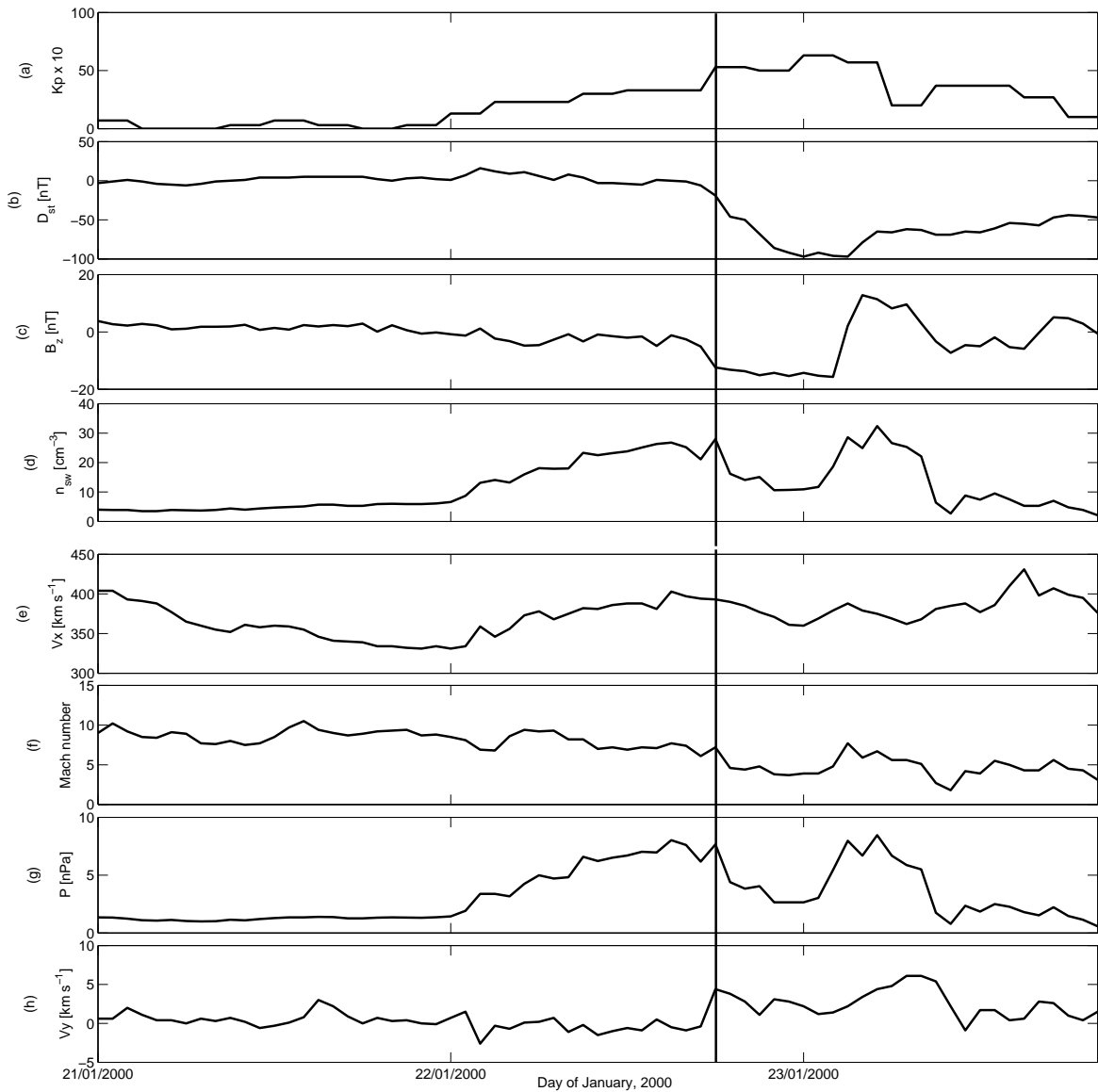
Figure 6.7: Geophysical parameters and solar wind conditions on 22 January 2000 MC-driven dropouts. Format is as in Figure 6.1.

6.3.2 LANL/SOPA Measurements of Electron Dropout

SOPA satellites were further examined for tendency in electron flux dropout. Due to satellite switch, data gaps exist for most of the reporting satellites in orbit at this time. There is also similarity to the previous observations presented in Figure 6.2 and Figure 6.5. Figure 6.8 (top) is the plot of the 1989-046

satellite with tendency for dropouts in the noon side after the impact of MC. Also presented in Figure 6.8 (bottom) is the measurement from the 1994-084 satellite. There is tendency for Dropout on passage of MC in local night side.
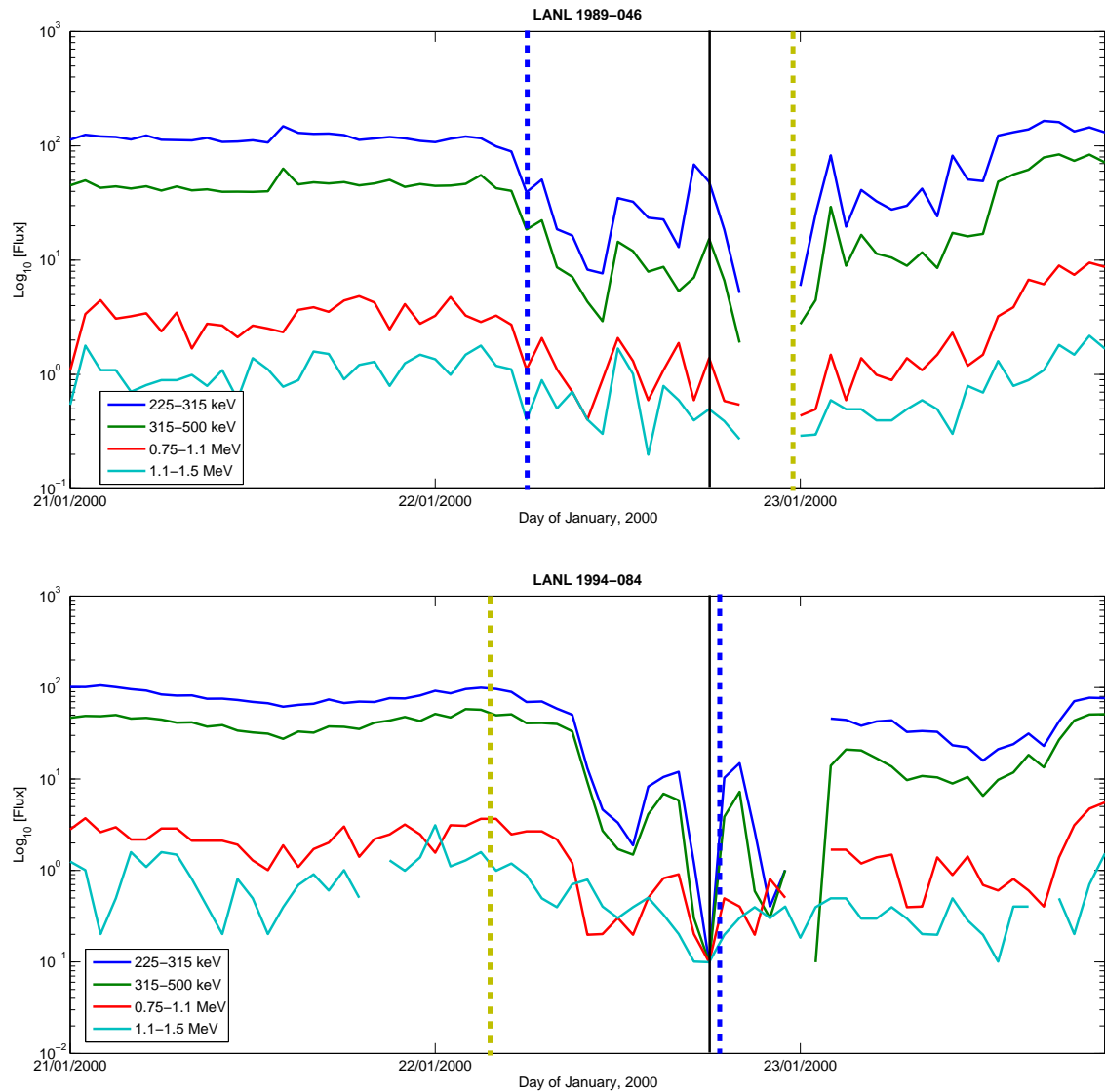
Figure 6.8: Electron flux as measured by LANL SOPA 1989-046, 1994–084 satellites during MC-driven dropout of 22 January 2000. Format is as in Figure 6.2.

6.3.3   Riometer Absorption

Figure 6.9 (a-h) presents an interesting riometer absorption during the MC-driven dropout of 22 January 2000. Throughout the chain of Finish riometers, at onset of the MC passage, there is no indication of peaks in absorption. This observation is different to the previously shown in Figure 6.3 and 6.6. Although there is an observed flux dropout at the passage of MC on 22 January 2000, there was no significant absorption peak. However, during the period of higher magnetospheric activities about 5 hours later there is significant peak in absorption at an approximate of 2.0 dB in the entire riometers chain as seen in Figure 6.9 (a-h).
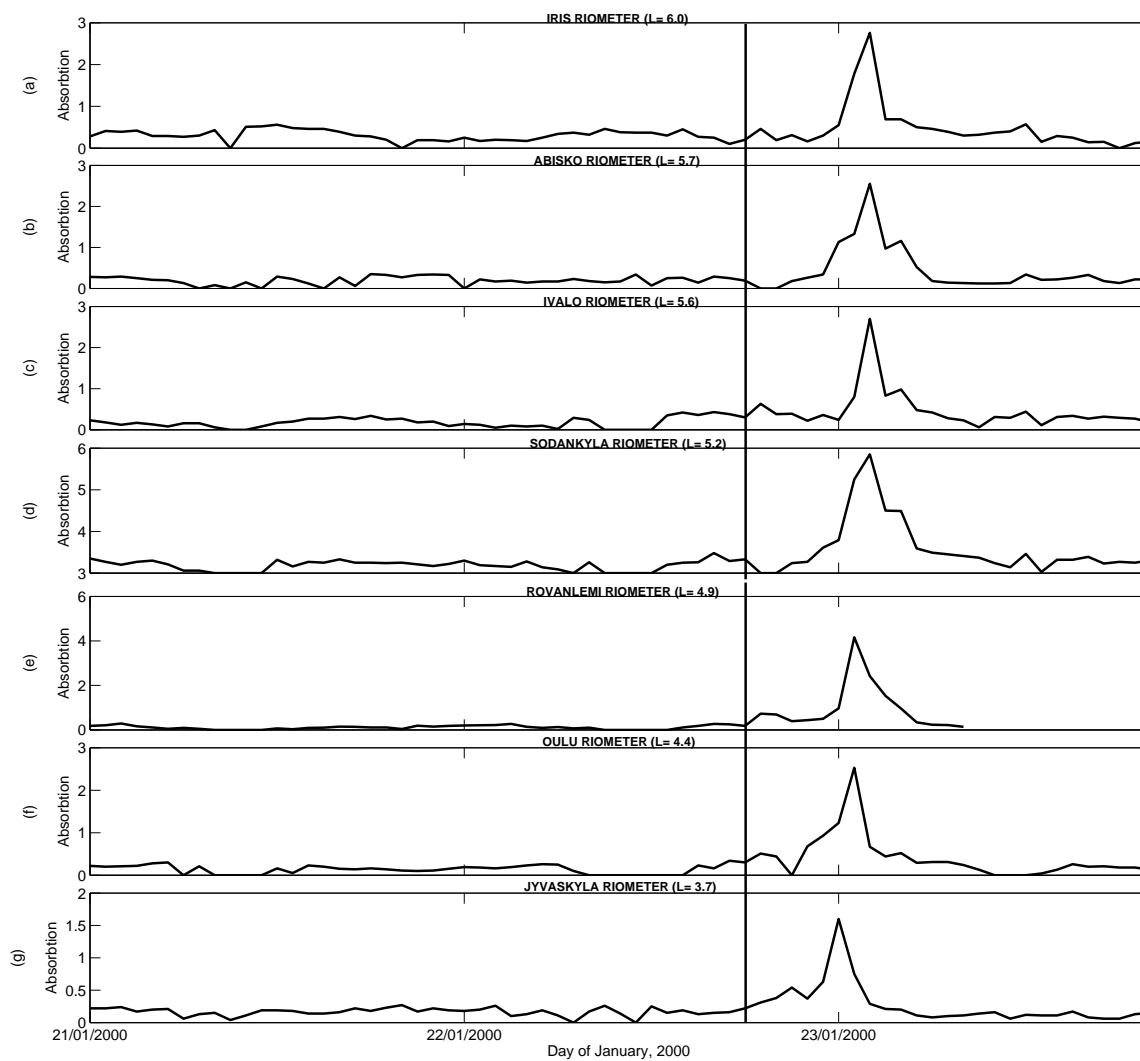
Figure 6.9: Finnish chain of riometers' absorption during dropout of 22 January 2000. Format is as in Figure 6.3.

6.4Summary

Observations for the 10 January 1997, 22 January 2000 and 29 October 2000 MC-driven dropouts have been presented. Dropouts of electron flux began during the period of an increased magnetospheric convection with the Kp index. The effect of the Dst show the significance of adiabatic evolution of ring current during these periods. The recovery of the dropout is, however, not seen to be associated with any significant changes in Kp and Dst. The onset of MC-driven dropout of outer electrons were seen to be simultaneous which is associated with the onset of smooth rotation of IMF B_z from south to North. Two of the events showed that solar wind number density and solar wind radial velocity had no effect on the MC-driven dropouts but a delayed rise was noticed a day after the arrival. During these periods, Alfvén Mach number is typically lower with the onset of electron dropout which remain at lower level during the dropout recovery. Except for a day delay, the onset of dropout and recovery was not seen to be associated with any noticeable change in solar wind pressure. The azimuthal solar wind velocity did not show any significant orientation during MC-driven dropouts.

The logarithms of electron flux of 225–315 keV, 315-500 keV, 0.75–1.1 MeV and 1.1–1.5 MeV around GEO were also examined during these MC driven dropouts. The onset of the dropouts was sudden and not energy dependent. The dropouts cut across all local times indicating non-global features, but rather began in a limited local time region and expanded over some hour period which eventually lead to the global lost of the relativistic electron lost. The appreciable level of dropout was found to correlate with the drop in Dst and smooth switch in IMF B_z from south to north polarity as well as the lower Alfvén Mach number, which is more suggestive of localized effects via substorm related activities and eventual actual lost. The fact that the flux remained high at some locations while dropping to background level at others can be substantiated by the switch in IMZ B_z confirming the adiabatic changes in the initial dropouts. Although, the dropout due to MC is independent of energy but the lower energy (keV) electron flux recovered quickly and much higher than the pre-event level while the higher energy (MeV) took some days to fully recover.

Riometers absorption during these periods showed how electron flux dropouts compared with precipitation. Two of these events, 10 January 1997 and 29 October 2000, showed significant absorption at the onset of MC driven dropout. The absorption was noticeable throughout the entire riometer stations which is contrary to the absorption on 22 January 2000 which was delayed for over 5 hours after the onset of MC driven dropouts. The reason for these observed time scale difference can perhaps be due to multiple contributing processes which occurred nearly simultaneously. However, these observations illustrated the stability of the ionospheric condition when there was no effect of MC driven storms. It is therefore necessary to know the general trend or response of the absorption rate during MC driven dropouts which can be seen in Chapter 7.

Chapter 7

Superposed Epoch Analysis

This chapter presents SEA of the observations and interpretations of the results from the investigation of entire 145 selected SI- and MC driven. The geophysical parameters, electron flux and absorption observations during SI driven dropouts were also compared to MC-driven. Using SEA to understand the consistent response of magnetosphere to storm occurrence is a well established technique [Chree, 1908; Borovsky and Denton, 2009; Morley *et al.*, 2010b].

7.1   SEA: SI Dropouts

The 80 events classified as SI-driven dropouts were used for statistical study. Similar to Section 4, in which Morley's events were used, various geophysical parameters and electron flux measurement from GEO were examined using SEA. In addition, SEA of ionospheric absorption was performed.

7.1.1   SI Dropouts

OMNI data were used to investigate the various geophysical parameters and solar wind conditions during SI-driven dropouts. Figure 7.1 is an overview of geophysical properties of SI dropouts. Each panel contains data superposed and averaged with the zero epoch chosen to be the onset of SI at Earth. The dispersion of the data is shown by providing the 75th and 25th quartiles.

In Figure 7.1 (a), the superposed average of Kp is plotted. Kp is elevated in coincidence with the arrival of SI while it is low prior to the arrival. Although the Kp in OMNI format is seen to be ramping up on -0.8 day, the peak of 4+ is reached in coincidence with the onset of SI arrival at Earth. This is indicative of moderate geomagnetic activity during compressed high-speed solar wind stream. The activity remains on relatively high level after the arrival for about 3 days.

Figure 7.1 (b) is superposed average of Dst. The weakly driven magnetoshere is compressed as indicated by the positive interval prior to the onset of SI which is typical of SI [e.g, Borovsky and Denton, 2006]. At the onset of SI, Dst reverses to modest average of about -30 nT. Since SI is a typical high-speed stream driven storm, strong ring current perturbation is not expected. The average small storm is seen to be persistent for over 3 days after arrival of SI.

Superposed average of the IMF B_z is plotted in Figure 7.1 (c). The northward IMF B_z interval prior to the onset of SI creates calm before the storm. There is a sector reversal from north to south on arrival of SI. This reversal is common in occurrence of SI. During the southward turning of IMF B_z, electrons can gain access into the Earth's ionosphere depositing significant amount of their energy which would enhanced ionospheric ionization.

Figure 7.1 (d) shows the superposed average of solar wind number density. Prior to the arrival of SI, the density is compressed slow wind and a peak of 17 cm^{-3} is seen on arrival of SI. The increase on the arrival of SI is a clear indication of dynamic pressure difference of the fast wind overtaking the slow wind. After the arrival is the compressed fast wind.

Figure 7.1 (e) is the superposed average of solar wind radial velocity (V_x GSE). Prior to the onset of SI is low wind speed at the range of approximately 400 km/s, which is ramping up closer to arrival of SI. The solar wind is well over 550 km/s after the arrival of SI till over +3 days.

The superposed average of Alfvén Mach number is seen in Figure 7.1 (f), showing high Alfvén Mach number. The level remains high at about 9.3 though after the arrival of SI. High Alfvén Mach number is much expected of CIR storm drivers due to high speed solar wind stream. This is contrary to the case of MC-driven storms where the state of magnetosphere is different in operation.

Also shown in Figure 7.1 (g) is the superposed average of solar wind pressure. The solar wind pressure is ramping up few hours to the arrival of SI at Earth and reaches a peak of about 10 nPa on arrival. In about +0.4 day, the solar wind pressure is seen to have returned to pre-event level.

Figure 7.1 (h) presents the superposed average of ecliptic component of solar wind azimuthal velocity (GSE-V_y). The solar wind azimuthal velocity reversed past an average of -12 km/s to +19 km/s on arrival of SI. The point of reversal through zero i.e the reversal from westward to eastward is onset in this study. Any point before the onset is compressed slow wind and after the arrival is compressed fast wind.

7.1.2   Electron Flux during SI Dropouts

Figure 7.2 (a-d) shows the superposed multisatellite average of the logarithm of electron flux from LANL satellites at GEO. Data were obtained from four satellites wherever possible. A running average of the measurement on each was used to construct a multisatellite logarithmic average of all the fluxes available per time. This proves very reasonable because for each of the SOPA satellite in operation, data were normalized so that all satellites have the same yearly averaged logarithm of the flux in the dawn sector [Belian *et al.*, 1992].

At the 225–315 keV electron flux band, there is a strong tendency for superposed average of electron flux dropout few hours to arrival of SI reaching minimum electron flux in about 2 hours after the onset of SI as can be seen in Figure 7.2 (a). At this band, the effect is not well pronounced deeper in the magnetosphere and the recovery takes about 0.2 day but higher than the pre-event level.

In Figure 7.2 (b) is the average of 315–500 keV electron flux. Tendency for electron flux dropout is also seen reaching deepest minimum after the impact of SI. The minimum electron flux time is prolonged for over 4 hours after which there is recovery to pre–event level. Dropouts at this energy band are seen to be about 0.8 order deeper than lower energy band.

At 0.75–1.1 MeV band, the average of electron flux indicates clear tendency for dropout as shown in Figure 7.2 (c) with deepest minimum on arrival of SI. Dropout is at minimum and prolonged for about 0.5 day after the arrival of SI. The recovery is slow and change to pre-event level in 3 days. The dropout is on average of 1.5 order deeper than the lower energy band.

The tendency for electron flux dropout continues at the band of 1.1–1.5 MeV as presented in Figure 7.2 (d). The minimum is seen after the arrival of SI and is much prolonged for over +1 day at its minimum. In respect to lower energy bands, this delay was about 3–4 hours. The recovery is very slow and remains less than the pre–event level for over 3 days after the arrival.

These observations indicate that the observed dropouts level of electron flux can arise through inward diffusion from the plasmasheet, or probably represent an increased ring current electrons through magnetospheric convection for example [Morley *et al.*, 2010b].

7.1.3   Precipitating Electron Flux during SI Dropouts

Similar to previous observations (shown in Figure 4.3) there is no significant precipitation of > 30 KeV electron counts prior to the arrival of SI as presented in Figure 7.3. However, abrupt slower decaying peaks are seen on arrival within $5.05 < L < 6.05$ which persist till 0.5 days. The recovery observed after
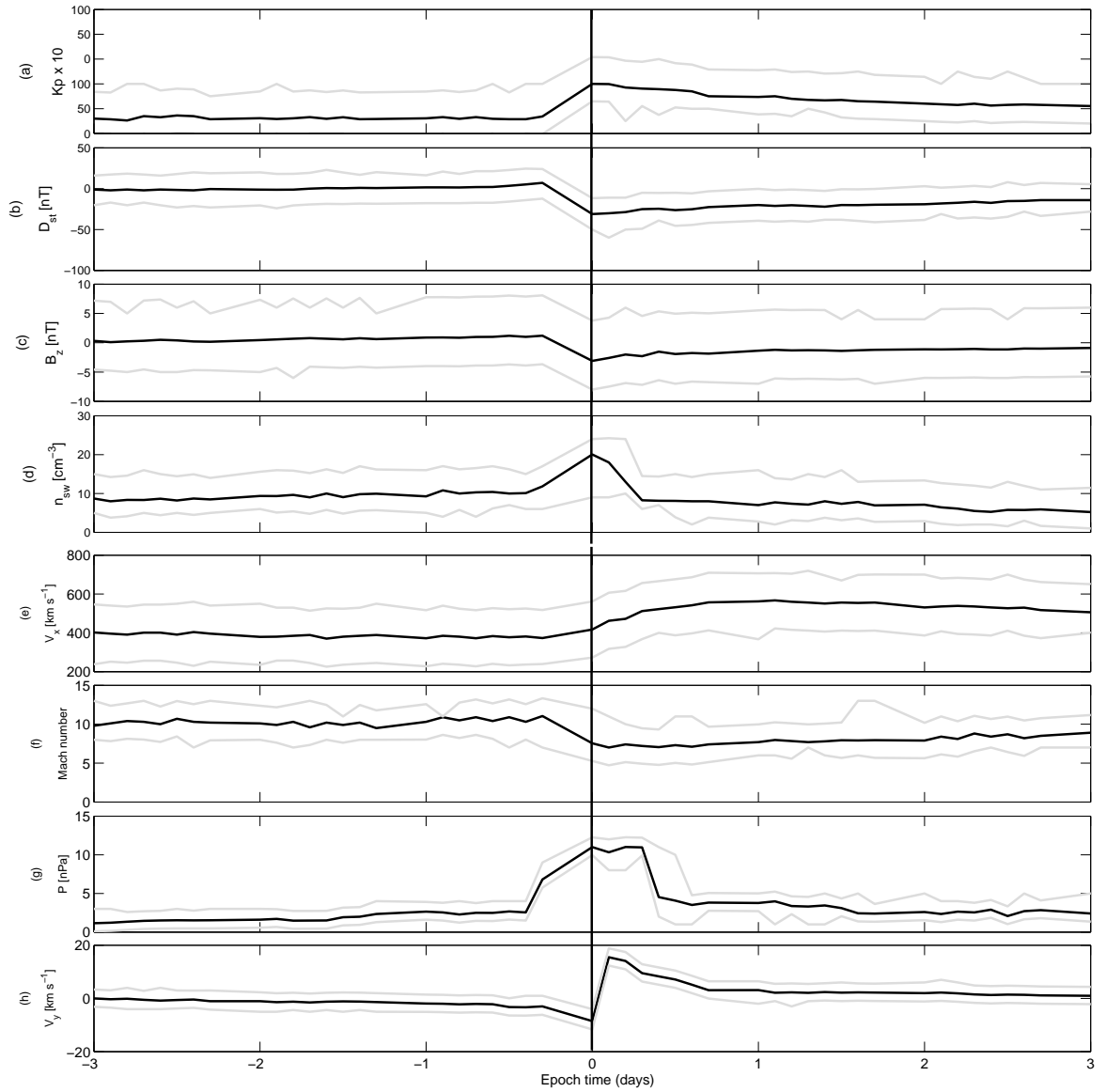
Figure 7.1: Plots of superposed properties of SIs used: in each panel the grey lines are the third quartile and first quartile) while black line indicates the average, with the zero epoch taken as the onset time of V_y reversal indicated by vertical line. From top is Kp, Dst, IMF B_z, solar wind number density, solar wind radial velocity, Alfvén Mach number, solar wind pressure and the solar wind azimuthal (west-east) flow velocity.
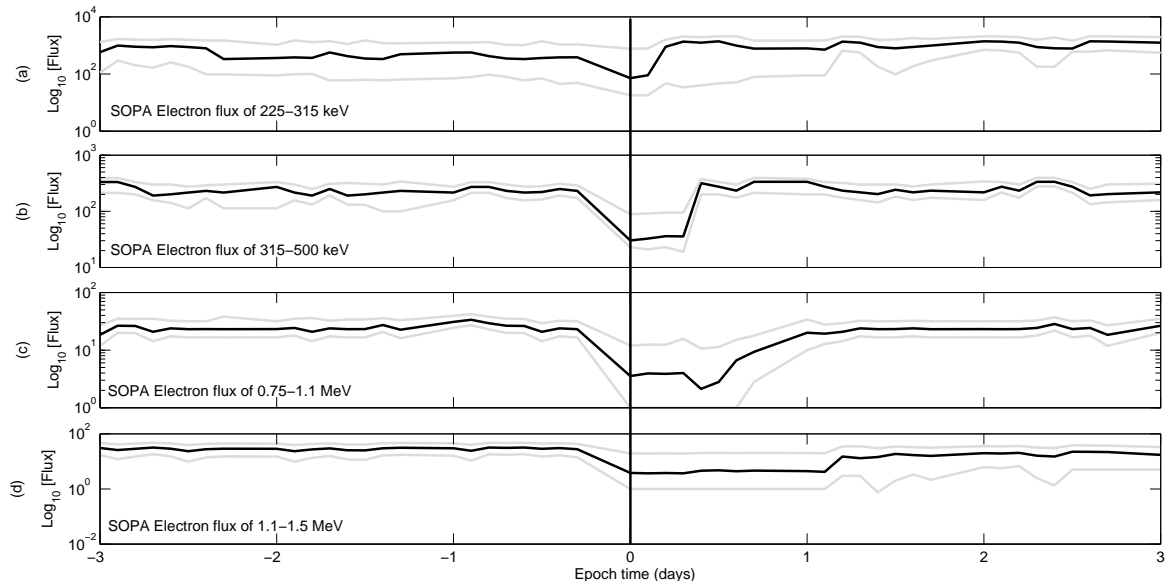
Figure 7.2: Superposed epoch plots of electron flux as measured by combined LANL SOPA satellites: (a) is 225 to 315 keV, (b) 315 to 500 keV, (c) 0.75-1.1 MeV and (d) 1.1-1.5 MeV. The vertical line indicates arrival of SI. Format is as in Figure 7.1.

the 0.5 day is similar to prior the event. An implication of this is that precipitation during SI can still be partly explained for any mechanism that is more dominant around the polar regions.

7.1.4   Riometer Absorption during SI Dropouts

Figure 7.4 (a-h) shows the superposed average of ionospheric absorption throughout the chain of Finish riometers. These observations show superposed average of absorption rate being busty and more localized in the high Latitude of approximately $5 < L < 6$, where absorption is seen to be delayed for over 3 hours after the impact of SI.

Figure 7.3: Superposed L–t of precipitating > 30 keV electron flux by POES satellites during SI-driven dropouts. The color coded are average values of the electron counts.
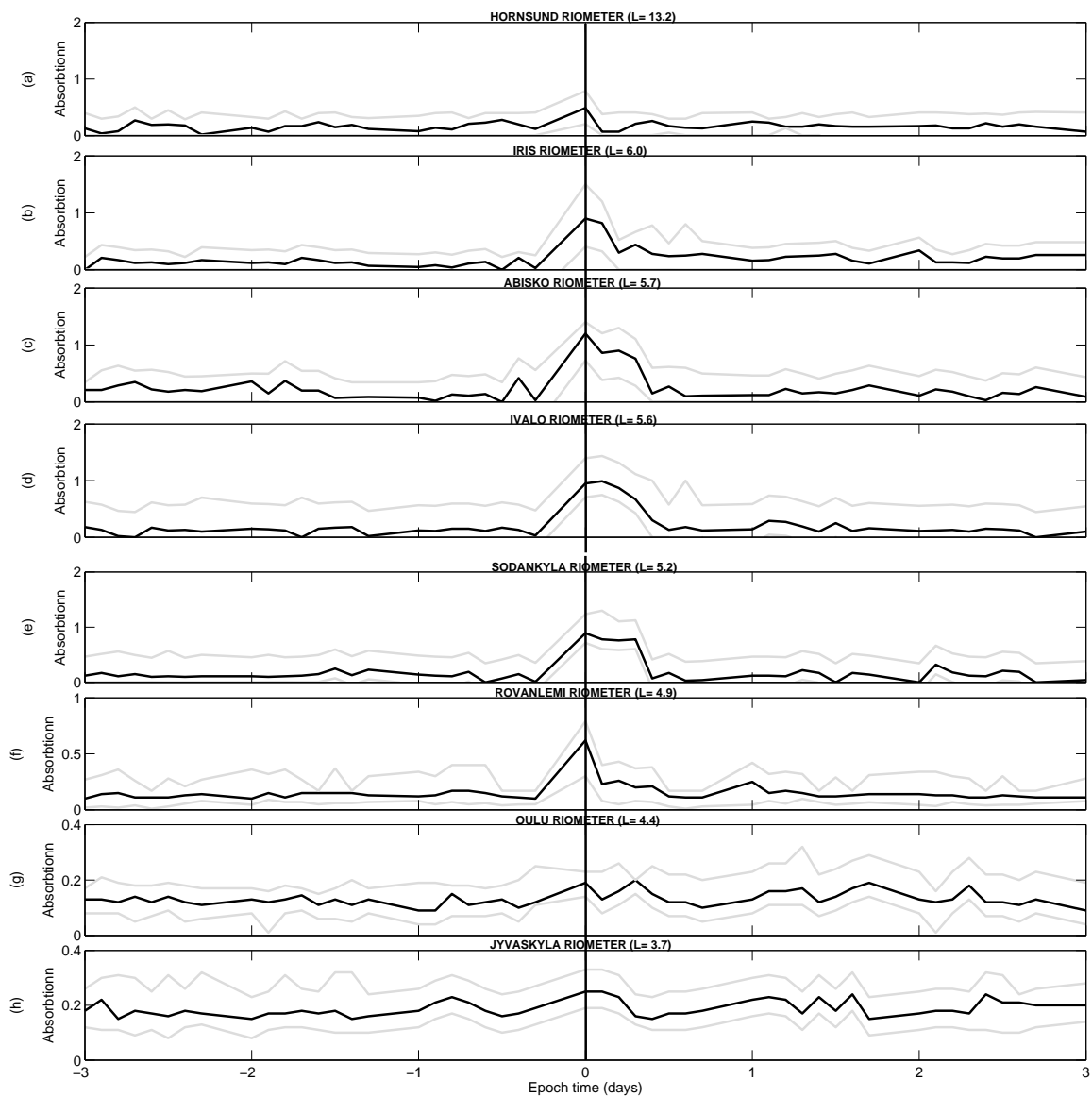
Figure 7.4: Superposed epoch of individual Finnish riometer absorption during SI-driven dropouts. From (a-h) is Hornsund, Iris, Abisko, Ivalo, Sodankyla, Rovanlemi, Oulu and Jyvaskyla. The vertical line indicates arrival of SI. Format is as in Figure 7.1.

7.2   SEA: MC Dropouts

The methods used during SI driven dropouts were again employed to study selected MC driven dropouts for possible correlations.

7.2.1   MC Dropouts

Using the same format as in that of Figure 7.1, Figure 7.5 presents superposed average plots of geophysical parameters and solar wind conditions during MC driven dropouts.

In Figure 7.5 (a) the superposed average of magnetospheric convection measurement, Kp, during MC dropouts showed that the onset of events began during high magnetospheric activity similar to the onset of SI dropouts presented in Figure 7.1 (a) while the recovery of the dropout was not seen to be associated with any significant changes in Kp.

Superposed average of Dst during MC-driven dropouts as presented in Figure 7.5 (b) showed highly intensified ring current effects at the onset of the dropouts contrary to the SI-drivens in Figure 7.1 (b) which clearly showed weak ring current evolution. The recovery was not, however, seen to be of any significant Dst variability.

IMF B_z at the onset of MC and SI dropout were respectively observed in Figure 7.5 (c) and Figure 7.1 (c) to be during southward turning. This is an indication of occurrence of local effects during the two varying storms. But the stretching of the IMF B_z was more prolonged during the MC-driven dropouts.

Contrary to that of MC-driven dropouts shown in Figure 7.5 (d) in which solar wind number density peak was delayed for about a day after the onset of dropout; there was a coincided peak at the onset of SI-driven dropouts as presented in Figure 7.1 (d).

Figure 7.5 (e) shows that solar wind radial velocity remains at a moderate level throughout the MC dropouts while it ramped up to higher level at the onset of SI dropouts as depicted in Figure 7.1 (e). Throughout the recovery of the dropouts there was compressed high speed solar wind during the SI-drivens while the flow remained moderate for the MC-drivens.

During MC-driven dropouts, Alfvén Mach number as presented in Figure 7.5 (f) was lower at the onset which differs from that of SI-driven dropouts shown in Figure 7.1 (f) in which it remained at higher level at the passage of SI. On the recovery sides, the Alfvén remained high for the SI- and lower for the MC-driven dropouts.

Figure 7.5 (g) presents the superposed average of the solar wind pressure. During the onset of the MC-driven dropouts, it was not significant but there was a noticeable peak a day after the onset. This delayed peak was seen to correspond to the time of the delayed peak in solar wind number density. However, this was not the case for SI dropout shown in Figure 7.1 (g) during which there was high solar wind pressure with the onset and sudden drop a few hours later.

In Figure 7.5 (h) solar wind azimuthal velocity is presented. There was not any significant variation in this flow throughout the MC-driven dropouts. Whereas, the reversal of azimuthal solar wind velocity from west to east was seen on superposed average during the onset of SI-driven dropouts in Figure 7.1 (h) indicates the arrival of SI at Earth.

7.2.2   Electron Flux during MC Dropouts

LANL satellites measurements were again examined during MC-driven dropouts as shown in Figure 7.6 (a-d). The superposed logarithm of multisatellites electron flux of 225–315 keV, 315–500 keV, 0.75–1.1 MeV and 1.1–1.5 MeV were performed. The tendency for electron dropout and depth was seen to be gradual and energy independent during MC-driven dropouts as presented in Figure 7.6 while the depth during SI-driven dropouts was energy dependent as shown in 7.2. On recovery, at lower energy, the superposed average of electron flux recovered quickly and to higher level which is similar to the SI-driven dropouts.
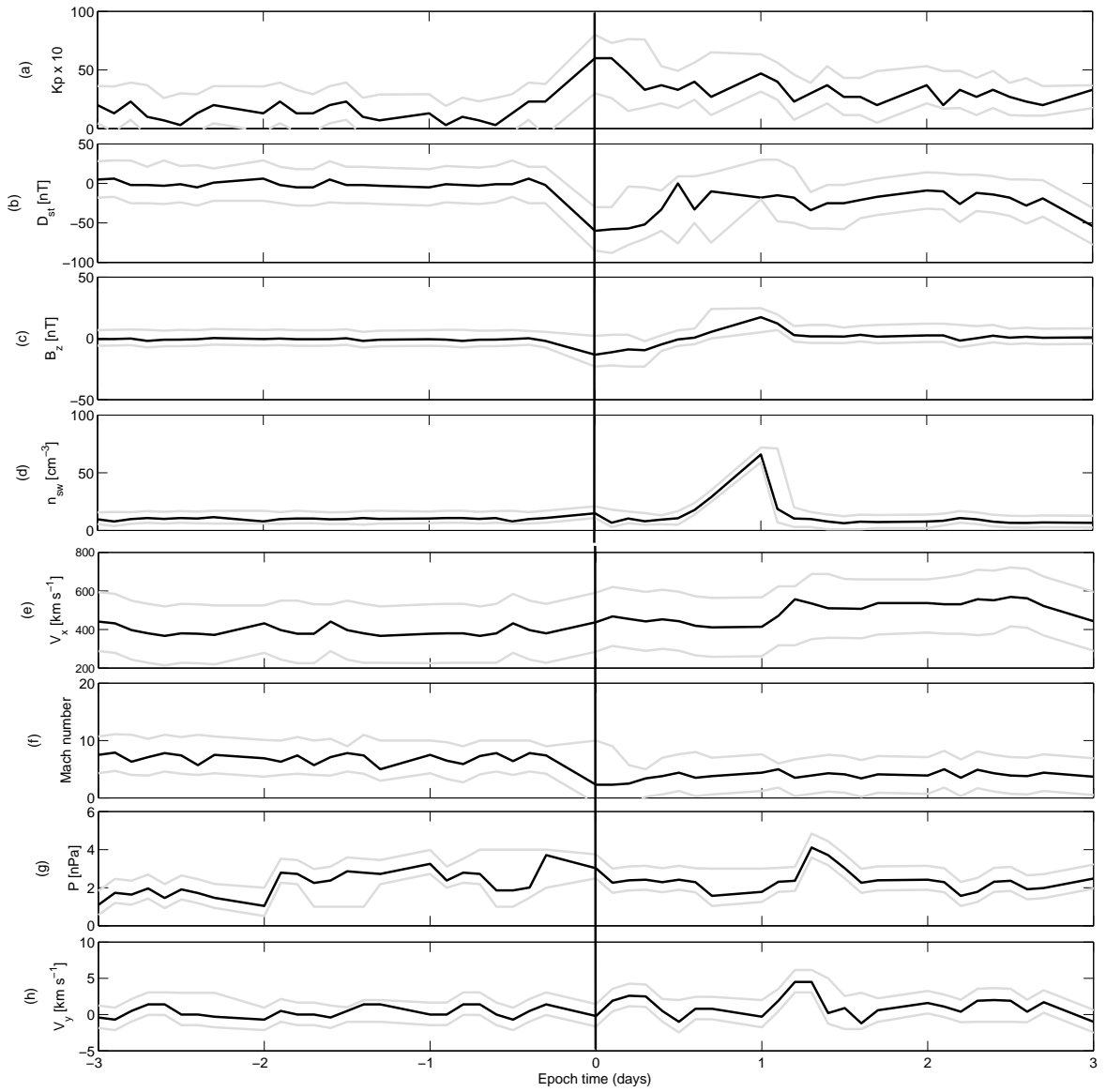
Figure 7.5: Plots of superposed properties of MCs used: in each panel the grey lines are the upper (75 th percentile) and lower (25 th percentile) quartiles while black line indicates the average, with the zero epoch taken as the onset time smooth rotation of Bz from the south to north as indicated by vertical line. Format is as in figure 7.1
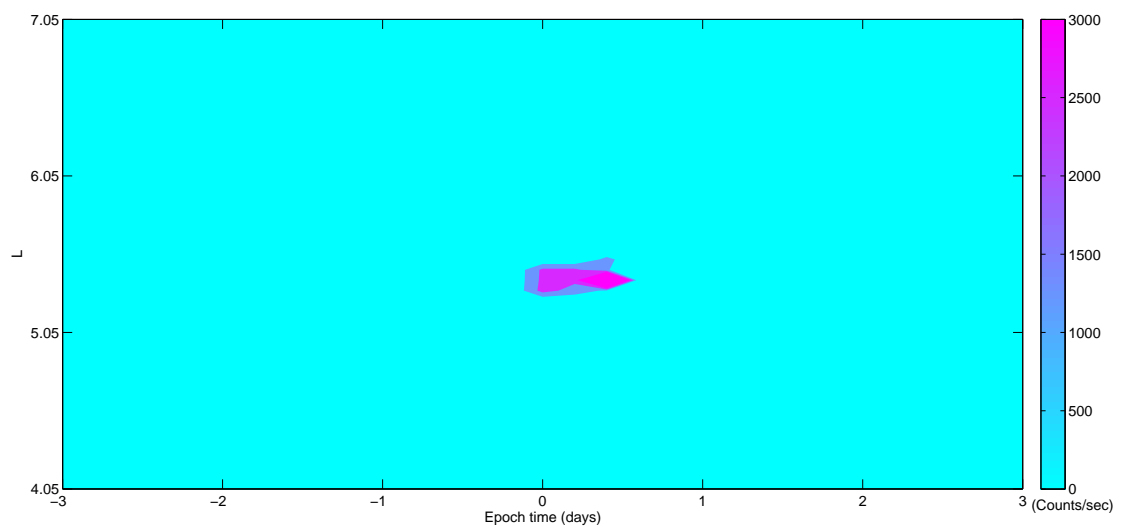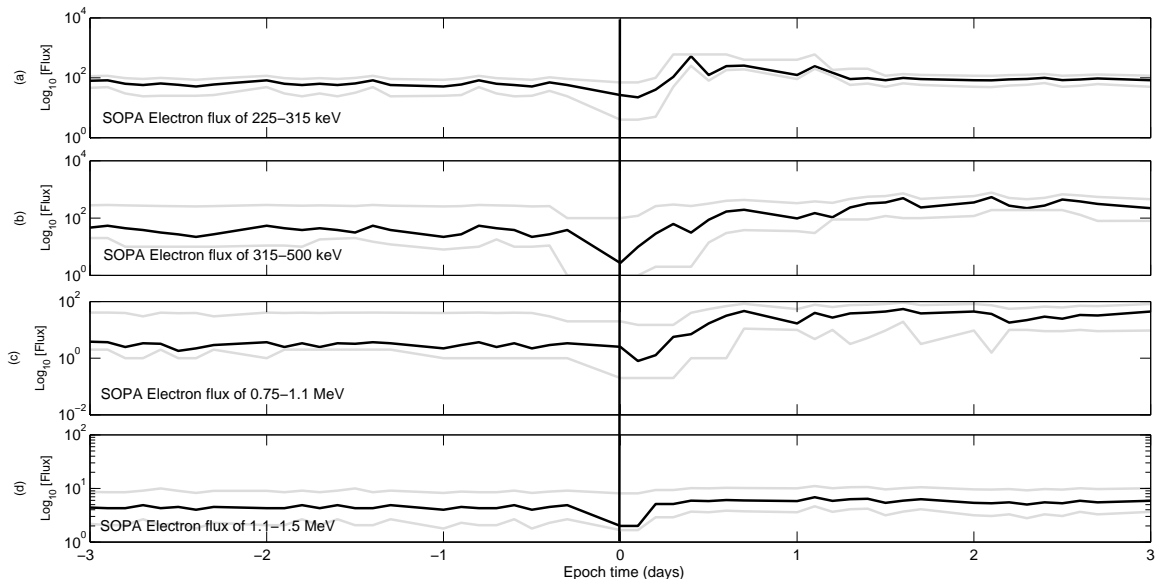
Figure 7.6: Superposed epoch plots of electron flux as measured by combined LANL SOPA satellites: Format is as in Figure 7.2.

Similarity was also observed for higher energy of electron flux which did not recover quickly to pre-event level   for   either   MC   or   SI   dropouts.

7.2.3   Precipitating Electron Flux during MC Dropouts

Contrary to Figure 7.3, Figure 7.7 shows that, > 30 KeV electron counts indicates significant precipitation in lower L at the onset of MC dropout. This difference is indicative of precipitation occurring outside plasmapause during the SI event while it perhaps extended to plasmapause at the impact of MC. It is expected the refore that MC occurrence will have more effects on ground-based instruments. Theriometers absorption will then be examined in the next subsection.
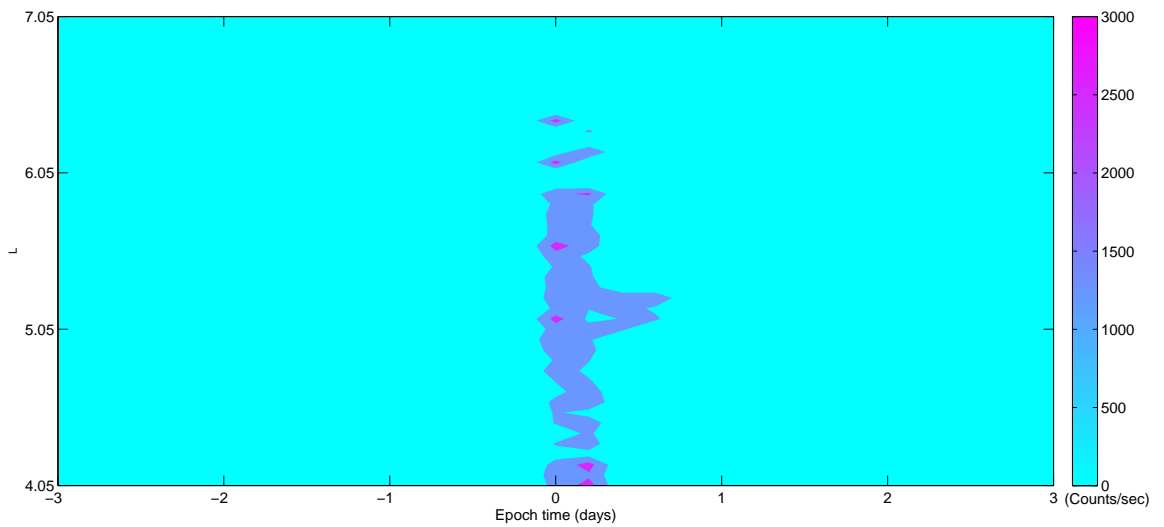
Figure 7.7: Superposed L–t precipitating > 30 keV electron flux by POES satellites during MC-driven dropouts. Format is as in Figure 7.3.

7.2.4   Riometer Absorption during MC Dropouts

The superposed average from Finnish chain of riometers showed that the ionospheric absorption extended to lower L on average for the MC dropout as shown in Figure 7.8 whereas absorption was only pronounced and significant mostly at the high latitude ($5 < L < 6$) during the SI dropouts as presented in Figure 7.4. The result of SI absorption can be correlated with Morley *et al.* [2010b] which suggest chorus driven effects which are mostly dominant at the high latitude and around the morning sector as possible operating mechanism. Although this does not completely rule out the role of EMIC waves which mostly characterised the afternoon sector. However, the result obtained from the SEA of absorption during MC-driven was an indication of pronounced adiabatic effects with more ionospheric impact. Here, the SEA represented the majority trend of the events but some events were seen to disobey these responses, herein referred to as non-response events with no significant absorption peaks throughout or absorption peaks prior to, or seen to be at peak a day after the onset of the events. Example of such non-response events was earlier shown in Figures 5.9 and 6.7. These non-response events could possibly arise due to varying mechanisms operating simultaneously.
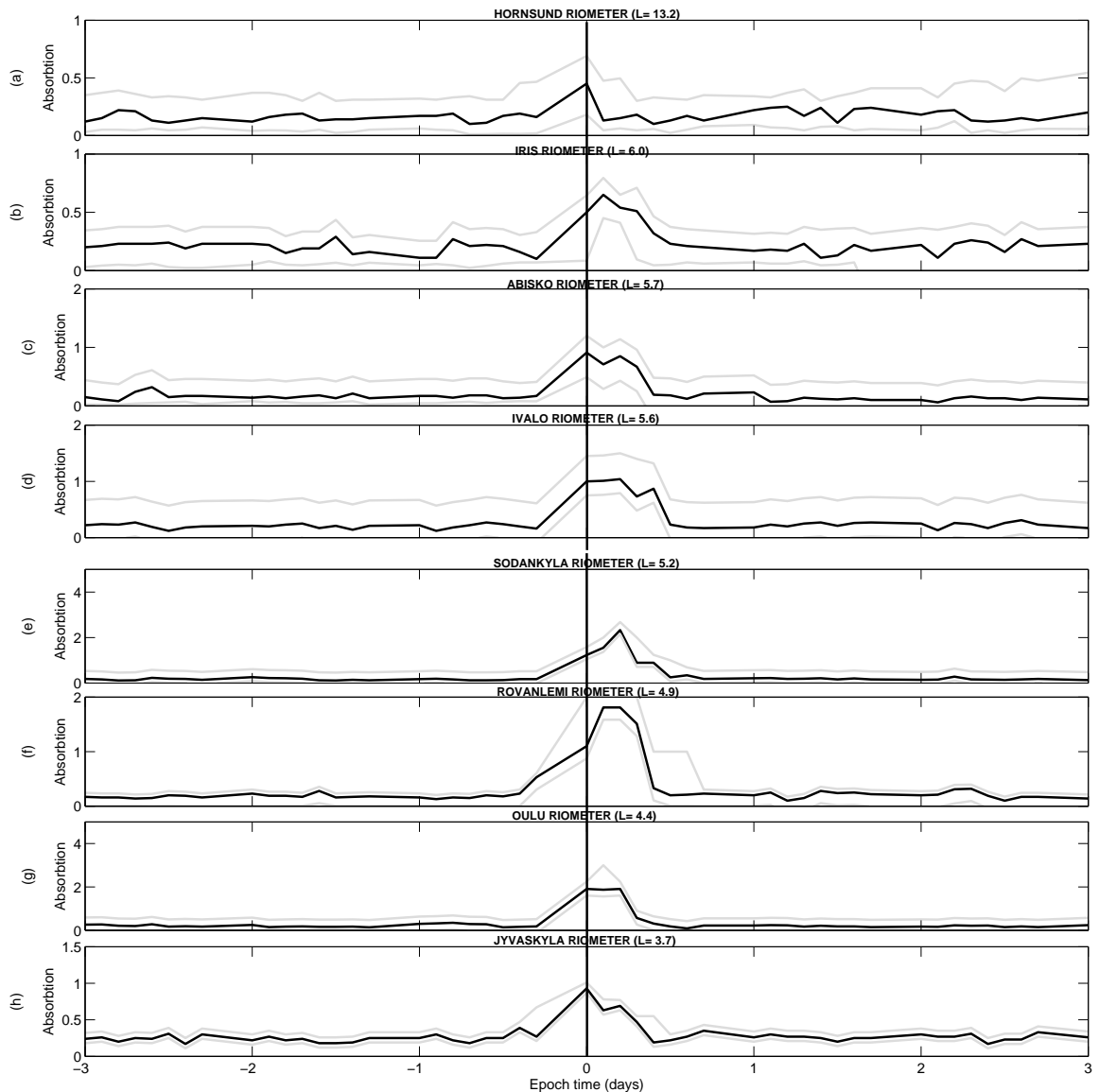
Figure 7.8: Superposed epoch plots of individual Finnish riometer absorption during MC-driven dropouts as detected by Finnish chain of riometers. Format is as in Figure 7.4.

7.3   Discussion

Outer radiation belt dropouts involve rapid lost of energetic electrons at the main phase of a storm and subsequent rapid recovery. These dropouts penetrate through the Earth's magnetosphere and often dumped into the ionosphere. The dropouts interact with various plasma waves and thus, causing enhanced ionospheric density at the collision dominated regions. Dropouts usually respond to SI and MC events.

To understand the dynamics of the SI driven and MC driven dropouts, various geophysical parameters were analysed. Electron measurements from GEO and LEO were examined. Also inspected is ionospheric absorption at the time of SI and MC onsets. SEA technique was used to validate the data and test for consistent response of all the considered observations. Results from the SEA indicate that SIs and MCs are important lost drivers with significant similarities and differences in GEO, LEO and Ionospheric environment.

Geomagnetic and solar wind properties were investigated. From the selected SI dropouts, the magnetosphere is immersed in compressed slow solar wind a day prior to the arrival of SI. In coincidence with this gradual lost, the Kp index starts to rise, as does the solar wind number density. The resultant increase in solar wind pressure at the onset would have caused the magnetopause to move inward. These gradual losses are consistent with a combination of loss mechanisms provided that the outward radial diffusion also takes place. Also significant is the turning of IMF B_z from geoineffective to geoeffective on arrival of SI. Apparently, this turning converts closed electron drift paths outside of GEO to open paths allowing electrons to be lost through magnetopause shadowing. On the event of MC dropouts, the charateristics of losses differ. During the course of the MC dropouts, the ring current was strong at onset and then recovers at a slower rate. Such current induction explains the presence of action of adiabatic lost process. The Dst index is a proxy for this process. IMF B_z orientation at MC is southward but the orientation before and after the MC dropouts were almost equally distributed between geoineffective and geoeffective. High Alfvénic magnetic fluctuations contribute to enhanced magnetospheric condition during HSSW. M_A is found to be higher before and after the SI driven dropouts. This is contrary to the case of MC drivens where the M_A was low. The difference of M_A during SI and MC respectively confirms the varying operation of the magnetosphere for CIR-driven and ICME-driven storms.

The SEA of GEO electron flux was performed using combined LANL satellites and the event of SI dropouts were compared with the MC dropouts. On average, the SI dropouts were found to be energy dependent at all local times which only recover quickly at lower energy. The prolonged recovery at higher energy band was likely to be that; acceleration processes are either weak or dominated by lost processes for the higher electron energies. The action of substorm is very apparent at this time which could lead to the occurrence of the dropout seen during the period. In correlation with the geophysical parameters, the other plausible phenomena which could have lead to the observed SI dropouts were noted to be possibly due to an enhanced magnetospheric convection and inward radial diffusion driven by ULF wave. Using the same method, SEA of GEO flux was also done for MC dropout. Contrary to former, the dropout was found to be independent of energy. The MC dropouts cut across all local times indicating non-global features, but rather began in a limited local time region and expanded over some hours period which eventually lead to the global lost of the relativistic electron lost. Beginning with local effects, an eventual lost was noticed during MC. The reason for these observed time scale difference perhaps may be attributed to multiple contributing processes which occurred nearly simultaneously. Significantly, the level of dropout was found to correlate with the drop in Dst indicating presence of adiabatic lost at the onset.

Analysis was presented for average > 30 KeV electron precipitation during both SI and MC dropouts using POES satellites. Statistical analysis revealed an unstructured abrupt peak (with slower decaying character) in precipitating electron flux on arrival of the SI which coincided with time of deepest minimum of observed dropouts. Analysis also reveals region outside plasmapause ($5 < L < 6$) as region with higher precipitation of electron flux during SI dropouts. This is indicative of action of mechanisms acting outside plasmapause such as relativistic electron microburst. This mechanism is known to be associated with scattering by VLF chorus due to their similarity in local time distribution at high latitudes. Although the possibility of EMIC waves which mostly occurred in afternoon sector can not be completely ruled out. There was correspondences between the times of dropouts of outer electrons and the electron

precipitation in the afternoon sector, which suggests that the electrons could also be scattered into the lost cone by the EMIC waves. This is in accordance with the findings of Anderson *et al.* [1992]. But it is expected that the minimum energy for EMIC wave action should be 2 MeV [Meredith *et al.*, 2003]. However, on the contrary, precipitation extended to lower L during MC dropouts. Since the precipitation is also intense outside plasmapause, and higher energy lost did not return to pre event level with the return of IMF B_z from south to north, it is interpreted that non-adiabatic effect was also involved. There was intense decay of ring current electrons during MC dropouts. Precipitation associated with this type of event confirmed the expectation from Tsurutani and Lakhina [1997]. It is expected that at storm recovery phase, any interaction involving whistler mode waves and radiation belt particles is capable scattering energetic electrons into the lost cone resulting into ring current decay.

An attempt was made to correlate the SI and MC dropouts with the ionospheric absorption using a chain of riometers. Riometer peaks at the regions where collision was dominated. During SI, absorption remain busty between mid- and high latitude regions. The peaks at these regions coincided with the time of minimal electron flux. This observation is similar to that of Morley *et al.* [2010b] which shows busty absorption around ($5 < L < 6$) at the morning sector. This is similar to the analysis of POES satellites observation during SI. However, this is not the absolute case for MC dropout as absorption peaks even within the lower L. The absorption during MC was also prolonged when compared with the former event. The results show that SI dropouts has greater effect on space based assets while the MC dropouts has greater impacts on the ionospheric regularities thus, having greater effect on ground based assets.

Chapter 8

Conclusions and Recommendations

8.1 Conclusions

This study has presented an investigation into the responses of GEO and Ionosphere during SI- and MC-driven outer electron radiation belt dropouts. Observations of outer electron dropouts reveal that SI and MC are important interplanetary lost drivers. The SEA analysis was made and there were some significant differences in ionospheric environment during SI and MC dropouts. The geophysical characteristics of these events were also examined. The main results emerging from this investigation are as follows:

1. An increase in dynamic pressure at SI arrival gives an indication that the magnetopause was closer to the Earth. This converts closed electron drift paths outside of GEO to open paths allowing electrons to be lost through the magnetopause shadowing. This of course is contrary during MC as there was no significant peak in dynamic pressure instead there was an intense Dst effect confirming lost to be mainly adiabatic during MC-driven dropouts.

2. The magnetospheric activity was high and prolonged during SI dropouts but brief for MC dropouts. Solar wind conditions especially the Alfvén Mach number, were enhanced and extended over days while it was at lowered level during MC dropouts. The recovery of SI dropouts was associated with compressed fast wind whilst the recovery during MC-driven dropouts was at the onset of northward IMF polarity. Also, the heliospheric current sheet crossing that typically occurs in some hours prior to the SI converted an ineffective IMF B_z orientation to an effective orientation after the interface. In contrast, the IMF orientations before and after the MC were almost equally distributed between effective and ineffective orientations.

3. On average, the SI dropouts were more energy dependent than MC dropouts. The recovery at lower energy bands was either higher or at pre-event level for both types of the events. While at higher energy band, recovery in both types were prolonged which suggests that acceleration processes were either weak or dominated by lost processes for the higher electron energies. During these events, dropouts occurred across all local times but more prevalent at midnight side for MC-driven. SEA showed that there were prolonged electron dropouts at GEO during SI dropouts than MC dropouts. It is also worth to note that the storms produced by SIs was generally very weak yet it produces high fluxes of electrons.

4. Statistical analysis of data from POES satellites in LEO revealed an unstructured abrupt peak (with slower decaying character) in precipitating electron flux on arrival of the SI dropout which coincided with time of deepest minimum of observed dropout. Analysis also reveals high-Latitude as region with higher precipitation of electron flux but extended to lower latitude during MC dropout. These observations could partly be used to explain some lost mechanisms under high speed stream-interface.

5. This study also partly confirms the previous results of Morley *et al.* [2010b] that ionospheric absorption during SI associated dropouts was more enhanced at morning sectors ($5 < L < 6$). It was further showed that the peaks in ionospheric absorption extended to lower L during MC dropouts. The level of absorption was high and pronounced within 60–65 MLAT at the onset of SI but higher and prolonged during MC events even as it extends to lower L.

6. Other features noted in the selection of these events are the solar cycle dependency of the SI and MC dropouts. The SI dropouts were more frequent during the declining phase of solar cycle while the MC dropouts were more dominant during the maximum phase of solar activity. This is in agreement with the recent work of Li *et al.* [2011] which confirms that MeV electron measurements at GEO has a systematic response to solar wind that is dependent on solar cycle.

8.2 Recommendations for Further Research

With the data used in this study, the majority of the SI and MC dropouts were linked to enhanced ionospheric absorption. However, there were some non-response events (i.e, dropouts without associated ionospheric absorption) which did not conform with the general response as shown by SEA. Thus, precipitation of the outer electron dropout into the ionosphere as well as dominant lost mechanism can not be completely established. Further work is needed to separate the non-response events to study ionisation at various regions of the ionosphere both daytime and nighttime. The outer radiation belt boundary should also be examined during such events so as to possibly reveal where and how the dropouts are dumped. Also, the relationship between individual wave-particle interactions and the lost of outer radiation belt relativistic electrons is suggested for further work hence giving insight into the dominant mechanism responsible for the lost. To achieve these, spacecrafts in GEO and LEO with data ordered by L^* is highly recommended. Also, ground based probing instruments that can provide for electron oscillations such as magnetometers will be of great help to partly discern some waves particle-interactions.

Bibliography

B. J. Anderson, R. E. Erlandson, and L. Zanetti. A statistical study of Pc 1-2 magnetic pulsations in the equatorial magnetosphere. 1. Equatorial occurrence distributions. *Journal of Geophysical Research*, *97*, 3075–3101 (1992). doi:10.1029/91JA02706.

W. I. Axford and C. O. Hines. A unifying theory of high-latitude geophysical phenomena and geomagnetic storms. *Canadian Journal of Physics*, *39*(10), 1433 (1961).

D. Baker. Coupling between the solar wind, magnetosphere, ionosphere, and neutral atmosphere. In P. Murdin, editor, *Encyclopedia of Astronomy and Astrophysics*, 2911–2914. Institute of Physics Publishing, Bristol, UK (2001).

D. Baker and R. L. McPherron. Extreme energetic particle decreases near geostationary orbit: A manifestation of current diversion within the inner plasma sheet. *Journal of Geophysical Research*, *95*, 6591 (1990).

S. Basu, K. Groves, and J. Quinn. A comparison of TEC Fluctuations and scintillations at Ascension Island. *Journal of Atmospheric and Solar-Terrestrial Physics*, *61*, 1219–1226 (1999).

W. Baumjohann and R. A. Treumann. *Basic Space Plasma Physics*. Imperial College Press (1996).

R. D. Belian, G. Gisler, T. Cayton, and R. Christensen. High-Z energetic particles at geosynchronous orbit during the great solar proton event series of October 1989. *Journal of Geophysical Research*, *97*, 16 897 (1992).

J. E. Borovsky and M. H. Denton. Differences between CME-driven storms and CIR-driven storms. *Journal of Geophysical Research*, *111*, A07S08 (2006). doi:10.1029/2005JA011447.

J. E. Borovsky and M. H. Denton. A statistical look at plasmapheric drainage plume. *Journal of Geophysical Research*, *113*, A09 221 (2008). doi:10.1029/2007JA012994.

J. E. Borovsky and M. H. Denton. Relativistic-electron dropouts and recovery: a superposed epoch study of the magnetosphere and the solar wind. *Journal of Geophysical Research*, *114*, A02 201 (2009). doi:10.1029/2008JA013128.

J. E. Borovsky and M. H. Denton. Solar wind turbulence and shear: A superposed-epoch analysis of corotating interaction regions at 1 AU. *Journal of Geophysical Research*, *115*, A10 101 (2010). doi:10.1029/2009JA014966.

L. F. Burlaga. Interplanetary stream interfaces. *Journal of Geophysical Research*, *79*, 3717–3725 (1974). doi:10.1029/JA679i025P03717.

L. F. Burlaga. Magnetic clouds: constant alpha force-free configurations. *Journal of Geophysical Research*, *93*, 7217 (1988).

L. B. Callis, R. E. Boughner, D. N. Baker, J. B. Blake, and J. D. Lambeth. Precipitation relativistic electrons - Their long-term effect on stratospheric odd nitrogen levels. *Journal of Geophysical Research*, *96*(15), 2939–2976 (1991).

C. Chree. Magnetic declination at Kew Observatory, 1890-1900. *Philosophical Transactions of the Royal Society of London*, *A*(208), 205–246 (1908). doi:10.1098/rsta.1908.0018.

M. A. Clilverd, C. J. Rodger, R. J. Gamble, T. Ulich, A. Raita, A. Seppälä, J. C. Green, N. R. Thomson, J. A. Sauvaud, and M. Parrot. Ground-based estimates of outer radiation belt energetic electron precipitation fluxes into the atmosphere. *Journal of Geophysical Research*, *115*, A12 304 (2010a). doi:10.1029/2010JA015638.

M. A. Clilverd, C. J. Rodger, T. Moffat-Griffin, E. L. Spanswick, P. Breen, F. W. Menk, R. S. Grew, K. Hayashi, and I. R. Mann. Energetic outer radiation-belt electron precipitation during recurrent solar activity. *Journal of Geophysical Research*, *115*(A8), A0832 (2010b). doi:10.1029/2009JA015204.

M. H. Denton, J. E. Borovsky, R. M. Skoug, M. F. Thomsen, B. Lavraud, M. G. Henderson, R. L. McPherron, J. C. Zhang, and M. W. Liemohn. Geomagnetic storms driven by ICME- and CIR-dominated solar wind. *Journal of Geophysical Research*, *111*, A07S07 (2006). doi:10.1029/2005JA01143.

J. W. Dungey. Interplanetary Magnetic Field and the Auroral Zones. *Physical Review Letters*, *6*(2), 47–48 (1961).

J. Fennell, J. Roeder, H. Spence, H. Singer, A. Korth, M. Grande, and A. Vampola. CRESS observations of particle flux dropouts events. *Advance Space Research*, *18*, 217 (1996).

R. H. W. Friedel, G. Reeves, and T. Obara. Relativistic electron dynamics in the inner magnetophere—A review. *Journal of Atmospheric and Solar-Terrestrial Physics*, *64*, 265 (2002).

N. Y. Ganushkina, I. Dandouras, Y. Y. Shprits, and J. Cao. Locations of boundaries of outer and inner radiation belts as observed by Cluster and Double Star. *Journal of Geophysical Research*, *116*, A09 234 (2011). doi:10.1029/2010JA016376.

T. Gold. Motions in the Magnetosphere of the Earth. *Journal of Geophysical Research*, *64*, 1219 (1959).

R. A. Helliwell. *Whistler and related ionospheric phenomena*. Standford University Press, Standford, California (1965).

T. W. Hill and A. J. Dessler. Plasma motions in planetary magnetospheres. *Science*, *252*, 410 (1991).

R. B. Horne. Acceleration of killer electrons. *Nature*, *3*(11), 2 (2007).

R. B. Horne, R. M. Thorne, S. Glauert, J. Albert, N. P. Meredith, and R. R. Anderson. Timescale for radiation belt electron acceleration by whistler mode chorus waves. *Journal of Geophysical Research*, *110*, A03 225 (2005).

J. A. Jacobs, Y. Kato, S. Matsushita, and V. Troitskaya. Classification of Geomagnetic Micropulsations. *Journal of Geophysical Research*, *69*, 180–191 (1964). doi:10.1029/JZ069i001p00180.

Y. Kamide. Is substorm occurrence a necessary condition for a magnetic storm? *Journal of Geomagnetism and Geoelectricity*, *44*, 109–117 (1992).

Y. Kamide, N. Yokoyama, W. D. Gonzalez, B. T. Tsurutani, I. A. Daglis, A. Brekke, and S. Masuda. Current understanding of magnetic storms: Storm-substrom relationships. *Journal of Geophysical Research*, *103*, 17 705–17 728 (1998).

C. F. Kennel and H. E. Petschek. Limit of stably trapped particle fluxes. *Journal of Geophysical Research*, *77*, 1 (1966).

J. King and N. Papitashvili. Solar wind spatial scales in and comparisons of hourly Wind and ACE plasma and Magnetic field data. *Journal of Geophysical Research*, *110*, A02 209 (2005). doi:10.1029/2004JA010804.

M. G. Kivelson and C. T. Russell. *Introduction to Space Physics*, 3–16. Cambridge University Press (1995).

M. M. Lam, R. B. Horne, N. P. Meredith, S. Glauert, T. Moffat-Griffin, and J. C. Green. Origin of energetic electron precipitation >30 keV into the atmosphere. *Journal of Geophysical Research*, *115*, A00F08 (2010). doi:10.1029/2009JA014619.

R. P. Lepping, L. F. Burlaga, A. Szabo, K. Ogilvie, W. Mish, D. Vassiliadis, A. Lazarus, J. T. Steinberg, C. Farrugia, L. Janoo, and F. Mariani. The Wind magnetic cloud and events of October 18-20, 1995: Interplanetary properties and as triggers for geomagnetic activity. *Journal of Geophysical Research*, *102*, 14 049–14 064 (1997). doi:10.1029/97JA00272.

R. P. Lepping, J. A. Jones, and L. F. Burlaga. Magnetic field structure of interplanetary magnetic clouds at 1 AU. *Journal of Geophysical Research*, *95*, 11 957 (1990).

J. L. Leroy. *Observation of prominence magnetic fields. In Dynamics and Structure of Quiescent Solar Prominences*, 77–114. Dordrecht Kluwer (1989).

W. Li, Y. Y. Shprits, and R. M. Thorne. Dynamic evolution of energetic outer zone electrons due to wave-particle interactions during storms. *Journal of Geophysical Research*, *112*, A10 220 (2007). doi:10.1029/2007JA012368.

X. Li, M. Temerin, D. N. Baker, and G. D. Reeves. Behavior of MeV electrons at geosynchronous orbit during last two solar cycles. *Journal of Geophysical Research*, *116*, A11 207 (2011). doi:10.1029/2011JA016934.

T. M. Loto'aniu, H. J. Singer, C. L. Waters, V. Angelopoulos, I. R. Mann, S. R. Elkington, and J. W. Bonnell. Relativistic electron loss due to ultralow frequency waves and enhanced outward radial diffusion. *Journal of Geophysical Research*, *115*, A12 245 (2010). doi:10.1029/2010JA015755.

H. McCreadie. A Seasonal Variation in the Dst Index and its Relevance to Models from Magnetic Survey Mission. *American Geophysical Union*, 31 (2001).

C. E. McIlwain. Plasma Convection in the Vicinity of Geosyncronous Orbit in the Earth's Magnetosphere Processes. *Earths Magnetospheric Processes*, 268–279 (1972).

N. P. Meredith, R. B. Horne, and R. R. Anderson. Substorm dependence of chorus amplitudes:implications for the acceleration of electrons to relativistic energies. *Journal of Geophysical Research*, *106*, 13 165–13 178 (2001).

N. P. Meredith, R. B. Horne, M. M. Lam, M. H. Denton, J. E. Borovsky, and J. C. Green. Electron precipitation during high speed solar wind stream driven storms. *Journal of Geophysical Research*, *116*, A05 223 (2011). doi:10.1029/2010JA016293.

N. P. Meredith, R. M. Thorne, R. B. Horne, D. Summers, B. J. Fraser, and R. R. Anderson. Statistical analysis of relativistic electron energies for cyclotron resonance with EMIC waves observed on CRRES. *Journal of Geophysical Research*, *108*, 1250 (2003). doi:10.1029/2002JA009700,2003.

R. Millan, R. Lin, D. Smith, K. Lorentzen, and M. McCarthy. X-ray observations of MeV electron precipitation with a balloon-borne germanium spectrometer. *Geophysical Research Letters*, *29*, 2194 (2002).

R. Millan and R. Thorne. Review of radiation belt relativistic electron losses. *Journal of Atmospheric and Solar-Terrestrial Physics*, *69*(3), 362–377 (2007).

S. K. Morley, R. H. W. Friedel, T. E. Cayton, and E. Noveroske. A rapid, global and prolonged electron radiation belt dropout observed with the Global Positioning System constellation. *Geophysical Research Letters*, *37*(6), L06 102 (2010a).

S. K. Morley, R. H. W. Friedel, E. L. Spanswick, G. D. Reeves, J. T. Steinberg, J. Koller, T. Cayton, and E. Noveroske. Dropouts of the outer electron radiation belt in response to solar wind stream interfaces: global positioning system observations. *Proceedings of Royal Society*, *466*, 3329–3350 (2010b).

R. C. Olasen, S. Shawhan, D. L. Galagher, J. L. Green, C. R. Chappell, and R. R. Anderson. Plasma observations at the earth's magnetic equator. *Journal of Geophysical Research*, *92*, 2385–407 (1987).

T. G. Onsager, G. Rostoker, H. J. Kim, G. D. Reeves, T. Obara, H. J. Singer, and C. Smithtro. Radiation belt electron flux dropouts: local time, radial and particle-energy dependence. *Journal of Geophysical Research*, *107*, 1382 (2002). doi:10.1029/2001JA000187.

T. O'Brien, M. Looper, and J. Blake. Quantification of relativistic electron microburst loss during the GEM storms. *Journal of Geophysical Research Letter*, *31*, L04 802 (2004).

G. D. Reeves. Relativistic electrons and magnetic storms. *Journal of Geophysical Research Letter*, *25*, 1817 (1998).

C. J. Rodger, M. A. Clilverd, J. C. Green, and M. M. Lam. Use of POES SEM-2 observations to examine radiation belt dynamics and energetic electron precipitation into the atmosphere. *Journal of Geophysical Research*, *115*, A04 202 (2010a). doi:10.1029/2008JA014023.

C. J. Rodger, M. A. Clilverd, A. Seppälä, N. R. Thomson, R. J. Gamble, M. Parrot, J. A. Sauvaud, and U. Th. Radiation belt electron precipitation due to geomagnetic storms: significance to middle atmosphere ozone chemistry. *Journal of Geophysical Research*, *115*, A11 320 (2010b). doi:10.1029/2010JA015599.

C. T. Russell and R. C. Elphic. ISEE Observations of Flux Transfer Events at the Dayside Magnetopause. *Journal of Geophysical Research Letter*, *6*, 33 (1979).

C. T. Russell and R. L. McPherron. Semiannual variation of geomagnetic activity. *Journal of Geophysical Research*, *78*, 92–108 (1973).

Y. Y. Shprits, L. Chen, and R. M. Thorne. Simulations of pitch angle scattering of relativistic electrons with MLT-dependent diffusion coefficients. *Journal of Geophysical Research*, *114*, A03 219 (2009). doi:10.1029/2008JA013695.

A. J. Smith, R. B. Horne, and N. P. Meredith. Ground observations of chorus following geomagnetic storms. *Journal of Geophysical Research*, *109*, A02 205 (2004). doi:10.1029/2003JA010204.

M. F. Thomsen, S. Bame, D. McComas, M. Moldwin, and K. Moore. The magnetospheric lobe at geosynchronous orbit. *Journal of Geophysical Research Letter*, *99*, 17 283 (1994).

R. M. Thorne. Radiation belt dynamics: The importance of wave-particle interactions. *Geophysical Research Letters*, *37*, L22 107 (2010). doi:10.1029/2010GL044990.

R. M. Thorne, T. O'Brien, Y. Y. Shprits, D. Summers, and R. B. Horne. Timescale for MeV electron microburst loss during geomagnetic storms. *Journal of Geophysical Research*, *110*, A09 202 (2005).

B. T. Tsurutani and G. S. Lakhina. Some Basic Concepts of Wave-Particle Interactions in Collisionless Plasmas. *Reviews of Geophysics*, *35*(4), 491–502 (1997).

A. Ukhorskiy, K. Takahashi, B. Anderson, and H. Korth. The impact of toroidal ULF waves on the outer radiation belt electrons. *Journal of Geophysical Research*, *110*, A10 202 (2005). doi:10.1029/2005JA011017.

A. Y. Ukhorskiy, Y. Y. Shprits, B. J. Anderson, K. Takahashi, and R. Thorne. Rapid scattering of radiation belt electrons by storm-time EMIC waves. *Geophysical Research Letters*, *37*, L09 101 (2010). doi:10.1029/2010GL042906.

A. Varotsou, R. Friedel, G. Reeves, B. Lavraud, R. Skoug, T. Cayton, and S. Bourdarie. Characterization of relativistic electron flux rise times during the recovery phase of geomagnetic storms as measured by the NS41 GPS satellite. *Journal of Atmospheric and Solar-Terrestrial Physics*, *70*(14), 1745–1759 (2008).

C. Yue, Q. Zong, Y. Wang, I. I. Vogiatzis, Z. Pu, S. Fu, and Q. Shi. Inner magnetosphere plasma characteristics in response to interplanetary shock impacts. *Journal of Geophysical Research*, *116*, A11 206 (2011). doi:10.1029/2011JA016736.